Quantum Hall Transport in Graphene and its Bilayer

Yue Zhao

Submitted in partial fulfillment of the
Requirements for the degree
of Doctor of Philosophy
in the Graduate School of Arts and Sciences

COLUMBIA UNIVERSITY

2012

Abstract

Quantum Hall Transport in Graphene and its Bilayer

Yue Zhao

Graphene has generated great interest in the scientific community since its discovery because of the unique chiral nature of its carrier dynamics. In monolayer graphene, the relativistic Dirac spectrum for the carriers results in an unconventional integer quantum Hall effect, with a peculiar Landau Level at zero energy. In bilayer graphene, the Dirac-like quadratic energy spectrum leads to an equally interesting, novel integer quantum Hall effect, with a eight-fold degenerate zero energy Landau level.

In this thesis, we present transport studies at high magnetic field on both monolayer and bilayer graphene, with a particular emphasis on the quantum Hall (QH) effect at the charge neutrality point, where both systems exhibit broken symmetry of the degenerate Landau level at zero energy. We also present data on quantum Hall edge transport across the interface of a graphene monolayer and bilayer junction, where peculiar edge state transport is observed.

We investigate the quantum Hall effect near the charge neutrality point in bilayer graphene, under high magnetic fields of up to 35 T using electronic transport measurements. In the high field regime, we observe a complete lifting of the eight-fold degeneracy of the zero-energy Landau level, with new quantum Hall states corresponding to filling factors $\nu = 0$, 1, 2 & 3. Measurements of the activation energy gap in tilted magnetic fields suggest that the Landau level splitting at the newly formed

ν =1, 2 & 3 filling factors does not exhibit low-energy spin flip excitation. These measurements are consistent with the formation of a quantum Hall ferromagnet. In addition, we observed insulating behavior in the two terminal resistance of the ν =0 state at high fields.

For monolayer graphene, we report on magneto-resistance measurements at the broken-symmetry of the zero-energy Landau level, using both a conventional two-terminal measurement of suspended graphene devices, which is sensitive to bulk and edge conductance, and a Corbino measurement on high mobility on-substrate devices, which is sensitive to the bulk conductance only. At $\nu = 0$, we observe a vanishing conductance with increasing magnetic fields in both cases. By examining the resistance changes of this insulating state with varying perpendicular and in-plane fields, we probe the spin-active components of the excitations in total fields of up to 45 Tesla. Our results strongly suggest that the $\nu = 0$ quantum Hall state in single layer graphene is not spin polarized, while a spin-polarized state with spin-flip excitations forms at $\nu = 1$.

For monolayer and bilayer graphene junction system, we first present a surface potential study across the monolayer/bilayer interface. Then we present experimental investigations of the edge state transition across the interface in the quantum Hall regime. Both monolayer graphene (MG) and bilayer graphene (BG) develop their own Landau levels under high magnetic field. While transport measurements show their distinct quantum Hall effects in the separate parts of the monolayer and bilayer respectively, the transport measurement across the interface exhibits unusual transverse transport behavior. The transverse resistance across the MG/BG interface is asymmetric for opposite sides of the Hall bar, and its polarity can be changed by reversing the magnetic field direction. When the quantum Hall plateaus of MG and BG overlap, quantized resistance appears only on one side of the Hall bar electrode pairs that sit across the junction. These experimental observations can be ascribed

to QH edge state transport across the MG/BG interface.

We also present sample fabrication details, particularly the efforts to eliminate mobility-limiting factors, including cleaning polymer residue from the electron beam lithography process via thermal annealing and removing/changing the substrate by suspending multi-probe graphene devices.

Contents

List of Figures

List of Tables

Acknowledgments

First and foremost, my sincerest gratitude goes to my advisor, Prof. Philip Kim. This dissertation would not have been possible without your immense knowledge, enlightening instruction, impressive kindness and patience. You have walked me through all the stages of my graduation education, from a foreign student who just entered graduate school, to an independent researcher. You taught me how to perform good experimental work, both consciously and unconsciously. Your enthusiasm and joy for research are contagious during the tough times in the Ph.D. pursuit. I am extremely fortunate to have you to be my advisor.

My fellow group members have been a irremovable part of both my professional and personal time at Columbia. Thank you to Paul Cadden-Zimansky; during the magnet times in Tallahassee, I learned not only the cryogenic techniques, but also your approach to answer questions; I also learned a lot from your excellent writing skills and presenting skills; and riding to NHMFL in your car is much more enjoyable than walking alone from the alumni village; special thanks for proofreading this thesis as well. Thank you to Melinda Han for being so considerate all the time, I learnt most of the fabrication skills from you. Thank you to Yuanbo Zhang for teaching me to start my first measurement in the lab. Thank you to Meninder S. Purewal for your patience at your busiest time. Thank

you to Yuri Zeuv; you are the first person I met in the lab, and from you I got good advices to initiate the job search. Thank you to Andrea Young; your self-confidence and enthusiasm for research is contagious and motivational, and the discussions with you are always helpful. Thank you to Mitsuhide Takekoshi for the snacks and good conversations (in both English and Japanese). Thank you to Fereshte Ghahari; we share the stresses and the joys when meeting the deadlines of magnet-time, and your persistence in research impressed me. Thank you to Dmitri Efetov; I admire your ability to balance between work and life. Thank you to Youngjun Yu; I very much appreciate your diligence in research and willingness to help. Thank you to Barbaros Oezyilmaz, Kirill Bolotin and Pablo Jarillo-Herrero; your creativity and confidence in making anything possible intrigue me a lot. Thank you to Byung Hee Hong for bringing me new perspectives of graphene research in the application side. Thank you to Keunsoo Kim for sharing the CVD method for graphene growth. Thank you to Vikram Deshpande for the short but enlightening conversations. Thank you for all the help, and the joys and pleasures.

I am thankful to the following people I have worked with in friend labs. I have learned things from all of you. Thanks to Kinfai Mak, Hugen Yan, Chun Hung Lui, and Jun Yan for expanding my knowledge in optical physics of graphene. Thanks to Seok Ju Kang, Bumjung Kim, Seokhoon Ahn and Gwan Hyoung Lee for their support from the chemistry side.

I am also grateful to the collaborators outside Columbia. Thank you to Zhigang Jiang (we worked together when I first started the experiments in NHMFL) for the helpful discussions and experimental help on bilayer graphene measurement in NHMFL. Thank you to Mikito Koshino in Tohoku University, Japan, for the insightful theoretical support on the study

of graphene monolayer and bilayer junction.

It is a great privilege for me that most of the work in this thesis could be done in the National High Magnetic Field Laboratory in Tallahassee (NHMFL), Florida. Also thank you to S. T. Hannahs, E. C. Palm, and T. P. Murphy for your generous experimental assistance.

With the friendly support of the faculty members at Columbia and staff members of Physics Department, my life at Columbia got much easier. Thank you to Prof. Allan S. Blaer for giving me a lot of suggestions in the beginning as a graduate student. Thank you to Prof. Tony Heinz and Prof. Colin Nuckolls for the invaluable advices and encouragements which guide me to find out my next career step. Thank you Lalla Grimes for your warmest kindness. Many thanks to Lydia Argote, Giuseppina Cambareri, John T Carr, III, Yasmin Yabyabin and Randy Torres, for your help over the years.

The last, I would like to thank my friend and family for their understanding and support. Thank you to my best friend Siva Ho, not only for suffering from the first draft of this thesis and also for being a constant source of joy and support over the years. Thank you mom; you sacrificed your life for me since I was born and provides me unconditional love and care. Thank you dad; you taught me that nothing is impossible to a willing heart, and I would not have made it so far without your encouragement and gratuitous belief. Thank you to my husband Xin Wang; these past six years have not been easy for both you and me, academically and personally, but your support has never wavered even when I was irritable and depressed.

Thank you everybody!

Chapter 1

Introduction

Graphene, a planar atomic sheet of carbon atoms bonded together in a honeycomb lattice, is the first truly two-dimensional electron gas (2DEG) system experimentalists have ever realized. Since its first isolation (Novoselov *et al.*, 2004), graphene has attracted tremendous interest within the scientific community from both a fundamental physics and an engineering point of view for the rich new physics arising from its unique electronic band structure and the great prospect of applications, compared with other well-known 2DEG semiconductor systems.

Prior to the start of graphene research, the experimental study of the quasi-2DEG systems has been pursued primarily by confining electrons in semiconductor structures, such as GaAs-based heterostructures, silicon metal oxide semiconductor field effect transistors (Si-MOSFETs) in inversion mode, or quantum wells. These explorations have already produced remarkable discoveries in quantum physics. One of the most prominent phenomena is the integer Quantum Hall effect (IQHE) under high magnetic field, discovered by Klitzing *et al.* (1980) in Si-MOSFETs with tunable carrier density via a back gate. The IQHE exhibits a quantized Hall conductivity in units of e^2/h with vanishing longitudinal conductivity. Shortly after the discovery of the IQHE, the fractional quantum Hall effect (FQHE) was observed by Tsui *et al.* (1982), where instead of an integer quantization of the Hall conductivity, quantization occurs at fractional values of e^2/h. The FQHE was realized in higher mobility samples of GaAs-based heterojunctions using a cleaner growth method: Molecular-

beam-epitaxy. Unlike the immediate understanding of IQHE by Landau level (LL) formation due to single particle localization, it took much longer time for people to get a not-yet-complete understanding of the FQHE. It is proposed by Jain (1989) that FQHE states are the result of localization of collective electronic excitations in strongly correlated electron systems.

The previously studied quasi-2DEG systems have active regions for electron conduction that are hundreds of atoms thick. The 2DEG in graphene, as a one-atom thick material, has many exciting advantages. It is possible to directly probe the surface of the electrons in graphene, e.g. using scanning tunneling microscope (STM) or scanning kelvin probe microscope (SKPM), since it is not embedded in a supporting medium. Another immediate advantage is the tunability of charge carrier density from electrons to holes via a field effect gate.

Graphene also has high mobility due, in part, to its nearly defect free lattice structure. On SiO_2 substrates, the usual carrier mobility is a few thousand cm^2/Vs, and is limited by scattering mechanisms, e.g., charged impurities (Ando, 2006; Hwang *et al.*, 2007), surface roughness (Ishigami *et al.*, 2007; Katsnelson and Geim, 2008), and the optical phonons from the substate (Fratini and Guinea, 2008; Chen *et al.*, 2008), etc. Today the field effect mobility of carriers in graphene can be on the order of 100,000 cm^2/Vs by removing or changing the substrate, i.e. suspending the graphene sample (Bolotin *et al.*, 2008; Du *et al.*, 2009), or placing the graphene sample on a hexagonal boron nitride substrate (Dean *et al.*, 2010). Although the highest mobility graphene is still lower than the cleanest GaAs-based systems, which is not limited by strong long-range polar optical phonon scattering, graphene is expected to have decent mobility over a wide range of temperatures (from 50K to 500K) (Hwang and Das Sarma, 2008; Chen *et al.*, 2008), and an intrinsic mobility that can be as high as 200,000 cm^2/Vs at room temperature (Morozov *et al.*, 2008), making graphene a desirable material for electronic applications.

Most importantly, in contrast to the parabolic dispersion relation in other 2DEG systems, the carriers in graphene exhibit a linear energy dispersion relation. This highly unusual low energy band structure is analogous to a relativistic system where the charge carriers are described by the massless Dirac equation rather than the non-relativistic Schrödinger equation (Haldane, 1988; Zheng and Ando, 2002), allowing access to quantum electrodynamics in a simple but elegant condensed matter system. The low-energy band structure of Bernal stacked bilayer graphene is approximately gapless and quadratic (McCann and Falko, 2006), which is found to be equally interesting, but distinct from monolayer graphene.

The main motivation of this thesis is the study of quantum transport in both monolayer and bilayer graphene, with an emphasis on their peculiar zero energy states, and the investigation of the interface boundary of monolayer and bilayer graphene junction(MG/BG) systems as well. In this introductory chapter, we will present a brief history of graphene, describe the lattice structures of monolayer and bilayer graphene and derive their underlying electronic band structure. We will also discuss in detail the relevant theories of the quantum Hall effect in bilayer and monolayer graphene.

1.1 A brief history of graphene: from conception to realization

Carbon is one of the most important elements on earth owing to its great bonding flexibility and strength. It forms a variety of allotropes, from soft graphite to super hard diamond, from nearly perfect spherical buckyballs to their cylindrical cousins (carbon nanotubes). In the past fifteen years, research into carbon allotropes were recognized with the Nobel Prize twice (the discovery of fullerenes was awarded the

1996 Nobel Prize in Chemistry and graphene won Geim and Novoselov the 2010 Nobel Prize in Physics).

Graphene can be viewed as the basic structural element for all the sp^2 bonded carbon allotropes. As shown in Fig. 1.1, one may increase the dimensionality by stacking graphene layers via van der Waals force to form three-dimensional (3D) graphite, or decrease the dimensionality by either rolling up the sheet to make a one-dimensional (1D) carbon nanotube, or sew together a small area of a graphene sheet into a nearly perfect zero-dimensional (0D) sphere with twelve pentagons and twenty hexagons (Castro Neto *et al.*, 2009). Unlike the discovery of bulkyballs (theoretically proposed by Yoshida and Osawa (1971) with experimental realization by Kroto *et al.* (1985)), it took experimentalists almost a half century to realize a graphene system (Novoselov *et al.*, 2004) since it was first theoretically studied (Wallace, 1947).

The first exploration of graphene band structure was done by Wallace (1947), who used a tight binding model of graphene as a step towards understanding bulk graphite. Although the existence of infinitely sized two-dimensional (2D) crystals was considered not realistic at finite temperature due to thermal fluctuation in the third dimension (Landau and Lifshitz, 1980; Peirls, 1934), the efforts to isolate graphene have been continuous since the theoretical studies shows graphene to be a fascinating 2DEG system with unique massless Dirac fermions (McClure, 1956; Slonczewski and Weiss, 1958; Semenoff, 1984; Fradkin, 1986; Haldane, 1988).

The breakthrough to isolate graphene was made by Novoselov *et al.* (2004). The method is called mechanical exfoliation. Since graphite contains weakly coupled graphene layers, monolayer graphene is peeled off by chance if one gently rubs Scotch tape on an SiO_2 substrate with graphite pieces in between. The randomly distributed graphene pieces are identified by optical microscope with a visible contrast difference (Note that the thickness of SiO_2 layer is tuned to 300 nm in order to maximize this contrast). Raman spectroscopy is a faster technique that can also identify the number

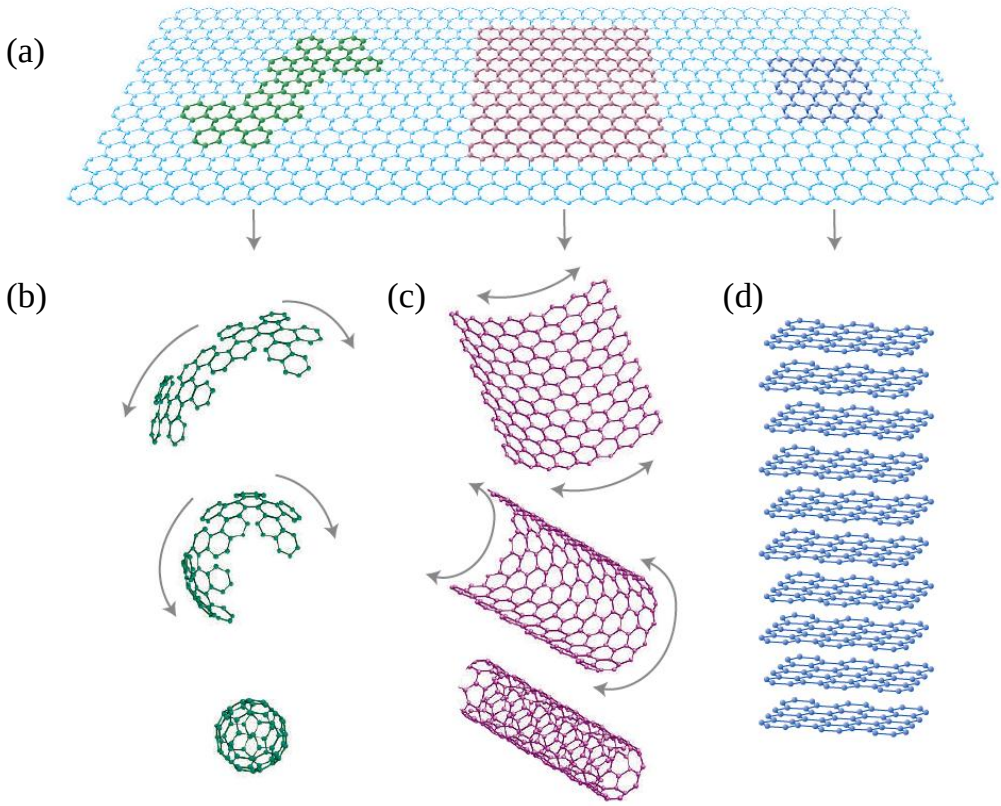

Figure 1.1: (a) Graphene, a two dimensional hexagonal lattice of carbon atoms, as the basic building block for other sp2 bonded carbon allotropes; (b) C_{60}, a 0D bulkyball, where curvatures are introduced by sewing graphene into a nearly perfect sphere via carbon pentagons; (c) 1D Carbon nanotube, a rolled up cylinder of graphene; (d) 3D Graphite: a stack of graphene layers via Van der Waals force. Figure from Ref (Geim and Novoselov, 2007).

of layers precisely, compared to human experience and judgment of the contrast or measurement of thicknesses by contact mode Atomic force microscope (AFM).

The existence of graphene does not necessarily contradict the prediction that perfect 2D crystals are unrealistic. Since the instability of 2D limit works for infinite sheet (Peirls, 1934; Landau and Lifshitz, 1980), the finite size and boundary con-

ditions in most graphene samples make it less relevant. Graphene is found to be microscopically corrugated (rippled) even in suspended cases, and it is believed the intrinsic ripples could be necessary for the structural stability in 2D graphene (Meyer *et al.*, 2007).

This 2D system is sufficiently robust even with charge traps, roughness and other defects. The observation of an anomalous QHE (Novoselov *et al.*, 2005a; Zhang *et al.*, 2006) provided solid evidence that this system is indeed the 2DEG theorists expected. Detailed introduction of the QHE in graphene systems is discussed in the following section.

The mechanical exfoliation method provides graphene samples with sufficient quality for fundamental studies, though it is obviously still unsuitable for real-world applications due to the unpredictable locations of exfoliated graphene flakes and their limited size. Recent progress in sample preparation has allowed the following scalable techniques to grow graphene: Large areas of graphene can be grown epitaxially either by thermal decomposition of silicon carbide, or via chemical vapor deposition (CVD) on metal surfaces at high temperature ($T > 1000°$C). The resulting quality is nearly comparable to that of mechanically exfoliated graphene from graphite crystal, with rather high mobility and observation of IQHE/FQHE (Petrone, 2011).

There are two ways of introducing band gap in graphene systems. In monolayer graphene, by cutting it into nanoribbons (Han *et al.*, 2007), an up-to 500 meV energy gap is reported in a 2.5 nm zigzap graphene nanoribbon (GNR) (Tapaszto *et al.*, 2008). The other is to apply an electrical field vertical to the two layers of bilayer graphene, where the observed band gap opening can be up to 250 meV (Zhang *et al.*, 2009; Ohta *et al.*, 2006). Although the controllability of GNR's edges and the growth of bilayer graphene is limited, graphene systems are still considered promising electric materials, capable of preserving Moore's Law (i.e. continue the electronic miniaturization) as silicon-based technology becomes obsolete. On-going research in this direction shows

great promise with ample chance of potential applications.

1.2 Monolayer graphene

1.2.1 Lattice structure and electronic band structure

The electronic structure of carbon atom is $1s^2 2s^2 2p^2$. Each carbon atom in graphene lattice forms three sp^2 orbitals, and leaves one p_z-orbital perpendicular to x-y plane. Since the sp^2 orbitals have a natural tendency to arrange themselves in a plane at 120°, graphene has a hexagonal lattice structure, as shown in Fig. 1.2. Note that a honeycomb lattice can be considered as a Bravais lattice with a two-atom basis. Thus in one primitive cell, enclosed by a grey dotted Parallelogram in Fig. 1.2, there are two inequivalent atoms, colored red and blue. The distance between two nearest carbon atoms is a_0 =1.42 Å. One may choose the primitive lattice vector to be the following for convenience:

$$\mathbf{a_1} = a(\frac{\sqrt{3}}{2}, \frac{1}{2}), \quad \mathbf{a_2} = a(\frac{\sqrt{3}}{2}, -\frac{1}{2}) \tag{1.1}$$

where $a = \sqrt{3}a_0$=2.46 Å.

The reciprocal graphene lattice is also a honeycomb-like lattice with primitive vectors defined by $\mathbf{a_i} \cdot \mathbf{b_j} = 2\pi\delta_{ij}$:

$$\mathbf{b_1} = \frac{2\pi}{a}(\frac{1}{\sqrt{3}}, 1), \quad \mathbf{b_2} = \frac{2\pi}{a}(\frac{1}{\sqrt{3}}, -1) \tag{1.2}$$

The first Brillouin zone of the reciprocal lattice, as shown in Fig. 1.2(b), is bounded by the planes bisecting the vectors to the nearest reciprocal lattice points, and it is rotated with respect to the original hexagons by $\pi/2$.

The six corner points of the first Brillouin zone are called K-points. We consider only the two inequivalent corners: K and K' as in Fig. 1.2(b). Their positions in momentum space are given by:

$$\mathbf{K} = \frac{2\pi}{a}(\frac{1}{\sqrt{3}}, \frac{1}{3}), \quad \mathbf{K}' = \frac{2\pi}{a}(\frac{1}{\sqrt{3}}, -\frac{1}{3}) \tag{1.3}$$

Starting with such a perfectly flat, free-standing graphene sheet with the standard periodic boundary condition, one can approach the band structure using a tight binding model (i.e. linear combination of atomic orbitals), where only nearest neighbor hopping is considered. For example, for the A sublattice atoms in Fig. 1.2, the real space vectors of the three nearest neighbors are given by:

$$\boldsymbol{\delta}_1 = 2a\left(\frac{-1}{\sqrt{3}}, 0\right), \quad \boldsymbol{\delta}_2 = \frac{a}{2}\left(\frac{-1}{\sqrt{3}}, 1\right), \quad \boldsymbol{\delta}_3 = \frac{a}{2}\left(\frac{-1}{\sqrt{3}}, -1\right).$$

The Hamiltonian is written as the following:

$$\mathbf{H}_{MG}^{TB} = -t\sum_{i,j,\sigma}(a_{i\sigma}^{\dagger}b_{j\sigma} + H.c.) \tag{1.4}$$

where the orbital on atom i with spin σ is denoted by (i, σ); $a_{i\sigma}^{\dagger}$ or $b_{i\sigma}^{\dagger}$ is the creation operator in for the atom in A or B sublattice; t is the nearest neighbor hopping matrix element (the energy scale of the π-band is 2.8 eV.) One then writes a two component wavefunction with a similar pseudospin index to indicate the contribution from sublattices A and B (apart from the real-spin-1/2 index.)

$$\begin{pmatrix} \alpha_{\mathbf{k}} \\ \beta_{\mathbf{k}} \end{pmatrix} = \sum_i e^{i\mathbf{k}\cdot\mathbf{R_i}} \begin{pmatrix} a_i^{\dagger}e^{-i\mathbf{k}\cdot\boldsymbol{\delta}/2} \\ b_i^{\dagger}e^{i\mathbf{k}\cdot\boldsymbol{\delta}/2} \end{pmatrix} \tag{1.5}$$

Here, $\mathbf{R_i}$ indicates a reference point for unit cell i, and $\boldsymbol{\delta}$ is a vector pointing from sublattice A to B. We choose the reference point to be at A as shown in the enclosed

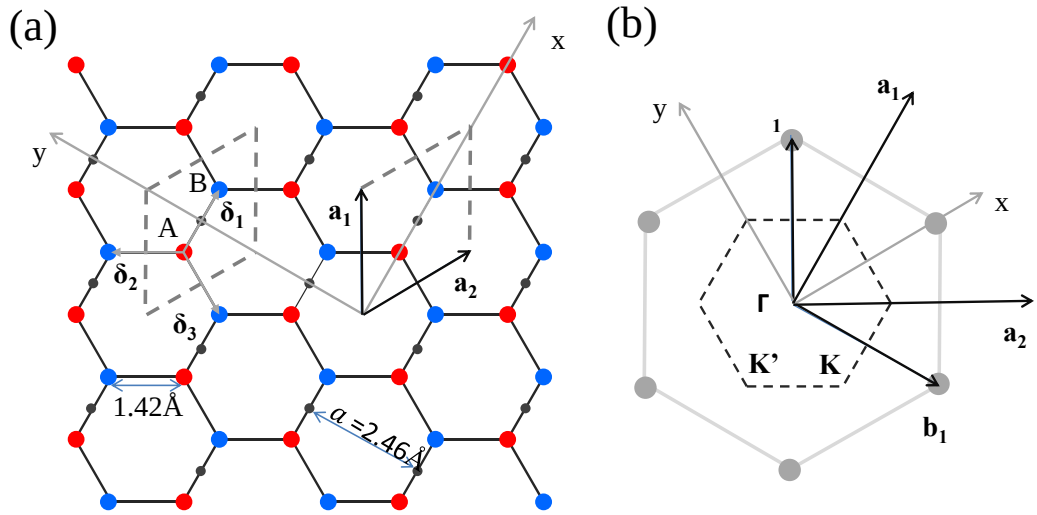

Figure 1.2: (a) graphene lattice structure in real space: carbon atoms are located at the corners of the hexagons and the lines are indications of the chemical bonds of the sp^2 orbitals. The grey dotted line shows one primitive cell with two inequivalent atoms A and B, denoted by red and blue colors. The primitive vectors $\mathbf{a_1}$ and $\mathbf{a_2}$ are shown under the x- and y- coordinates. (b) The reciprocal lattice with the first Brillouin zone.The grey dots indicates the reciprocal lattice points, while the area enclosed with a dotted hexagon is the first Brillouin zone.

unit cell in Fig. 1.2. Since the $e^{\pm i\mathbf{k}\cdot\boldsymbol{\delta}/2}$ in the spinor components are chosen, the Hamiltonian in k-space is then simplified to be purely off-diagonal:

$$\mathbf{H_k} = \begin{pmatrix} 0 & \Delta_{\mathbf{k}} \\ \Delta^*_{\mathbf{k}} & 0 \end{pmatrix} \tag{1.6}$$

where $\Delta_{\mathbf{k}} = -t\sum_{j=1,2,3} e^{i\mathbf{k}\cdot\boldsymbol{\delta}_j}$ and $\boldsymbol{\delta}_j$ refer to the nearest neighbor vectors.

The eigenenergy is obtained as following:

$$\begin{aligned} E_{\mathbf{k}} &= \pm\Delta_{\mathbf{k}} \\ &= \pm t\sqrt{1 + 4\cos\left(\frac{\sqrt{3}a}{2}k_x\right)\cos\left(\frac{a}{2}k_y\right) + 4\cos^2\left(\frac{a}{2}k_y\right)} \end{aligned} \tag{1.7}$$

It is interesting that, as shown in the Fig. 1.3 main panel, the energy gap vanishes at exactly the corners of the first Brillouin zone ($\mathbf{K}$ and $\mathbf{K}'$).

To take a closer look at this low energy spectrum, we expand the energy expression around $\mathbf{K}$, by taking $\mathbf{q} = \mathbf{k} - \mathbf{K}$. The eigenenergy is reduced to the following:

$$\begin{aligned} \Delta_{\mathbf{K}}(\mathbf{q}) &= -\frac{3\sqrt{3}}{2a}te^{-iK_x a/\sqrt{3}}(iq_x - q_y)\left(+O(q)^2\right) \\ &\backsimeq \hbar v_f(q_x + iq_y) \end{aligned} \tag{1.8}$$

with $v_f = \frac{\sqrt{3}ta}{2\hbar} \backsimeq 10^6$ m/s.

As shown in the inset of Fig. 1.3, the low energy spectrum shows a linear dispersion relation near the $\mathbf{K}$ and $\mathbf{K}'$ points (also called Dirac points).

Similarly, the expansion around the K' point gives $\Delta_{\mathbf{K}'}(\mathbf{q}) = \Delta^*_{\mathbf{K}}(\mathbf{q})$, where the helicity is preserved for the same convention. Near the $\mathbf{K}$ and $\mathbf{K}'$ points, the Hamiltonian is rewritten as the following:

$$\mathbf{H}_{\mathbf{k}} = \begin{pmatrix} 0 & \Delta_{\mathbf{k}} \\ \Delta^*_{\mathbf{k}} & 0 \end{pmatrix} = \hbar v_f \boldsymbol{\sigma}\cdot\mathbf{q} \tag{1.9}$$

$$E_q = \pm\hbar v_f|q| \tag{1.10}$$

where $\boldsymbol{\sigma}$ is the Pauli vector and $\mathbf{q}$ is the quasiparticle momentum with respect to the $\mathbf{K}$ point.

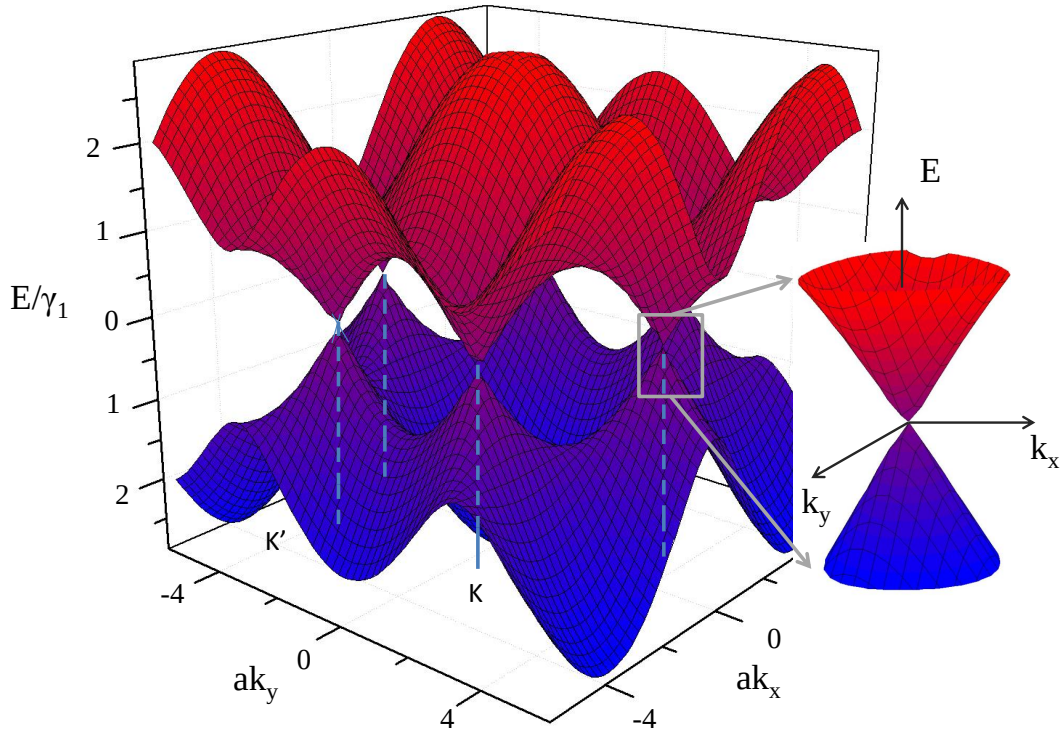

Figure 1.3: Main panel:Graphene band structure calculated from the tight binding model; right inset: a zoom-in at low energy scale, showing the linear dispersion relation.

It is noteworthy that Eq. 1.9 is exactly a Dirac Hamiltonian for a relativistic massless particle with an intrinsic degree of freedom that resembles the spin degree of freedom in the ordinary Dirac equation, with the speed of light replaced by the fermi velocity $v_f \backsimeq c/300$. The spinor introduced in this description is often called pseudospin, since it is also described by a Pauli matrix.

The eigenfunction near the Dirac points are written as the following:

$$\Psi^{\pm}_{\mathbf{K}} = \frac{1}{\sqrt{2}} \begin{pmatrix} e^{i\theta_q/2} \\ \pm e^{-i\theta_q/2} \end{pmatrix}, \quad \text{where } \tan\theta_{\mathrm{q}} = \mathrm{q_x}/\mathrm{q_y} \tag{1.11}$$

This state is characterized by its "helicity" – that as the quasiparticle momentum rotates once around the Dirac point, the phase of the eigenfunction changes by π. In graphene, the helicity is sometimes called chirality since electrons with momentum **k** and -**k** are also connected to the direction of pseudospin.

Although in this tight binding model the higher order perturbations are ignored to obtain this linear dispersion, it has been demonstrated that the approximation holds well for energies smaller than 1 eV (Plochocka *et al.*, 2008; Bostwick *et al.*, 2007) when higher order terms are taken into account.

Considering the variation in 2D k-space, the variation of the density of states (DOS) for a 2DEG, N(E), is determined by

$$dN = g\frac{2\pi k}{(2\pi/L)^2}dk \tag{1.12}$$

where g is the spin degeneracy of the carriers. For a conventional 2DEG with finite effective carrier masses m^*, the dispersion relation is described by $E = \frac{\hbar^2 k^2}{2m^*}$, and the DOS is a step function

$$N(E) = \frac{m^*}{\pi\hbar^2}\theta(E) \tag{1.13}$$

For graphene, since the massless Dirac fermions are described by a linear dispersion $E = \pm\hbar v_f k$, its DOS is then linear

$$N(E)dE = \frac{2}{\pi\hbar^2 v_f^2}EdE \tag{1.14}$$

The carrier density is:

$$n_s = \int_0^{E_f} \frac{2\pi}{\hbar^2 v_f^2}EdE = \frac{k_f^2}{\pi} \tag{1.15}$$

The differences between Dirac fermions and Schrödinger fermions can be observed in transport measurements. One of the most notable examples is the unconventional

quantum Hall effect discussed in the following sections.

1.2.2 Introduction to quantum Hall effect

In a magnetic field B, free electrons are forced to circulate in cyclotron orbits. In 3D metals, this leads to the classical Hall effect (Hall, 1879). At the quantum level, the effect is more spectacular due to the quantization of the closed orbits (as seen in experimental observations such as the De Haas-van Alphen effect and Shubinikov-de Haas oscillations in 3D metals). In 2DEG systems, Klitzing *et al.* (1980) observed a number of plateaus in the Hall resistance corresponding to the value of h/ne^2(with n an integer); the transverse resistance became zero within experimental error over the range of each plateau. The plateaus sit on integer filling factors corresponding to at $\nu = n_s h/eB$, where n_s is the sheet carrier density. This is the integer quantum Hall effect.

The fact that R_{xy} is exactly quantized at e^2/h forms a basis for metrology, since it is accurate and universal to all 2DEG systems. In the following text, we will discuss the formation of Landau levels (LLs) and the existence of edge states to explain IQHE and the role of disorder.

Let us consider a 2DEG with a finite width (W) and length (L) under a perpendicular magnetic field, as illustrated in Fig. 1.4. We approach the energy spectrum of such a system in the bulk by solving the Schrödinger equation of a single particle semiclassically (Halperin, 1982).

$$E\psi = \frac{1}{2m}(\mathbf{p} - \mathbf{eA/c})^{\mathbf{2}}\psi \tag{1.16}$$

By choosing coordinates such that the vector potential $A_y = -Bx, A_x = 0$, the equation is simplified to a one-dimensional harmonic oscillator problem:

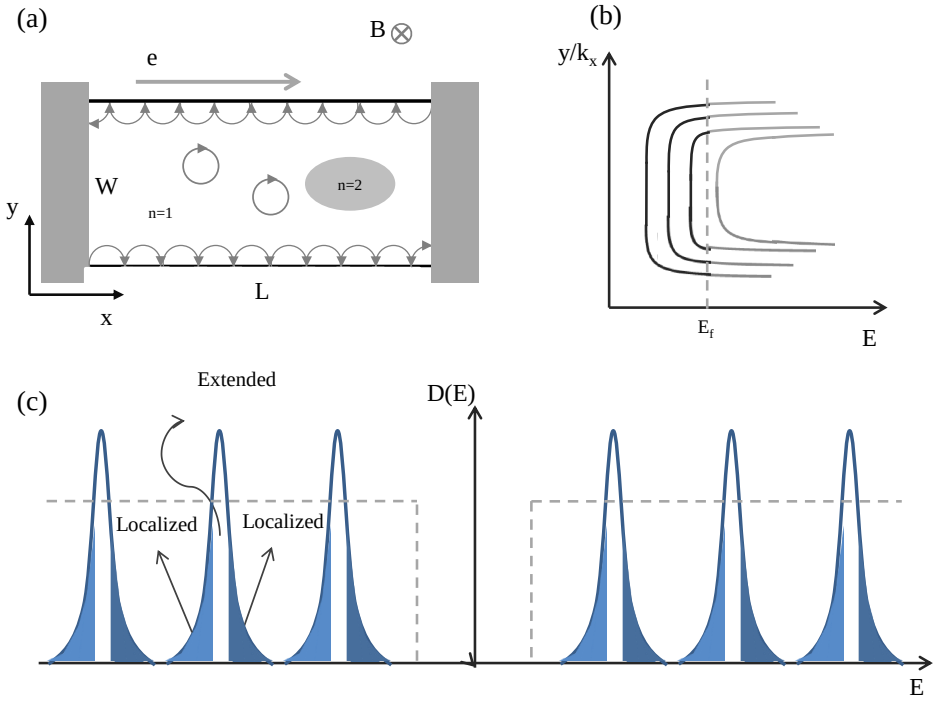

Figure 1.4: Schematics of edge state and broadening of LLs:(a) a 2DEG strip, with length L and width W under perpendicular magnetic field B, has a large area quantized at $n = 1$ while, due to a local potential difference, a tiny $n = 2$ LL forms in the middle of the strip. Grey circles with arrows indicate the cyclotron motion. (b) LLs on the edges; (c) DOS with broadened LLs.

$$E\psi(x) = (\frac{1}{2m}p_x^2 + \frac{1}{2}m\omega_c^2(x - x_0)^2)\psi(x), \quad x_0 = p_y l_B^2, \tag{1.17}$$

$l_B = \sqrt{\frac{\hbar}{eB}}$ is the magnetic length. The energy spectrum:

$$E_n = \hbar\omega_c(n + \frac{1}{2}) \tag{1.18}$$

describes the Landau levels (LL).

Considering the edge boundary condition: $\psi(x = 0, w) = 0$, and the approximately parabolic band structure of the conduction/valence band edges in momentum space, the energy of the LLs increase as they move away from the parabolic potential minimum (i.e. approach to the edge), as shown in Fig. 1.4. The conducting channels originating from the LLs along the edges are considered edge states. According to the Landauer-Büttiker formalism (Büttiker, 1988), at filling factor $\nu = n$, there are n conducting edge states, corresponding to a quantized Hall voltage $V_H = Ih/ne^2$. Since the edge states propagate along the same direction, backscattering can be neglected in samples with $W \gg l_B$ where electrons would have to tunnel to the opposite edge for backscattering to occur. The absence of back scattering in the quantum Hall regime leads to a vanishing longitudinal resistivity and thus dissipationless transport.

$D(E)$ for such a 2DEG system under high magnetic fields can be expressed by $D(E) = \frac{g_s}{2\pi l_B^2}\delta(E - E_n)$. However, in realistic graphene systems, where there are spatial potential fluctuations, the energies of the LLs change with the varying potential. Hence the DOS is broadened by localized states, which results in the observation of a finite width in the QH plateaus.

1.2.3 Quantum Hall effect in monolayer graphene

Let us now analyze the energy levels of monolayer graphene in a magnetic field. One can treat the quasimomentum $\mathbf{q}$ in the Hamiltonian(equation 1.9)with the standard substitution "$\mathbf{p} \to \mathbf{p} - e\mathbf{A} \equiv \boldsymbol{\pi}$":

$$\mathbf{H} = v_f \begin{pmatrix} 0 & \boldsymbol{\pi}_x + i\boldsymbol{\pi}_y \\ \boldsymbol{\pi}_x - i\boldsymbol{\pi}_y & 0 \end{pmatrix} \tag{1.19}$$

Note that $[\boldsymbol{\pi}_x, \boldsymbol{\pi}_y] = ie\hbar B_z$ It is convenient to rewrite the Hamiltonian by setting

$\mathbf{\Pi}_i = l_B \boldsymbol{\pi}_i/\hbar$:

$$\mathbf{H} = \frac{\hbar v_f}{l_B} \begin{pmatrix} 0 & \mathbf{\Pi}_x + i\mathbf{\Pi}_y \\ \mathbf{\Pi}_x - i\mathbf{\Pi}_y & 0 \end{pmatrix} \tag{1.20}$$

Since the commutation relation of $\mathbf{\Pi}_x$ and $\mathbf{\Pi}_y$ is: $[\mathbf{\Pi}_x, \mathbf{\Pi}_y] = i$, taking the square of Eq. 1.20 gives:

$$\mathbf{H}^2 = \frac{\hbar^2 v_f^2}{l_B^2} \begin{pmatrix} \mathbf{\Pi}_x^2 + \mathbf{\Pi}_y^2 + 1 & 0 \\ 0 & \mathbf{\Pi}_x^2 + \mathbf{\Pi}_y^2 - 1 \end{pmatrix} \tag{1.21}$$

which is exactly a harmonic oscillator Hamiltonian with eigenvalues $\frac{\hbar^2 v_f^2}{l_B^2}(2|n| + 1 \pm 1)$ and $|n| = 0, 1, 2, ...$, thus the eigenvalues of Eq. 1.20 are:

$$E_n = \pm\sqrt{2\hbar v_f^2 |n| eB}, \qquad |n| = 0, 1, 2, ... \tag{1.22}$$

The structure of the LLs, as shown in Fig. 1.5(a), leads to an unconventional half-integer quantum Hall effect in graphene, which was predicted by theory (Peres *et al.*, 2006; Gusynin and Sharapov, 2005), and then observed experimentally by two research groups independently (Novoselov *et al.*, 2005a; Zhang *et al.*, 2005).

Compared with the LLs obtained in conventional 2DEGs (discussed in the previous subsection), where $E_n = \hbar\omega_c(n + 1/2)$, $n \in Z$, it should be noted that there is a distinctive LL at $E = 0$ as the consequence of the electron-hole symmetry in graphene. The zero energy LL is formed equally from electron and hole states leading to a half-integer shift in the number of flux quanta needed to fill an integer number of LLs. The total degeneracy of each level is 4, 2 from the spin degeneracy, 2 from the two Dirac cones (valley degeneracy). Thus the QH plateaus occur at the filling factors

$$\sigma_{xy} = \nu e^2/h, \quad \nu = 4(n + 1/2), n \in Z \tag{1.23}$$

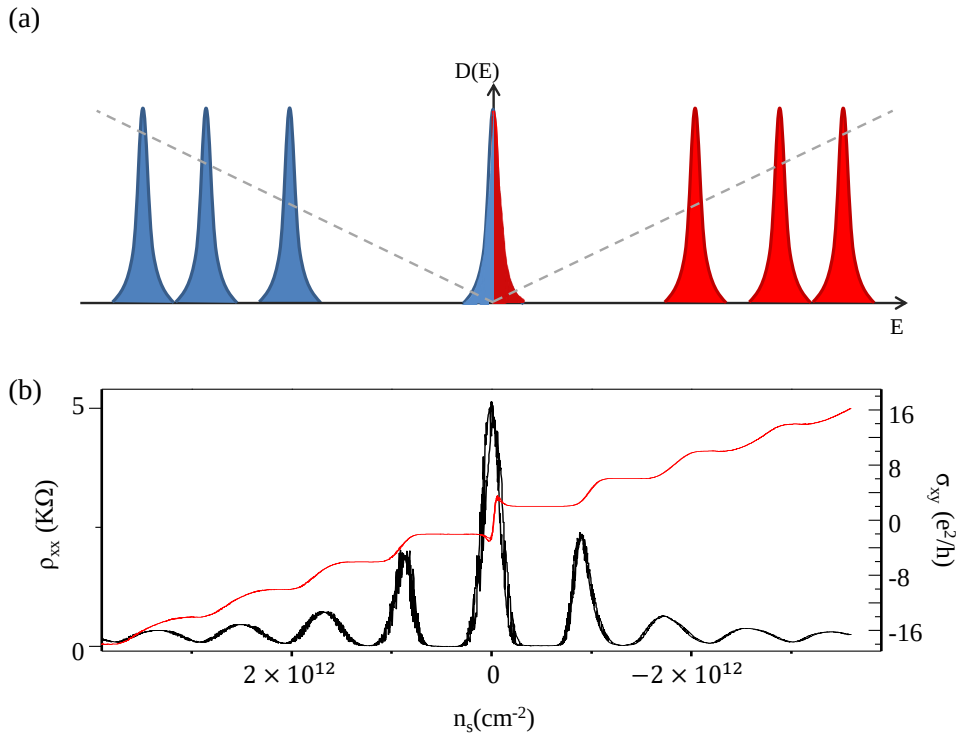

Figure 1.5: (a) Unevenly spaced Landau levels in monolayer graphene: filled colors indicate electrons (red) and holes (blue); dashed lines show the density of states at zero magnetic field. (b) longitudinal resistivity (ρ_{xx} in black) and Hall conductivity(σ_{xy} in red) as a function of charge carrier density, at $B = 9$ T, $T = 7$ K.

Note that $\nu = -2$ and $\nu = 2$ correspond to the emptying and filling of the $E_{n=0} = 0$ LL.

Since the LLs are unevenly spaced in energy (proportional to $\sqrt{n}$), and according to Eq. 1.15 $E_f \propto \sqrt{n_s}$, the quantum Hall plateaus are evenly spaced with varying carrier density n_s, as shown in Fig. 1.5.

With particle-hole symmetry the LL at $E = 0$ is a very unique one. At K or K' points with $E = 0$, the wavefunctions reside entirely on the A or B sublattices, while

for other non-zero energy level, there is equal chance them to be on each sublattice. Thus for $n = 0$ LL, the valley degeneracy (isospin) is the same as the sublattice degeneracy (pseudospin). Also note that near the charge neutrality point, real graphene samples are subject to the formation of electron-hole puddles (Martin *et al.*, 2008). Due to lack of screening, disorder plays an important role in ordering states in this regime.

In a quantum Hall ferromagnetism picture, at high magnetic field the inherent four-fold symmetry of monolayer graphene can be broken because both valley and spin degrees of freedom can be polarized due to the strong Coulomb interactions (Nomura and MacDonald, 2006) (Zeeman energy is usually enhanced by Coulomb interactions). These ordered states have been widely observed as QH plateaus appearing at new filling factors (Zhang *et al.*, 2006; Jiang *et al.*, 2007a; Abanin *et al.*, 2007b; Giesbers *et al.*, 2009). Higher LL splitting at the $\nu = 4$ state has been found to be exchange-enhanced spin split, since the energy gap is much larger than bare Zeeman energy, and the gap increases as Zeeman energy grows (Zhang *et al.*, 2006).

As for the ordering of the split zero LL, it cannot be simply analogous to the higher LLs, because of the $n = 0$ LL particle-hole symmetry. For the $\nu = 1$ state, a square root B dependence was found and the energy gap was not sensitive to in-plane magnetic field, indicating a valley splitting origin (Jiang *et al.*, 2007a). The experimental observations for $\nu = 0$ is to some extent controversial. The initial study of this state showed a plateau at zero for the Hall conductivity while the longitudinal resistivity exhibited a peak value at a few multiples of $\frac{h}{e^2}$. This has been explained by the exchanging roles of bulk and edge transport (Abanin *et al.*, 2007b,a). However, subsequent experiments on high mobility graphene devices revealed an insulating longitudinal resistance at $\nu = 0$ (Checkelsky *et al.*, 2008, 2009; Bolotin *et al.*, 2009). Although these observations on $\nu = 0$ and 1 have evoked many theoretical studies to explore the ordering sequence of the degeneracy breaking (Abanin *et al.*, 2007b;

Shimshoni *et al.*, 2009; Jung and MacDonald, 2009; Herbut, 2007; Fuchs and Lederer, 2007; Hou *et al.*, 2010; Nomura *et al.*, 2009; Kharitonov, 2011), the discrepancies among experiment and theory have not yet been conclusively resolved. We will present our study in this direction in Chap. 4.

Furthermore, at even higher field with sufficient electron-electron interactions, fractional QHE under this new SU(4) symmetry has been predicted by many theoretical papers (Töke *et al.*, 2006; Töke and Jain, 2007; Goerbig and Regnault, 2007; Shibata and Nomura, 2009; Khveshchenko, 2007; Apalkov and Chakraborty, 2006). FQHE has been observed experimentally in suspended graphene (Bolotin *et al.*, 2009; Du *et al.*, 2009; Ghahari *et al.*, 2011) and graphene on hexagonal boron nitride (Dean *et al.*, 2011). Studies on these strongly correlated regimes are exciting and will provide an alternative insight to the nature of the LL broken symmetry.

1.3 Bilayer graphene

1.3.1 Lattice structure and electronic band structure

Solving the energy spectrum in bilayer graphene is slightly more complicated compared with monolayer graphene due to the Bernal stacking of the two graphene layers. Fig. 1.6(a) shows the bilayer graphene lattice structure, where the bottom layer A_2 atom sits right under the top layer B_1 atom. Apart from the nearest neighbor hopping mechanism ($\gamma_0 = t$) in monolayer graphene, a substantial hopping between A_2 and B_1 atoms are expected as a result of the overlapping of the out-of-plane π orbitals, denoted by the hopping integral γ_1. Weaker hoppings can also occur between orbitals further apart as indicated in Fig. 1.6(a) (labeled as γ_3, γ_4). Following the conventional notation in graphite, we denote the corresponding hopping integrals

$\gamma_1 = 0.4$ eV, $\gamma_3 = 0.3$ eV, $\gamma_4 = 0.04$ eV (Brandt and Ponomarev, 1988; Dresselhaus and Dresselhaus, 2002).

Within the simplest model, the Hamiltonian is written similarly to the monolayer one with an extra term from the interlayer hopping:

$$\mathbf{H}_{BG}^{TB} = -t\sum_{i,j,\sigma}[(\mathbf{a}_{1,i\sigma}^{\dagger}\mathbf{b}_{1,j\sigma}+\mathbf{H}.c.)+(\mathbf{a}_{2,i\sigma}^{\dagger}\mathbf{b}_{2,j\sigma}+\mathbf{H}.c.)]-\gamma_1\sum_{i,\sigma}(\mathbf{a}_{2,i\sigma}^{\dagger}\mathbf{b}_{1,j\sigma}+\mathbf{H}.c.)) \quad (1.24)$$

Since A_1 and B_2 overlap with each other in the x-y plane, the last term in the Hamiltonian does not contain any k-dependence. Adopting the result from the monolayer calculation, we then write the bilayer Hamiltonian in a 4-dimensional spinor notation as following:

$$\psi_k = (\psi_{A_1}, \psi_{B_1}, \psi_{A_2}, \psi_{B_2})^T$$

$$\mathbf{H}_k = \begin{pmatrix} 0 & v_f(\mathbf{q}_x + i\mathbf{q}_y) & 0 & 0 \\ v_f(\mathbf{q}_x - i\mathbf{q}_y) & 0 & \gamma_1 & 0 \\ 0 & \gamma_1 & 0 & v_f(\mathbf{q}_x + i\mathbf{q}_y) \\ 0 & 0 & v_f(\mathbf{q}_x - i\mathbf{q}_y) & 0 \end{pmatrix} \quad (1.25)$$

The effective Hamiltonian in the $A_1 - B_2$ subspace is then:

$$\mathbf{H}_{A_1-B_2} = \frac{v_f^2}{\gamma_1}\begin{pmatrix} 0 & (\mathbf{q}_x + i\mathbf{q}_y)^2 \\ (\mathbf{q}_x - i\mathbf{q}_y)^2 & 0 \end{pmatrix} \quad (1.26)$$

The energy spectrum is given by:

$$E^2 = v_f^2\hbar^2q^2 + \frac{\gamma_1^2}{2}\left(1 \pm \sqrt{1 + 4v_f^2\hbar^2q^2/\gamma_1^2}\right). \quad (1.27)$$

This equation represents four bands, as shown in Fig. 1.6, with two bands degenerate at the Dirac points and two split bands. At low energy, near the Dirac points, the energy dispersion is simplified to the following form:

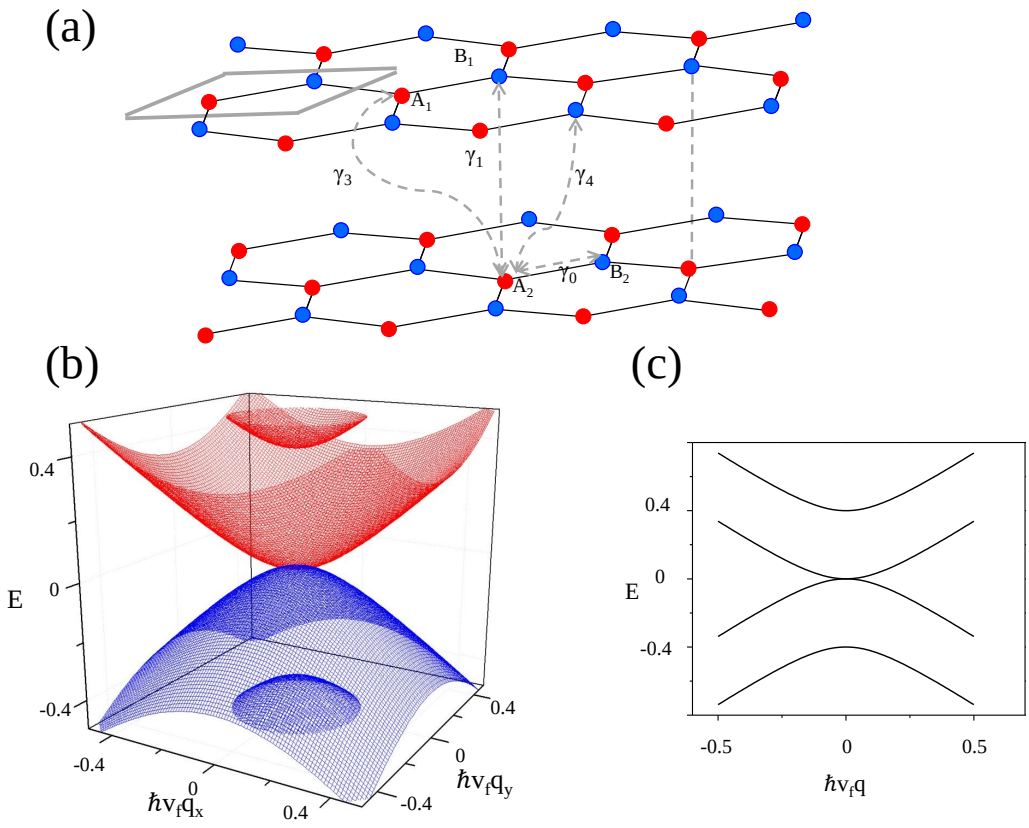

Figure 1.6: (a) Bilayer graphene lattice structure in a Bernel Stacking, γ_i is the hopping integrals of the indicated pairs; (b) Energy spectrum at low energy showing four bands, two of which touch at **K** or **K'** points and two of which are split; electron and hole symmetry is preserved; (c) Parabolic band structure at low energy.

$$(2E \pm \gamma_1)^2 - 4v_f^2\hbar^2q^2 = \gamma_1^2 \tag{1.28}$$

where we see a parabolic band behavior near $E = 0$. Comparing with the carrier characteristics in monolayer graphene, the parabolic band structure near the Dirac points indicates the carriers are massive Dirac fermions with an effective mass $m^* =$

$\frac{2\gamma_1\hbar^2}{3ta^2} = \frac{\gamma_1}{2v_f^2}$.

Note that we start with a clean bilayer system with no potential bias between the top and bottom layer. Any potential bias will result in corresponding potential components in the initial Hamiltonian in Eq. 1.25. Thus a band gap will be introduced:

$$E^2 = E_0^2 + v_f^2\hbar^2q^2 - \frac{\gamma_1}{2}\left(1 \pm \sqrt{1 + 4v_f^2\hbar^2q^2/\gamma_1^2}\right) \tag{1.29}$$

where E_0 is the potential bias between the two layers.

Comparing the Hamiltonian of bilayer graphene (Eq. 1.26) with that of monolayer graphene(Eq. 1.19), the charge carriers in bilayer have a Berry phase 2π, in contrast to quasiparticles with a Berry phase of π in monolayer graphene.

1.3.2 Quantum Hall effect in bilayer graphene

In this subsection, we discuss the quantum Hall effect in bilayer graphene. Similar to monolayer graphene, we again begin with the simplest model presented in the previous section, and perform the substitution $\mathbf{p} \to \mathbf{p} - e\mathbf{A} \equiv \boldsymbol{\pi}$. The Hamiltonian near the Dirac point is then:

$$\mathbf{H} = \frac{v_f^2}{\gamma_1}\begin{pmatrix} 0 & (\boldsymbol{\pi}_x + i\boldsymbol{\pi}_y)^2 \\ (\boldsymbol{\pi}_x - i\boldsymbol{\pi}_y)^2 & 0 \end{pmatrix} \tag{1.30}$$

Introducing $\boldsymbol{\Pi}_i = l_B\boldsymbol{\pi}_i/\hbar$ and taking the square of the Hamiltonian as in the previous case:

$$\mathbf{H}^2 = \frac{\hbar^2v_f^2}{\gamma_1 l_B^2}\begin{pmatrix} (\boldsymbol{\Pi}_x^2 + \boldsymbol{\Pi}_y^2 + 1)(\boldsymbol{\Pi}_x^2 + \boldsymbol{\Pi}_y^2 + 3) & 0 \\ 0 & (\boldsymbol{\Pi}_x^2 + \boldsymbol{\Pi}_y^2 - 1)(\boldsymbol{\Pi}_x^2 + \boldsymbol{\Pi}_y^2 - 3) \end{pmatrix} \tag{1.31}$$

The eigenvalue of the above Hamiltonian is given by

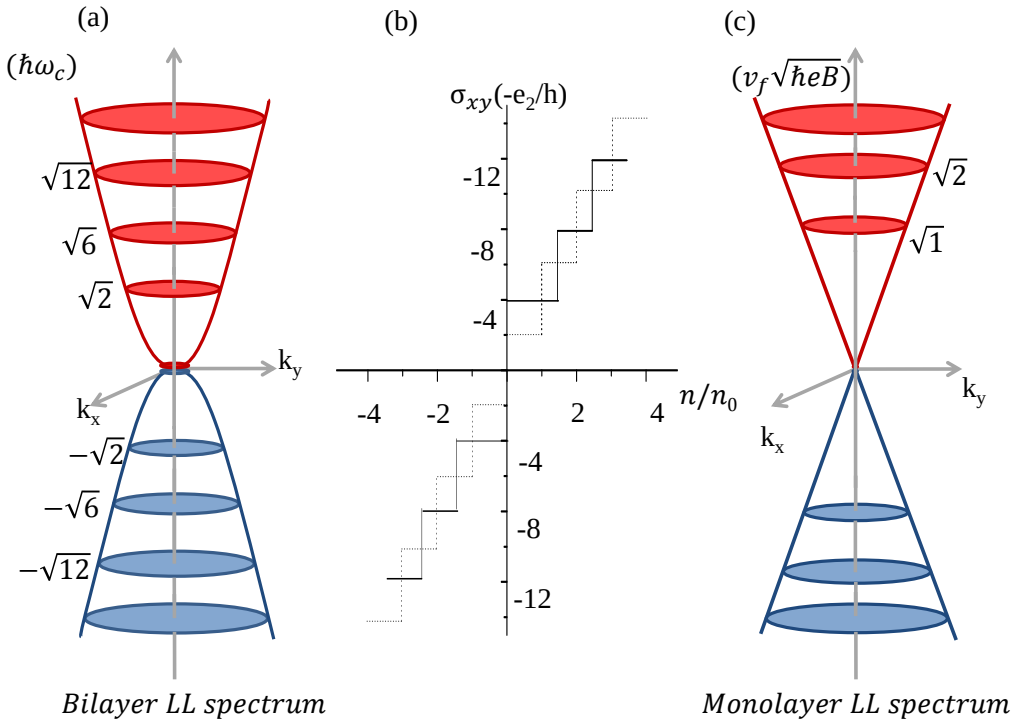

Figure 1.7: (a) Landau levels for graphene bilayer at low energy ($E < \gamma_1$); (b) Schematics of the Hall conductivity σ_{xy} as a function of n/n_0, with $n_0 = \frac{4}{2\pi l_B^2}$ for bilayer graphene (solid line), and monolayer graphene (dotted line); (c) LLs for monolayer graphene as a reference.

$$\mathbf{H}^2\Psi = \frac{4\hbar^2 v_f^2}{\gamma_1 l_B^2}\begin{pmatrix}(n+1)(n+2)\\ n(n-1)\end{pmatrix}\Psi, \quad n = 0, 1, 2, ... \tag{1.32}$$

Thus the LLs for bilayer graphene are

$$E_n^{\pm} = \pm\hbar\omega_c\sqrt{|n|(|n|-1)}, \quad \omega_c = \frac{eB}{m^*}, \quad m^* = \frac{\gamma_1}{2v_f^2} \approx 0.03m_e \tag{1.33}$$

E_n^+ and E_n^- are assigned to electron and hole states respectively. Similar to monolayer graphene, each none-zero LL contains four degenerate states, caused by the spin

and pseudospin degeneracy, while for $E = 0$ state, the degeneracy doubles because of the orbital degeneracy $n = 0$, or 1. Hence the zero energy LL contains a eight-fold degeneracy. Consequently the quantum Hall plateaus are expected to be at filling factors $\nu = 4n$, where n is a non-zero integer. The degenerate LL formation under magnetic field was predicted theoretically (McCann and Falko, 2006), and observed experimentally by Novoselov *et al.* (2006).

Note that although γ_3 will change the energy spectrum qualitatively at low energies by introducing a trigonal warping on the bands near the Dirac points (this breaks the iso-energy lines into four pockets), the effect is believed to be insufficient to affect the LL spectrum over the magnetic field range studied in this work (McCann and Falko, 2006), and the eight-fold degeneracy at zero energy LL is preserved. In order to understand the nature of the electron-hole degenerate zero energy LL, we shall investigate the degeneracy lifting at zero energy state in Chap. 3.

Chapter 2

Sample preparation

In this chapter, we describe the sample fabrication methods used in this work. We first describe the general device fabrication process of mechanically exfoliating graphene, then introduce the thermal annealing procedure for cleaning the sample surface. We also present progress on preparing high quality multi-probe suspended graphene devices.

2.1 General device procedures

2.1.1 Device fabrication

For the time being, mechanical exfoliation from bulk crystal graphite remains the preferred method for obtaining graphene for most of the experimental research community around the world, since it produces the most reliable quality graphene flakes and the subsequent lithographic process is straightforward. All graphene samples employed throughout this work are produced based on the mechanical exfoliation method invented by the Manchester group (Novoselov *et al.*, 2004).

We use a doped-Si/SiO_2 wafer as a supporting substrate for graphene pieces. The sandwich structure of SiO_2 dielectric layer in between doped Si and graphene forms a capacitor, which allows the charge carrier density in graphene to be tuned. By

folding the scotch tape with a ∼mm size bulk graphite crystal several times, we pre-cleave and spread thin graphite crystal over the surface of the tape. Then we press and rub the spread-out thin crystals onto the wafer substrate gently. When the tape with graphite crystals is pulled away, van der Waals force competition separation occurs between different interfaces: the graphite/substrate interface and graphene layer interface in the bulk graphite. The relative weakness of the latter results in thin graphene layers (from monolayer to a few layers) or bulk graphite attaching to the SiO_2 substrate. In fact comparison of the work of adhesion between different interfaces shows that thin layers are energetically favorable (Li *et al.*, 2009). The main difficulty in using exfoliation is locating the graphene flakes. The optical contrast of monolayer graphene on a Si/SiO_2 wafer changes with the thickness of SiO_2 (d_{SiO_2}); maximal contrast appears at $d_{SiO_2} = 90$ nm and 300 nm for monochromatic light with a wavelength of 550 nm, the wavelength to which human eyes are the most sensitive (Novoselov *et al.*, 2004; Blake *et al.*, 2007). We choose the thickness of the thermally grown SiO_2 to be 285 nm (±7 %), in order to optimize both the optical contrast and the tunable range of the charge carrier density, which is limited by the dielectric capacitance through ϵ/d and the breakdown voltage, where $\epsilon = 4$ is the dielectric constant of SiO_2.

We use 3M Scotch tap and Kish graphite from Toshiba Ceramics. Prior to the exfoliation, the wafer chips are immersed in Pirahna (3:1 $H_2SO_4 : H_2O_2$ solution) for 15 mins, rinsed by DI water, and blown dry with nitrogen gas. We usually bake the substrate on a hotplate at 120°C for 10 mins right before the exfoliation to get rid of accumulated moisture, a source of impurities trapped between graphene and the substrate. The exfoliation procedure itself can hardly be standardized. However a general guideline is the following: we would like to maximize the area of spread-out graphite to increase the chance of finding graphene pieces within a finite substrate area; we would like to minimize the graphite thickness by folding scotch tape re-

peatedly, while avoiding polluting the graphite with tape residue. Based on these guidelines, we usually start with a millimeter-size graphite crystal, pre-peel it with scotch tape and select a thin layer from the page-like bulk crystal with a sharp tip tweezer. This fresh piece of graphite is delivered to a new piece of tape and spread out by folding it 4-6 times. We then gently rub a pre-selected area of the tape on the pre-treated wafer using the flat end of a teflon tweezer. It usually takes about two minutes to remove the tape covering a 1cm×1cm chip. A typical result of the mechanical exfoliation is shown in Fig. 2.1(a) and (b).

A standard device with metal contacts is made using a conventional electron beam (e-beam) lithography process followed by a metal deposition with Cr/Au (1/40 nm). We usually try to use isolated graphene pieces with natural edges, but in certain cases an additional patterning (such as Hall bars, etc.) is required to fit the specific experimental needs. One can pattern an etch mask with an additional e-beam lithography process to protect the desired area of graphene, and then perform an oxygen plasma etch to remove the unwanted area. If the pattern is large enough (≥500 nm), one can use the same lithography resist (PMMA). For graphene nanoribbons, a different e-beam resist of HSQ is used, in order to achieve finer structures (Han *et al.*, 2007). For plasma etching we use a Technics Reactive Ion Etcher (RIE) with 250 mTorr oxygen pressure, 50 W power, and an etch rate of about one layer per second with a $\sim$ 5 s initial delay. Fig. 2.1(c) shows a 100X optical image of an etched device (a MG/BG junction device, for the study described in Chap. 5).

Starting from the back gated device, we can make dual gated devices by depositing another layer of gate dielectric with metal contact on the top. The top gate can be any kind of dielectric materials, such as thermally grown SiO_2, atomic layer deposition (ALD) grown HfO_2, or even solid polymer electrolyte (Efetov and Kim, 2010). Fig. 2.1(d) shows a finished dual gated device made by depositing 25 nm ALD HfO_2 as dielectric layer. Note that a thin wetting layer is required to grow HfO_2

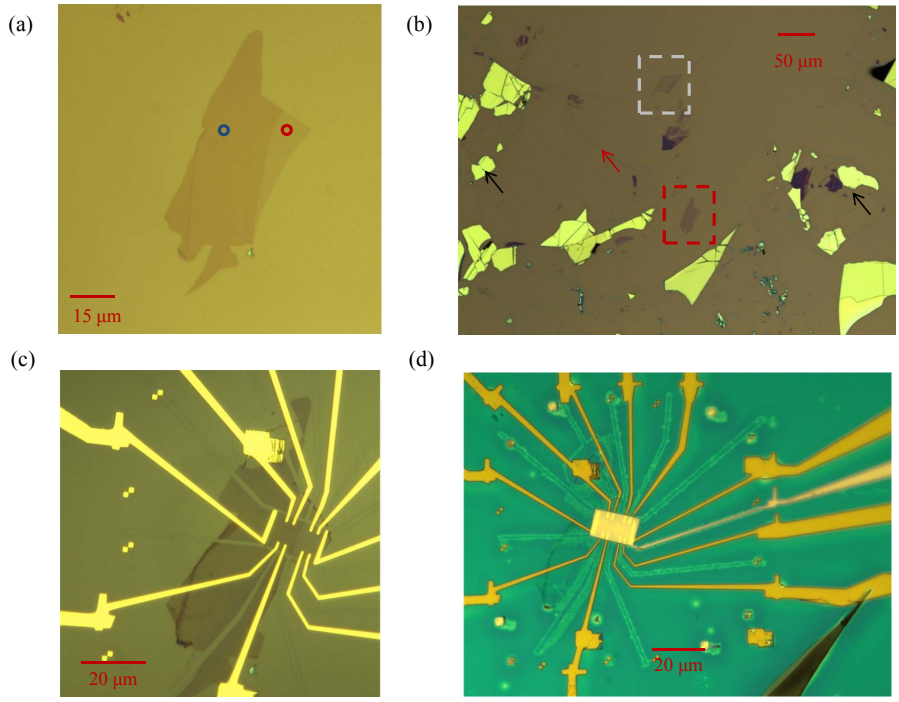

Figure 2.1: Optical Microscop images from a typical mechanical exfoliation. (a) 50X optical image from a zoom-in of the red dashed square region in (b); monolayer, bilayer areas are marked by red and blue circles, respectively. (b) 20X optical image; black arrows indicate the bulk graphite flakes, while the red arrow points out the tape residue from the exfoliation process; The grey dashed square marks another monolayer graphene piece at the same spot. (c) 100X optical image of a device etched by oxygen plasma; (d) 50X optical image of the same device with a top gate; dielectric layer is ∼10 nm HSQ and 25 nm HfO_2.

uniformly above graphene (Meric *et al.*, 2008), so the actual dielectric constant is given by ∼10 nm HSQ and 25 nm HfO_2.

2.1.2 Device characterization (AFM, Raman, and zero magnetic field transport)

Once contacts have been patterned, one can certainly identify monolayer graphene or bilayer graphene by their unique QHE. However, before we expend efforts in the lithography processes, additional methods to identify thin flakes, besides the subjective judgment from optical contrast, are necessary. Fig. 2.2(b) shows a typical non-contact mode AFM image of a graphene piece. Monolayer graphene on oxidized wafers has a height of 0.8 to 1.2 nm, a discrepancy from the expected thickness which may be a result from the ambient environment. Any additional layer will add the expected 0.35 nm thickness, which corresponds to the van der Waals interlayer distance in graphite. In addition to the issue of the height discrepancy, since AFM is slow and limited by the scan size, it is usually used primarily as a method to monitor the topographical surface quality rather than to identify the number of layers.

Raman spectroscopy can reflect the changes in the electronic band structure for monolayer, bilayer and few-layers graphene (Ferrari *et al.*, 2006). The Raman spectrum contains three peaks: a G peak at ∼1560 cm^{-1}, a D peak at ∼1360 cm^{-1}, and a signature 2D peak at ∼2700 cm^{-1}. The G peak is a result of the E_{2g} phonon at the centre of the Brillouin zone, while the D peak is due to the out-of-plane mode of the sp^2 carbons and probes the defect and impurity density in graphene. Fig. 2.2(a) shows the Raman spectrum of the device in Fig. 2.1. As shown in the inset, the shape of the 2D peak for monolayer graphene can be fit by a symmetric Lorentzian function, while that of bilayer shows a small shoulder on the left side of a flattened peak, a feature from which the number of layers can be determined. The Raman

spectrum for thicker layers ($>$ 5 layers) can hardly be distinguishable. The Raman data is taken using a Reinshaw InVia Raman microscope, $\lambda = 488$ nm laser, with a 10 s integration time.

Fig. 2.2 shows a typical four-terminal longitudinal resistivity measurement of a few monolayer graphene devices using a standard current bias ($I = 100$ nA) lock-in technique. The gate voltage at which a peak occurs is defined as V_D; this peak point is also called the charge neutrality point (CNP). V_D is typically a non-zero value (occasionally negative), indicating an unintentional initial doping from charge impurities (density of charged impurity is denoted by n_i). As the gate voltage approaches V_D, carrier density in the device ($n = C_g(V_g - V_D)/e$) becomes smaller than the fluctuations in carrier density induced by the charge impurities. Therefore at the CNP, there are puddles of electrons and holes on the graphene surface. The resistance at the CNP has a finite value due to the existence of a finite density of states. The charge impurities could be from the SiO_2 substrate, or impurities on graphene surface (due to lithography residues or impurities trapped in between graphene and the substrate), etc.. Statistically, for a sufficiently large graphene piece (length$\geq$2 μm), the trapped charge contribution from SiO_2 substrate is more or less neutral, since the potential variation contribution from the substrate averages to zero (Martin *et al.*, 2008).

In addition to charged impurities, neutral impurities (e.g. point defects in the lattice structure), with density denoted by n_p, can produce short range potentials and thus act as a source of scattering. The scattering time of carriers estimated from short range scatters is $\tau_s \propto 1/(n_p\sqrt{n})$, while that estimated from screened charge impurity scatters (through long range Coulomb potential) is $\tau_c \propto \sqrt{n}/n_i$ (Nomura and MacDonald, 2007). Using Boltzmann transport theory, the conductivity is given by

$$\sigma = \frac{e^2}{h}\frac{2E_f\tau}{\hbar} \tag{2.1}$$

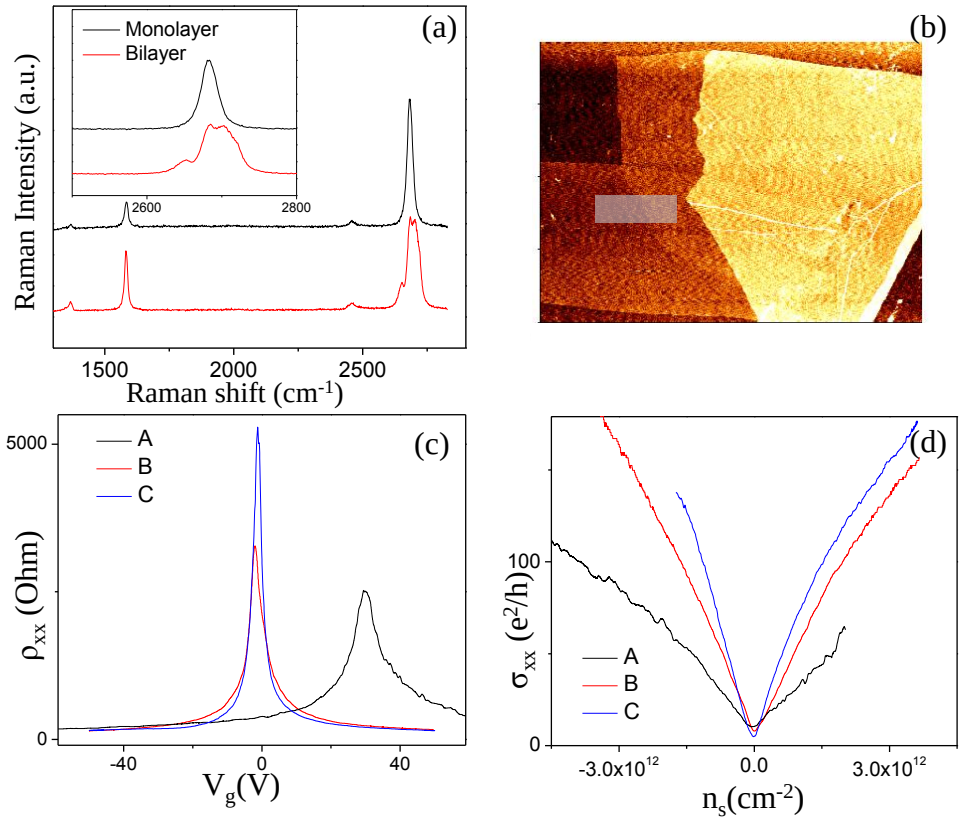

Figure 2.2: (a) Raman spectrum of monolayer graphene (black) and bilayer graphene (red); inset: a zoom-in of the 2D peak, from which the number of layers is identified; (b) Non-contact mode AFM image of a fresh graphene piece right after exfoliation, the rms surface roughness is 0.3 nm; the step height between monolayer and bilayer is 0.4 nm, while the step height between SiO_2 and monolayer graphene is 1.1 nm; (c) Gate sweep of the longitudinal resistivity for a few monolayer device with different mobility at $T = 1.7$ K. The field effect mobilities of sample A to C at hole density $n = 4 \times 10^{12}$ cm^{-2} are 4,000, 10,000, 12,000 cm^2/Vs, respectively; (d) Conductivity vs. carrier density, calculated from monolayer data in (c), showing a linear dependence far away from V_D, and a sublinear dependence near V_D.

where τ is the scattering time. In the presence of both scattering mechanisms, τ is then determined by $1/\tau = 1/\tau_c + 1/\tau_s$. Therefore, at high carrier density (V_g away from V_D), the conductivity is linear in carrier density: $\sigma \propto n/n_i$, and the linear dependence on carrier density may become sublinear as the CNP is approached. Fig. 2.2(d) shows conductivity vs. carrier density of a few graphene devices with different mobility, calculated from Fig. 2.2(c), with the sublinear change more pronounced in high mobility samples (i.e. n_i/n_p is small).

One can estimate graphene sample quality by the above gate sweep curves, through the sample mobility $\mu = \frac{1}{ne\rho}$, as well as the magnitude and sharpness of the Dirac peak. At high carrier density, the mobility calculated from the field effect carrier density $n = C(V_g - V_D)/e$ is similar to that calculated from the classical Hall effect, $n = \frac{IdB}{edV_H}$.

2.2 Effect of thermal annealing

After metal contact deposition, the rms surface roughness of graphene usually increases to about 1.2 nm, compared with the typical 0.3 nm right after mechanical exfoliation, indicating lithography residue accumulates on the sample surface, as shown on the top panel of Fig. 2.3(b). Since the e-beam resist (PMMA) has a boiling point of 200° and all the solvents used in processing (MIBK, IPA, Acetone) have an even lower boiling point, one possible way of removing these residues is by thermal annealing (Ishigami *et al.*, 2007). In this method, the device is annealed at 300°C for 1 hour with a mixture of argon and hydrogen gas (3:1) (denoted as process 1). Argon flow (3 scfh) is maintained throughout the heating and cooling procedure, while hydrogen flow is shut off during cooling. The annealing effect on the sample surface is consistent and it is shown in bottom panel of Fig. 2.3(b) (data taken in a nitrogen ambiance). The surface residues are thoroughly removed after annealing, and the

rms surface roughness for graphene and SiO_2 is reduced to 0.16 nm and 0.176 nm, respectively.

In Fig. 2.3(c), we measures the resistance as a function of gate sweep continuously in air right after the above thermal annealing. Note that this is a different device from the one studied in Fig. 2.3(a) and (b). V_D quickly shifts towards the positive side and moves out of our gate sweep window. We attribute this heavily p-doped phenomenon in air to molecular adsorption of moisture and oxygen, since the CNP can be restored to a finite value (usually 10∼40 V) by putting it in a nitrogen ambiance (denoted as process 2). A vacuum annealing (400 K, 10^{-5}Torr for 1 hour) may further reduce V_D (Fig. 2.3(d))(denoted as process 3). Among six devices with the same Ar/H_2 annealing and subsequent vacuum annealing, four of them show $|V_D| \leq 10$ V, and the other two exhibit a random V_D between 10 V and 40 V. Further analysis of the field effect mobility comparison is presented for five of the six devices in Fig. 2.3(e), where y-axis is field effect mobility at hole density $n = 1.4 \times 10^{12}$ cm^{-2}, and 1, 2, 3 on the x-axis indicate the different processes (the last device did not show any Dirac peak before annealing). We do not notice any systematic improvement or degradation of sample mobility, which is consistent with the speculation in Morozov *et al.* (2008) and Chen *et al.* (2008), that charge impurities on the SiO_2 substrate are the dominant scattering mechanism.

To conclude, thermal annealing and vacuum annealing clean the resist-contaminated graphene surface and shift V_D effectively. Alternatively, a wet-chemical treatment using chloroform is reported to achieve similar effects on cleaning the surface (Cheng *et al.*, 2011). However, this process does not improve sample mobility, which is an important indicator of sample quality. Experiments on suspended graphene (Bolotin *et al.*, 2008, 2009; Ghahari *et al.*, 2011; Du *et al.*, 2009) and graphene on hexagonal boron nitride substrates (Dean *et al.*, 2010) have shown significant improvement of graphene quality after removing the substrate induced ripples and charge traps.

t

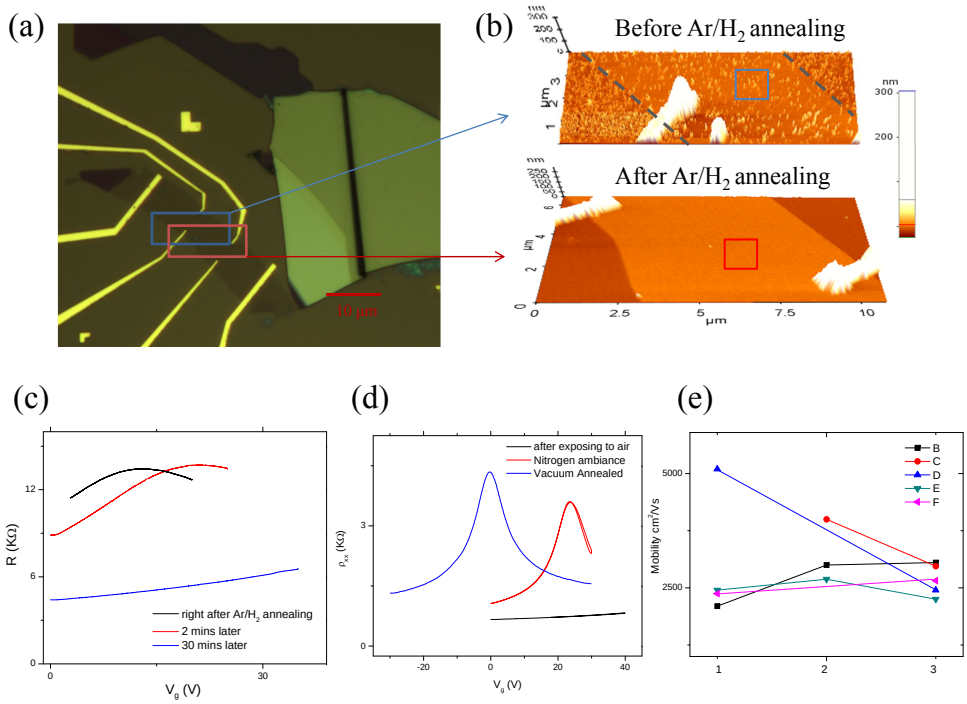

Figure 2.3: (a) Optical microscope image of the device studied in Fig. 2.3(b); (b) top: before Ar/H_2 annealing, AFM image of the blue square area in (a); bottom: After Ar/H_2 annealing, AFM image of the red square area as shown in (a); The rms (R_q) surface roughness of graphene decreases from 1.2 nm (blue square) to 0.16 nm(red square); (c) After Ar/H_2 annealing the sample is exposed to air. Resistance is measured in a two-probe geometry vs. back gate voltage for different exposure times; (d)The resistivity of a different device as a function of back gate voltage showing the restored CNP under a nitrogen environment (red) and an almost zero CNP after vacuum annealing; (e) Mobility at a fixed hole density $n = 1.4 \times 10^{12}$ cm^{-2} after processes 1, 2, 3 for five different samples (B - F).

We will discuss our method of fabricating high mobility multi-terminal suspended graphene in the next section.

2.3 Suspended multi-terminal devices

Although multi-terminal measurements were reported in suspended samples, those experiments fails to detect FQHE or even IQHE in devices with a Hall bar geometry (Bolotin *et al.*, 2008; Du *et al.*, 2009). Possible reasons for such failure could be thermal instability (Skachko *et al.*, 2010) or elastic strain concentrated at the sample edges/corners (Fogler *et al.*, 2010; Prada *et al.*, 2010). We are interested in investigating the symmetry breaking nature near the charge neutrality point, and the newly discovered strongly-correlated states. Using suspended multi-terminal devices to obtain high mobility samples is one possible method of investigating these phenomena. Here we follow the method described in Bolotin *et al.* (2008). By choosing a naturally exfoliated graphene strip of an appropriate size and a careful strategy of current-annealing, we show that the IQHE and FQHE can be measured in multi-terminal suspended graphene devices. Detailed study of the $\nu = 1/3$ gap using such a multi-terminal suspended device has been published as Ghahari *et al.* (2011). In this subsection we emphasize that the fabrication and current annealing processes are capable of producing high quality suspended devices with which QH physics can be further explored.

A straightforward method of making a suspended graphene device is to deposit graphene pieces on a pre-etched trench. For multi-terminal devices, this method is extremely low-yield because it requires graphene exfoliation on a specific location. An alternative approach is to use reactive ion etching (RIE) with CF_4 to remove the underneath substrate after metal contact deposition, or to perform wet etching with HF (buffered oxide etchant is often used to have better control over the etch rate). In

this work, a wet etching method is preferred to avoid possible metal contamination when using RIE.

Our devices are pre-patterned to an approximately 1 $\mu m \times 1$ μm Hall bar with four probes. Cr/Au (1 nm/75 nm) electrodes are deposited by metal evaporation followed by a hot acetone (70 °C) liftoff. Electrode width is designed to be more than 500 nm (1 μm is desirable) to enhance the mechanical stability of the device. The device is then immersed into a 5:1 BOE (NH_4F:HF = 5:1) for 12 mins. About 200 nm of SiO_2 is etched away uniformly except those areas covered by metal contacts. The etching underneath graphene is facilitated by the moisture trapped in between the graphene and SiO_2 substrate. In order to remove residues from the chemical reaction, the device is then transferred into a series of water/Acetone mixtures with successively decreasing ratios in order to reduce the chance of collapsing the device due to surface tension mismatch. Instead of using a critical-point-dryer, we carefully blow dry the device after another round of Acetone/IPA mixture cleansing (again with a decreasing ratio of IPA). Although using a critical point dryer makes suspension of larger area devices easier, we try to avoid it since the contamination from our critical-point-dryer system is hard to remove in the current-annealing procedure described below.

Fig. 2.4(a) presents the AFM image of two types of multi-terminal devices after successful suspension. The right device is fabricated from a natural graphene stripe with invasive Hall probes on the side, while the left one is from a pre-etched graphene piece with a Hall bar geometry. We then perform DC current annealing in a helium environment at a pressure of 1∼4 Torr. By applying a DC voltage (V_{sd}) across the source and drain electrodes, we heat the suspended graphene piece locally (Berciaud *et al.*, 2010), with the only effective thermal conduction path out of the graphene being the metal contacts. As the heating power increases with increasing V_{sd}, impurities (mostly lithography residue) are more efficiently burned away, but there is higher chance of losing the contacts and destroying graphene channel itself. For two-probe

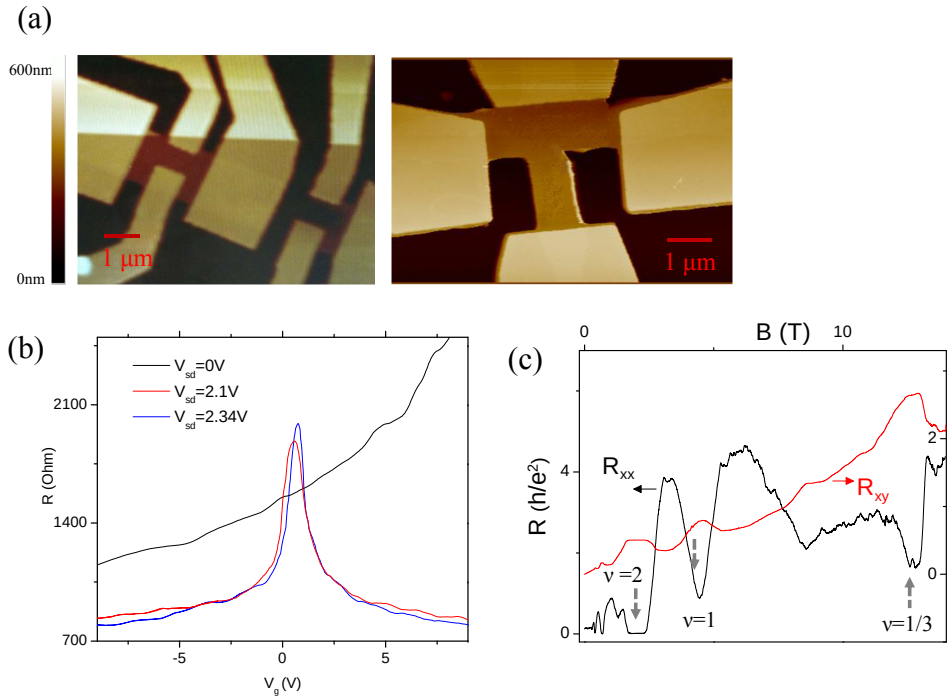

Figure 2.4: (a) AFM images of two types of multi-terminal suspended devices: a natural graphene stripe with invasive Hall probes (left), and pre-etched graphene with a Hall bar geometry (right); (b) Two-probe resistance as a function of back gate voltage (kept at $V_g \leq 10$ V to avoid collapse) under different heating powers, denoted by different values of V_{sd}; (c) Longitudinal resistance (black) and Hall resistance (red) (from van der Pauw measurements) vs. magnetic field for an optimally annealed device. All transport data are taken at $T = 1.7$ K.

suspended devices, we increase the DC bias in small steps (0.2 V) and at the same time monitor the Dirac peak change. The general trend of an effective current annealing is shown in Fig. 2.4(b): V_D approaches zero at first and the broad Dirac peak gets narrower during further annealing. As stated in Sec. 2.1.2, we can estimate the quality from the sharpness of Dirac peak. Usually a typical suspended graphene flake with $\mu \geq 20,000$ cm^2/Vs has a full width at half maximum around 1.5 V.

From the current annealing process, we have learned that the pre-etched Hall bar geometry is undesirable. Sturdy PMMA residues that result from the e-beam patterning are found to be concentrated along the etched edges of graphene, which would require additional heating power to remove those impurities. Instead, we select natural graphene strips with 1∼2 μm width and 2∼4 μm length, to balance the heating efficiency and the possibility of electrode/graphene damage. Uniformity of annealing is also a key point. For example, for the device in the left of Fig. 2.4(a), we found the following annealing procedure the most effective: applying DC voltage alternately across the two current contacts and between the Hall voltage probes with an annealing strength proportional to their contact area. After completion of this optimal annealing procedure, we obtain a clear signature of the QHE with R_{xx} minima and R_{xy} plateaus at integer filling and fractional filling factors $\nu = 1/3, 1, 2, ...$, as shown in Fig. 2.4(c).

The $\nu = 0$ QH state of this particular device was also studied. Results are presented in Chap. 4.

Chapter 3

Symmetry breaking of the zero energy Landau level in bilayer graphene

In this chapter, we report magneto-transport measurements on graphene bilayer where the eight-fold symmetry-breaking of the zero energy LL is observed. Under high magnetic field (up to 35 T), the zero energy quantum hall octet splits completely into eight separate LLs and new QH states of $\nu = 0, 1, 2, 3$ are observed. The activation energy measurements of these QH states demonstrate that energy spacing is smaller than the bare electron-electron (e-e) interaction energy and Zeeman energy. We find that the activation of the excitations at $\nu = 1, 2, 3$ in tilted magnetic fields are independent of spin, which is consistent with the formation of quantum Hall ferromagnet at $\nu = 0$. We also observe a diverging resistance as a function of magnetic field at the charge neutrality point $\nu = 0$. The results presented in this chapter is published as Zhao *et al.* (2010).

3.1 Introduction

As we discussed in the introduction chapter, both monolayer graphene and bilayer graphene are found to have a novel half-integer QHE due to the unique chiral nature of the carrier dynamics (Novoselov *et al.*, 2005a; Zhang *et al.*, 2005; Novoselov *et al.*,

2006), which distinguishes them from the conventional 2DEG systems. The unique low energy dispersion relations: linear in monolayer graphene (Eq. 1.10) while being parabolic in bilayer graphene (Eq. 1.27), lead to unevenly spaced Landau levels. In monolayer graphene, the spacing is linear to the square root of LL index n as shown in Eq. 1.22, and each LL has a four-fold degeneracy due to the valley and spin degrees of freedom. While in bilayer graphene, the coupling between the top and bottom layers pushes the corresponding LL to higher energy, which is linear to $\sqrt{n(n-1)}$ as shown in Eq. 1.33. The "layer" degeneracy is the same as "valley" degeneracy for bilayer. However, there is an additional orbital degeneracy for $n = 0$ and 1 indices, which results in eight-fold degenerate zero energy LL that is unprecedented in LL physics (McCann and Falko, 2006; Novoselov *et al.*, 2006; Barlas *et al.*, 2008).

At high magnetic fields, the decreasing radius of the cyclotron orbits gives rise to increasing electron-electron interactions which can perturb the degenerate LLs. This effect could be most pronounced at lower filling fractions where the exchange interactions are greater. Experiments in monolayer graphene have already demonstrated the broken symmetry states of $n = 0$ and 1 by the appearance of new QH states at the filling factor sequences $\nu = 0, \pm 1, \pm 4$ (Zhang *et al.*, 2006; Jiang *et al.*, 2007a; Giesbers *et al.*, 2009). In particular, it has been observed that in monolayer graphene the $\nu = 0$ QH state becomes increasingly insulating at higher magnetic fields (Checkelsky *et al.*, 2008, 2009; Du *et al.*, 2009; Bolotin *et al.*, 2009). The precise nature of the field-dependent mechanisms that lift the degeneracies in monolayer graphene is still under experimental and theoretical debates (Jiang *et al.*, 2007b; Yang, 2007; Kharitonov, 2011), which will be discussed in Chap. 4. Similar to monolayer, the enhanced interactions under high magnetic field is expected to lift the eight-fold degeneracy in the zero energy LL of bilayer graphene with the appearance of new QH plateaus. A number of theoretical predictions involving unusual collective excitations have been proposed to occur in this particle-hole symmetric LL as its degeneracy is

broken (Barlas *et al.*, 2008; Shizuya, 2009; Abanin *et al.*, 2009; Nandkishore and Levitov, 2010), but the observation was yet to be achieved. In the following section, we describe the first experimental observation of the magnetic field induced symmetry broken IQH states in bilayer graphene.

3.2 Broken symmetry at zero energy Landau level

To observe the new phases, we need the effect of e-e interaction to overcome that of the disorder. The combination of a high mobility device and a high magnetic field as shown in Fig. 3.1 can fulfill the goal.

Fig. 3.1(a) shows the field effect mobility as a function of carrier density for the bilayer graphene sample used in this work. This device has a mobility as high as $\sim 1.3 \times 10^4\,\mathrm{cm}^2/\mathrm{Vs}$ measured at the hole carrier density $n = 4 \times 10^{12}\,\mathrm{cm}^{-2}$. It is deposited on SiO_2 (300 nm)/Si substrates by mechanical exfoliation techniques from bulk single crystals (Novoselov *et al.*, 2005b) as described in Chap. 2. The number of graphene layers is identified by optical contrast. And it is also cross-checked using Raman spectroscopy (Ferrari *et al.*, 2006) and measurements of the high-field LL spectrum. Most of the experiments are performed in the 35 T magnet cell at the National High Magnetic Field Laboratory in Tallahassee, Florida, as shown in Fig. 3.1. Note that the mobility experiences a degradation to 1×10^4 $\mathrm{cm}^2/\mathrm{Vs}$ after transferring to the 35 T magnet cell.

A gate voltage V_g is applied to the degenerately doped Si substrate to control the carrier density n according to the relation $n = C_g(V_g - V_D)/e$, where the areal gate capacitance is $C_g = 7.1 \times 10^{10}\, e/\mathrm{V} \cdot \mathrm{cm}^{-2}$ and V_D is the gate voltage corresponding the charge neutrality point. The optical microscope image is shown in the lower inset of Fig. 3.2(a). Since the electrodes of this device are configured in non-ideal Hall bar geometry, the magnetoresistance R_{xx} and Hall resistance R_{xy} were obtained following

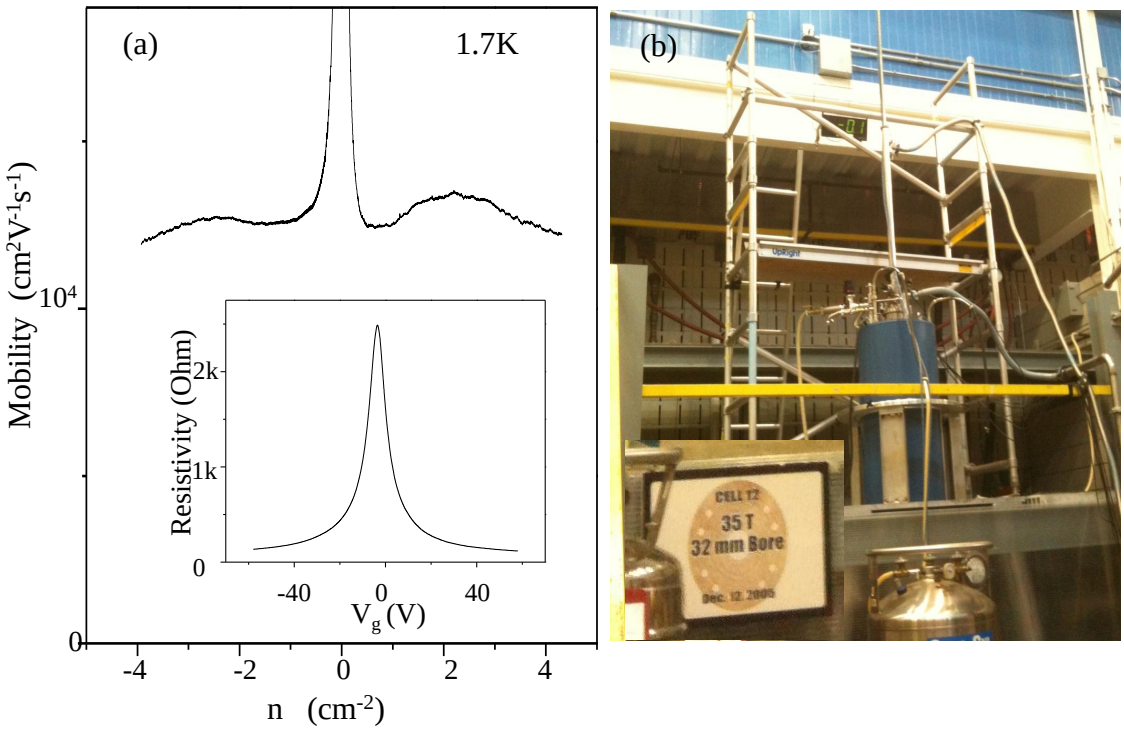

Figure 3.1: (a) Field effect mobility of a bilayer device(calculated from resistivity vs. back gate voltage as shown in the inset) as a function of charge carrier density n at T=1.7 K; (b) A photo of the 35 T magnet cell in National High Magnetic Field Laboratory in Tallahassee, Florida.

the van der Pauw method with symmetric (R_{xx}) and anti-symmetric (R_{xy}) averaging over data from positive and negative magnetic fields. The Hall conductivity σ_{xy} is then computed from R_{xx} and R_{xy} following the relation:

$$\sigma_{xy} = \frac{R_{xy}}{(R_{xx}w/l)^2 + R_{xy}^2}, \quad \sigma_{xx} = \frac{R_{xx}w/l}{(R_{xx}w/l)^2 + R_{xy}^2} \tag{3.1}$$

Fig. 3.2(a) shows and σ_{xy} as a function of V_g at a few different magnetic fields (B), as well as R_{xx} and R_{xy} in the upper inset. As the back gate voltage alters the carrier density, QH plateaus in R_{xy} with corresponding zeros in R_{xx} are observed. Consequently, the calculated σ_{xy} shows well quantized plateau values at $\frac{1}{\nu}\frac{h}{e^2}$ with the integer filling factor ν. In the low magnetic field regime ($B < 10$ T), QH states corresponding to $\nu = \pm 4,\ \pm 8$ are present, as were previously seen in Novoselov *et al.* (2006). As B increases, however, new QH states emerge, as evidenced by additional QH plateaus at $\nu = 0,\ 2$ and then $\nu = 1,\ 3$ at higher fields.

In the high magnetic field regime, $B \gtrsim 20$ T, the new set of QH states demonstrate the full eight-fold degeneracy lifting in the zero energy LL. Upon close inspection of σ_{xy} in different magnetic fields, we can construct the hierarchical evolution of these new QH states. As the field increases from the low magnetic field regime, the $\nu = 0$ and 2 states start to develop at 15 T and are fully evolved by 20 T; while the $\nu = 1$ and $\nu = 3$ states start to develop at 20 T and are fully evolved by 25 T. This hierarchical appearance of the new QH states is in accordance with the sequential symmetry breaking of the zero energy LL degeneracy as depicted in Fig. 3.2(b) and suggests that different symmetry-breaking process are relevant as B increases.

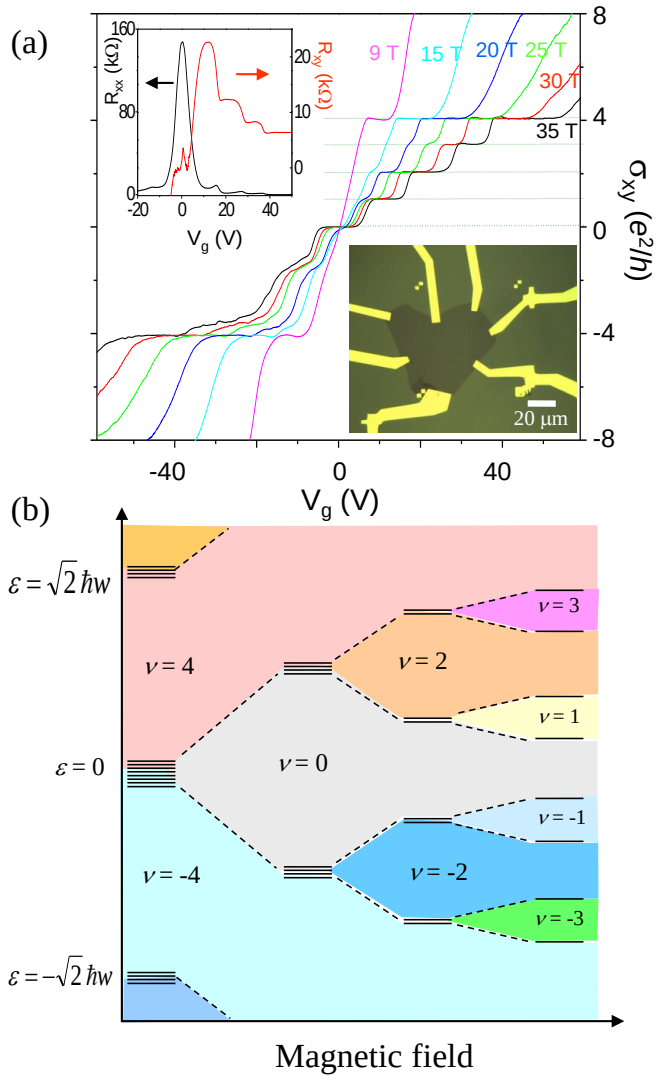

Figure 3.2: (a) Hall conductivity σ_{xy}, as a function of gate voltage V_g at T=1.4K at different magnetic fields: 9, 15, 20, 25, 30, and 35 T. Upper inset: R_{xx}(in black) and R_{xy}(in red) as V_g varies at B=35 T. Lower inset: optical microscope image of a bilayer graphene device used in this experiment. (b) Schematic of the zero energy LL hierarchy in bilayer graphene at high magnetic field.

3.3 Minimum longitudinal resistance under tilted magnetic field

There are several mechanisms to break the LL degeneracy. As we discussed, the zero energy LL contains spin and valley (layer), orbital degrees of freedom. Since the top and bottom layers are not identical, shear lattice strain or charge impurities may break the layer inversion symmetry. With increasing magnetic field, Zeeman splitting of spin becomes pronounced and electron-electron interactions increase with field as the radius of the cyclotron orbits decrease, which may also break the eight-fold degeneracy. Disorder can smear out the LL spectrum by LL broadening.

The magnitude of charge impurities in this device can be estimated by assuming that ∼2 V offset of the charge neutrality point gate voltage V_D from zero energy reflects an aggregate 1.4×10^{11} cm^{-2} charged impurity density on the bilayer. The location of these charge impurities relative to the back gate can affect the opening of the band gap due to the perpendicular electric field across the $d = 0.34$ nm layer spacing. Assuming that all these impurities reside on the top layer, an upper bound of such a gap could be estimated to be about 9 meV from an unscreened capacitance model. If we consider the screening effect (Castro *et al.*, 2007), however, this valley(layer) splitting gap is likely much smaller than this upper bound, close to the same order as the high-field (B $\gtrsim$ 20T) bare Zeeman energy. Further quantitative analysis of this energy scale requires experimental quantification of the location of the charge impurities, which is beyond the scope of this work.

We can manipulate the magnetic field to discern the origin of the symmetry breaking, since there are two magnetic field-dependent factors that can lead to the lifting of the eight degeneracies: Zeeman splitting of spin, which is given by the total magnetic field B_{tot} through

$$E_z = g\mu_B B_{tot}, \tag{3.2}$$

where μ_B is the Bohr magneton, and g is the gyromagnetic factor for the carriers in bilayer graphene; electron-electron interactions through Coulomb interactions, which are given by

$$E_{e-e} = e^2/\epsilon l_B, \quad l_B = \sqrt{\hbar/eB_\perp}, \tag{3.3}$$

where $\epsilon \sim 4$ is the dielectric constant considering SiO_2 as the interface material and l_B is the magnetic length. In order to produce full eight-fold symmetry breaking, these mechanisms must lift not only the spin and valley degeneracies, but also the $n = 0\,\&\,1$ LL orbital degeneracy. Barlas *et al.* have suggested that the exchange term from Coulomb interactions between electrons in these degenerate orbital states leads to a QH ferromagnetic state where the eight-fold symmetry is lifted by this exchange interaction. A Hund rule-like hierarchical symmetry breaking in the zero energy LL is predicted with this exchange-enhanced Zeeman splitting followed by the spin-independent valley and orbital splitting (Barlas *et al.*, 2008).

In order to test out this hierarchical degenerate lifting and the role of electron-electron interactions, we first note that sublattice or interlayer splittings that are associated solely with the Coulomb interactions between electrons localized in LL orbits should depend only on the perpendicular magnetic field ($B_\perp$) but not the in-plane field ($B_\parallel$). Whereas spin-splitting includes a Zeeman component determined by the total field $B_{tot} = \sqrt{B_\perp^2 + B_\parallel^2}$. Experimentally, this idea can be tested out by measuring the samples in a series of tilted fields where we can examine the R_{xx} minima in different $B_\perp$ and $B_\parallel$ by tuning the tilting angle θ and B_{tot}. Fig. 3.3 displays the change of R_{xx} as a function of the gate voltage normalized by $B_\perp = B_{tot}\cos\theta$, in two different experimental conditions.

In Fig. 3.3(a), we first fix $B_\perp = 20$ T and then vary $B_\parallel$. For $\nu = 2, 3$ QH states, R_{xx}^{min}, the minima of R_{xx} corresponding to the QH zero magnetoresistance, display less than $\sim 10\%$ of variation, indicating that no significant changes are induced by applying $B_\parallel$. For comparison, in Fig. 3.3(b), we show R_{xx} as a function of $B_\perp$ with

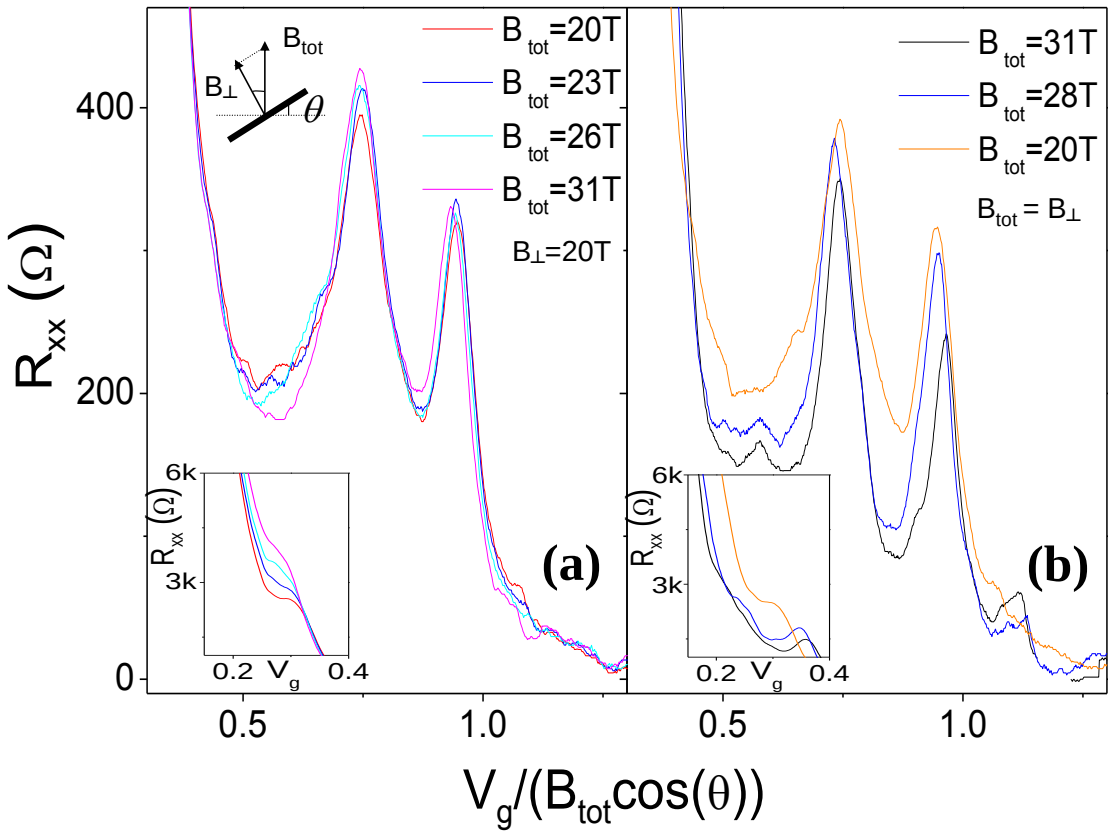

Figure 3.3: (a) Magnetoresistance R_{xx} as a function of normalized back gate voltage $V_g/(B_{tot}\cos\theta)$ around $\nu = 2$ and $\nu = 3$, at four different total magnetic fields with the same perpendicular field. Upper inset: Schematic diagram of tilted field; Lower inset: R_{xx} vs. $V_g/(B_{tot}\cos\theta)$ at $\nu = 1$ state under the same condition as in the main figure. (b)R_{xx} as a function of normalized gate voltage with a zero tilting angle at different total fields, with the same scale of Fig. 3.2(a). Lower inset: R_{xx} vs. $V_g/(B_{tot}\cos(\theta))$ at $\nu = 1$ state. All data are taken at 1.5 K.

fixed $\theta = 0$, that is $B_{\parallel} = 0$ and $B_{\perp} = B_{tot}$. In this case R_{xx}^{min} for $\nu = 2$ and $\nu = 3$ increases by ~ 40 % as $B_{\perp}$ decreases from 31 T to 20 T, a factor of 4 larger change than the change of Fig. 3.3(a) where B_{tot} decreases from 31 T to 20 T while $B_{\perp}$ was kept to 20 T. The fact that R_{xx}^{min}'s for $\nu = 2$ and $\nu = 3$ shows little to no dependence on the in-plane field strongly suggests that both these QH states are from non-spin orgin and thus are due to the breaking of the valley or orbital degeneracy of the zero energy LL.

As for the $\nu = 1$ QH state, the experimental data of its tilted field dependence, shown in the insets of Fig. 3.3, displays an increasing R_{xx}^{min} with either an increasing in-plane field or an increasing normal field. While this evolution is consistent neither with an electron-electron origin nor with a spin one, it is conceivable that the increasing R_{xx}^{min} shown in the inset of Fig. 3.3 (a) is due to the proximity of this filling factor to the increasingly insulating behavior of the bilayer at the charge neutrality point, discussed below. However, given the hierarchy of the degeneracy breaking, schematically shown in Fig. 3.2(b), the mechanism underlying the $\nu = 1$ symmetry breaking should be similar to that for $\nu = 3$, i.e. not from a spin origin, consistent with theoretical predications of the formation of a QH ferromagnet in bilayer graphene at high magnetic fields (Barlas *et al.*, 2008; Abanin *et al.*, 2009).

3.4 Energy gap measurements of $\nu = 1, 2$ and 3

To further understand the nature of the fully lifted LL degeneracy, we determine the energy of the LL splittings by measuring R_{xx}^{min} at different temperatures T. Fig. 3.4(a-c) shows $\log R_{xx}^{min}$ versus $1/T$ for the $\nu = 1,\ 2,$ and 3 states. Since

$$R_{xx}^{min} \propto \exp\left[-(\Delta E - 2\Gamma)/2k_B T\right], \tag{3.4}$$

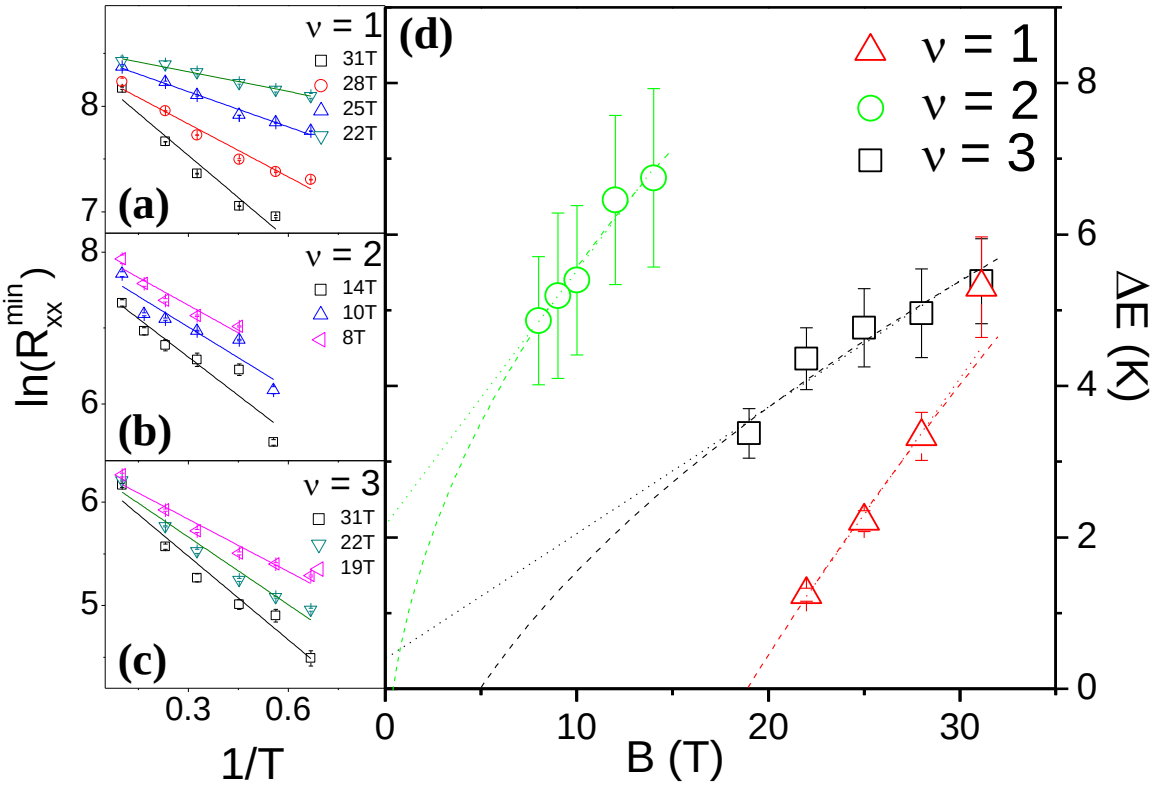

Figure 3.4: (a)Arrhenius plots of R_{xx}^{min}'s as a function of $1/T$ at different fields for $\nu = 1$ state, the lines with respective colors are the linear fits to the data points. (b) Arrhenius plot for $\nu = 2$ state. (c)Arrhenius plot for $\nu = 3$ state. (d)Energy gap ΔE vs magnetic field B for different filling factors $\nu = 1$ (open triangle red), $\nu = 2$ (open circle green), $\nu = 3$ (open square black). The dotted lines are linear fits, whereas the dashed lines are square-root fits.

where ΔE is the energy gap between two subsequent LLs and Γ is the half-width of the LL energy broadening at half-maximum. The observed Arrhenius behavior in these plots allows us to estimate ΔE at different magnetic fields from the slope of the linear fit.

Fig. 3.4(d) displays the field dependence of the activation gap for $\nu = 1$, 2, & 3. Generally, ΔE increases with increasing B as expected. It is also noted that at given B, $\Delta E_{\nu=2} > \Delta E_{\nu=3}$, $\Delta E_{\nu=1}$, indicating that the even ν states have larger energy than the odd ν QH states in accordance with the LL symmetry breaking hierarchy of Fig. 3.2(b).

As for the field dependence, we find that a $\sqrt{B}$ fit is better for $\nu = 2$ and $\nu = 3$ states. Attempts to fit the gap evolution linearly to B result in a positive y-axis intercept for the $\nu = 2$ and $\nu = 3$ gaps and lead to a non-physical negative LL broadening Γ. From the y-intercept of the $\sqrt{B}$ dependence, we can extract a physically reasonable LL broadening of $\Gamma/k_B = 1.4$ and 3.7 K for the $\nu = 2$ and 3 states, respectively (for $\nu = 1$ the measured energy gap is too small to make a reliable fit).

Although the apparent $\sqrt{B}$-dependence provides an independent confirmation of non-spin origin of the QH states $\nu = 2$ and 3, we note that the observed energy scale ΔE is still too small compared to the Coulomb energy or even the bare Zeeman energy. For $B = 15$ T, the Coulomb energy is 370 K and the Zeeman energy $E_z = 21$ K, both larger than $\Delta E_{\nu=2} = 8.6$ K at this field. It is possible that the large amounts of disorder near the charge neutrality point of BLG are responsible for such a reduced transport gap.

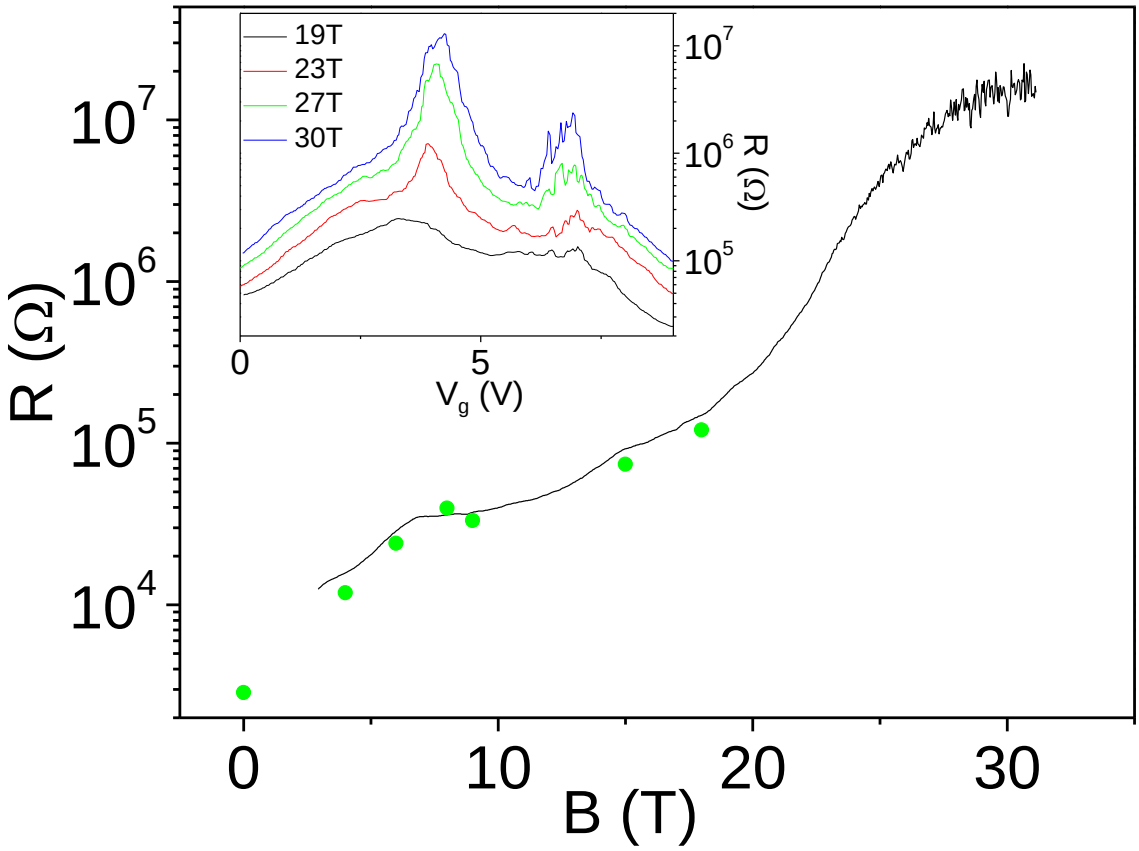

Figure 3.5: Maximum resistance, measured in a two-probe constant voltage bias method, as a function of magnetic field, which is applied normally to the graphene plane, at a fixed gate voltage $V_g = 4.1$ V around the charge neutrality point. The green dots are R_{xx}^{max}'s at $\nu = 0$ using a four-probe measurement. They are taken at lower magnetic fields($B < 20$ T), and multiplied by a factor of 4 to match the 2 probe data. Inset: Gatesweep of two-probe resistance at different fields: 19, 23, 27, and 29 T from bottom to top. All data are taken at 1.5 K.

3.5 $\nu = 0$ insulating state

We finally focus our attention on the $\nu = 0$ QH state. As with monolayer graphene, the presumed $\nu = 0$ splitting at the charge neutrality point is not directly observable as a zero in R_{xx}. Rather, R_{xx} displays a maximum at this point, whose value increases with increasing B. In Fig. 3.5, we display our measurement of R_{xx} at the charge neutrality point in bilayer graphene. The measured resistance shows quasi-exponential growth as B increases, up to ~ 10 MΩ at 30 T.

To avoid the self-heating of the graphene discussed in Checkelsky *et al.* (2009) and to measure resistances > 10 MΩ, we employ a two-probe AC measurement configuration with a constant voltage bias of 500 μV, resulting in only ~ 10 fW of heating at the highest fields. The contact resistance included in this measurement set up is relatively small (~ 1 KΩ), but as an additional confirmation that it does not affect the behavior of the measured resistance, we cross-checked the two-probe measurement using a conventional, current biased, four-probe measurement at fields low enough that the resistance can be reliably measured with the voltage probes input to an amplifier with 10 MΩ input impedance. The exponentially divergent behavior of R_{xx} at high magnetic field is similar to analogous measurements that have been performed on monolayer graphene (Checkelsky *et al.*, 2008, 2009), where a field-induced QH insulator has been proposed. We also note that the gate sweep (Fig. 3.5 inset) displays a growing number of local maximum in R_{xx}, presumably due to the inhomogeneous distribution of these insulating states at high magnetic fields (Das Sarma and Yang, 2009).

3.6 Conclusion and new puzzles

To conclude, we have observed the full degeneracy lifting of the zero energy LL in bilayer graphene. Independent measurements of the longitudinal resistance zeros for the newly observed filling factors as a function of perpendicular field and temperature each indicate that the degeneracy lifting for the $\nu = 1, 2, \& 3$ splittings originates from electron-electron interactions. The field dependence of the longitudinal resistance at the $\nu = 0$ charge neutrality point reveals insulating behavior similar in character to that of single layer graphene.

Note that similar symmetry breaking is also observed in two-probe measurements of suspended bilayer graphene devices by Feldman *et al.* (2009), where they have an emphasis on the study of the insulating $\nu = 0$ state.

Although the results agree in the observation of eight-fold LL splitting and insulating $\nu = 0$, the detailed analysis on the energy gap is to some extent different, since we observed a $\sqrt{B}$ dependence for $\nu = 2, 3$, while Harvard group has a linear B dependent $\nu = 0$. Comparing suspended devices with on-substrate samples, the effective screening from the dielectric makes suspended devices a system with much stronger many-body interactions, and the scale of disorder in suspended devices is about one order of magnitude smaller than that of on-substrate devices. These differences in relative magnitudes in electron-electron interaction and disorder may explain the discrepancy in the observation of the broken symmetry at the zero energy LL in the framework of quantum Hall ferromagnetism. It is important to understand the role of e-e interactions in an inhomogeneous medium. More theoretical and experimental work need to be done to further clarify this issue.

We finally note that the most recent experimental results on bilayer graphene on hexagonal boron nitride substrate provide extremely high quality samples where more quantitative measurements and analysis are possible with an order of magnitude smaller disorder than that presented in this chapter. In those samples reaching the

clean limit, further investigation on the nature of the symmetry broken states can be obtained with less perturbation from the disorder scattering, which will bring new insights to the interpretation we made in this chapter.

Chapter 4

Magnetoresistance measurements of monolayer graphene at the charge neutrality point

In this chapter we report on magnetoresistance measurements at the $\nu = 0$ Landau level filling fraction of monolayer graphene. Using both conventional two-terminal measurements, sensitive to bulk and edge conductance, and Corbino measurements, sensitive only to the bulk conductance, we observed a vanishing conductance with increasing magnetic fields. By examining the changes in maximum resistance/minimum conductivity of this insulating state with varying perpendicular and in-plane magnetic fields, we probe the spin-active components of the excitations in total fields of up to 45 Tesla. Our results indicate that $\nu = 0$ quantum Hall state in monolayer graphene is not spin polarized. This work has recently been submitted (Zhao *et al.*, 2011).

4.1 Introduction

Under a magnetic field, the linear dispersion relation of low energy electron spectrum in graphene leads to unique Landau levels (LLs) whose energy difference is unequally spaced (Zheng and Ando, 2002; Gusynin and Sharapov, 2005; Peres *et al.*, 2006). The LL spectrum, given by Eq. 1.22: $E_n = \pm\sqrt{2|n|\hbar {v_F}^2 eB}$, where v_F is the Fermi velocity and $n = 0, \pm1, \pm2, ...$ is LL index, contains an $n = 0$ level, termed the

zero-energy LL (ZLL). In the absence of appreciable interactions or Zeeman splitting, each LL has a four-fold degeneracy arising from a real spin and valley (or pseudospin) degeneracy. The appearance of the quantum Hall (QH) effect in graphene at the LL filling fractions $\nu = \pm 2, \pm 6, ...$ is a manifestation of this four-fold degeneracy of graphene LLs (Novoselov *et al.*, 2005a; Zhang *et al.*, 2005). In the high magnetic field regime, however, this effective SU(4) spin-pseudospin symmetry can be broken, with more QH plateaus appearing at $\nu = 0, \pm 1, \pm 4$ and developing signatures of QH states for other integer filling fractions (Zhang *et al.*, 2006; Jiang *et al.*, 2007a; Kurganova *et al.*, 2011).

The $\nu = 0$ filling factor that appears at the center of the ZLL presents something of a paradox in QH physics, as it is not marked by the usual longitudinal resistance minima that typify all other filling factors. While initial measurements on disordered samples at this filling factor reported high-field (above 30 T) resistance in the regime of tens of KΩs (Abanin *et al.*, 2007b), subsequent reports on this quantum Hall state have shown a strong insulating behavior as sample mobility is increased (Checkelsky *et al.*, 2008, 2009), with two-terminal measurements of the highest mobility suspended samples measuring into the GΩ range at fields as low as 5 Tesla (Du *et al.*, 2009; Bolotin *et al.*, 2009),

Theoretically, various models of symmetry breaking and ordering underlying this $\nu = 0$ insulating state have been proposed. Most of the models fall into the framework of exchange-driven quantum Hall ferromagnetism that separate different sectors of the SU(4) spin-pseudospin space (Nomura and MacDonald, 2006; Alicea and Fisher, 2006). As shown in Table 4.1, these include a fully spin-polarized ferromagnet (F) (Abanin *et al.*, 2006; Shimshoni *et al.*, 2009), a fully pseudospin-polarized charge density wave (CDW) (Jung and MacDonald, 2009; Herbut, 2007), a Kekule distortion with a spontaneous ordering of pseudospin (KD) (Fuchs and Lederer, 2007; Nomura *et al.*, 2009; Hou *et al.*, 2010), and a canted antiferromagnet (CAF) (Kharitonov,

	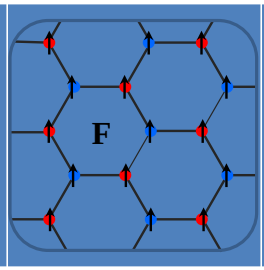	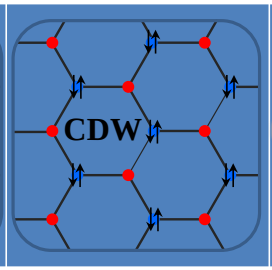	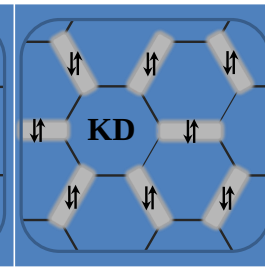	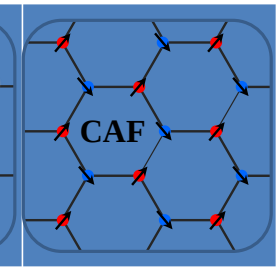
Edge	Gapless	Gapped	Gapped	Gapped
Bulk	Gapped	Gapped	Gapped	Gapped
Net spin	Y	N	N	Y(CAF) N(AF)

Table 4.1: Edge and bulk conduction for the four possible ordered states of $\nu = 0$ under the framework of QH ferromagnetism; the black arrows indicate spin-up (arrows up) and spin-down (arrows down) electrons; A and B sublattices are denoted as red and blue dots. The four ordered states are: **F**, spin-polarized ferromagnetic state; **CDW**, spin singlet charge density wave; **KD**, Kekule distortion, where spontaneous ordering of pseudospin occurs and they are denoted as grey bonds; **CAF**, canted antiferromagnet with spontaneous ordering of spins.

2011). An alternative approach is based on magnetic catalysis: long-range electron interactions that induce an excitonic gap (Gusynin *et al.*, 2006). Experimental reports on the non-zero filling factor (Zhang *et al.*, 2006; Jiang *et al.*, 2007a) suggest that the excitations of the $\nu = 1$ state have no spin, while the Kosterlitz-Thouless insulating behavior of $\nu = 0$ (Checkelsky *et al.*, 2009) is consistent with a Kekule distortion origin. The various models of the broken symmetry states involve unique bulk spin/pseudospin textures and corresponding edge state configurations (Abanin

et al., 2006). Thus transport measurements require careful comparison of the bulk and edge state conduction in order to answer questions related to the nature of the symmetry breaking at $\nu = 0$.

In this chapter we investigate the spin response of the $\nu = 0$ QH state in monolayer graphene by measuring the bulk and edge conduction as a function of in-plane magnetic field using both high-mobility suspended graphene and on-substrate graphene with Corbino geometry. Our experiments reveal a vanishing conductance at the $\nu = 0$ filling factor, but neither measurements exhibit an increasing gap with increasing in-plane field, suggesting that the $\nu = 0$ state is not spin-polarized.

4.2 Edge transport in suspended graphene

The suspended graphene devices are prepared using the methods described in Chap. 2 following Bolotin *et al.* (2008). An atomic force microscope (AFM) image of the device is shown in the inset of Fig. 4.1(c). DC current annealing (as described in Chap. 2) is then performed at low temperature ($T = 1.7$ K) to remove residual impurities from the suspended graphene. Four-terminal transport measurements are conducted using conventional low-frequency lock-in techniques. The carrier density of the graphene is tuned through the series capacitor of residue layer of SiO_2 and a layer of vacuum. The magnitude of the tuned density is determined using Hall measurements through the relation: $n = -\frac{BI}{eV_H}$, where V_H is the hall voltage. The mobility of this annealed device is ~80,000 cm^2/Vs.

In Fig. 4.1(a), we show the longitudinal conductivity σ_{xx} and hall conductivity σ_{xy} versus back gate at $B = 4$ T normal to the graphene basal plane. As indicated by the vertical arrows, along with clearly developed $\nu = 2$ QH state, strong $\nu = 0$ and developing $\nu = 1$ are observed as plateaus in σ_{xy} and the suppression of σ_{xx} at the

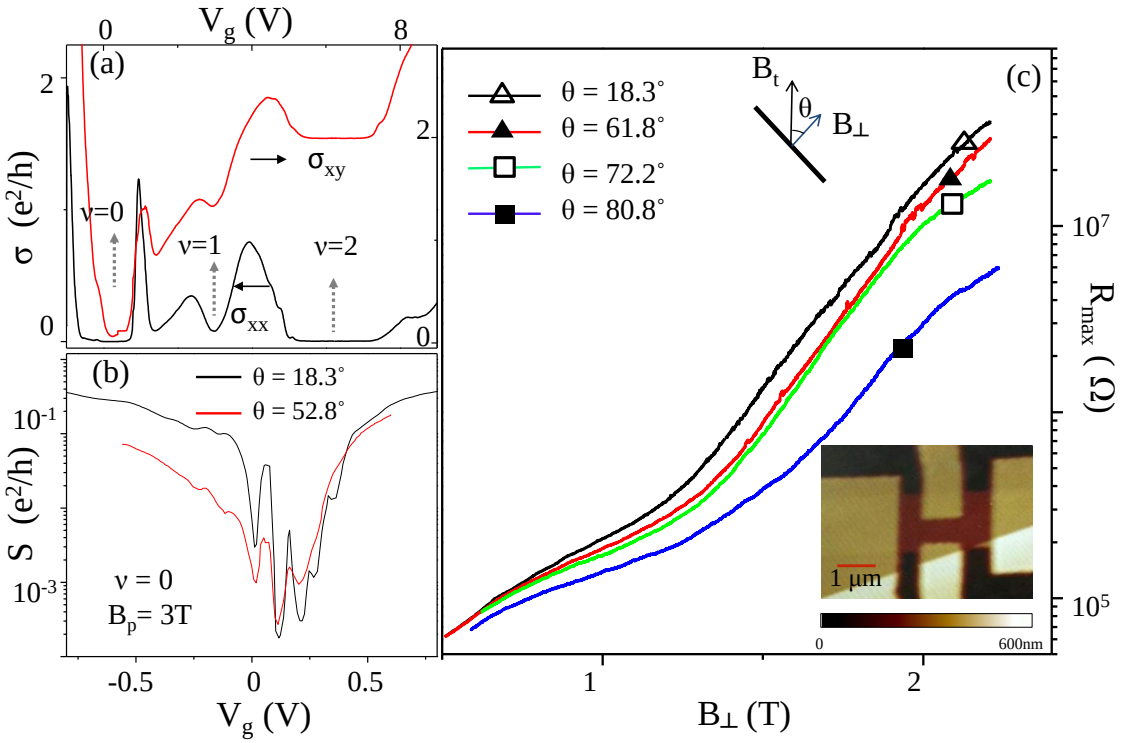

Figure 4.1: (a) Longitudinal conductivity (σ_{xx} in black) and hall conductivity (σ_{xy} in red) as a function of back gate voltage at $T = 1.7$ K with $B = 4$ T; dashed arrows indicate QH states $\nu = 0$, 1, and 2; (b) Conductance (S) on a logarithmic scale versus V_g at $B_\perp = 3$ T for two different tilting angles: $\theta = 18.3°$ and $\theta = 52.8°$; (c) Maximum two-terminal resistance as $B_\perp$ increases for different tilting angles: $\theta = 18.3°$ (open triangle), 61.8° (solid triangle), 72.2° (open square), and 80.8° (solid square); the experimental error of θ is 0.3°; lower right inset: AFM image of the measured suspended graphene device; upper inset shows a schematic diagram for tilting angle and perpendicular and total magnetic field components.

corresponding filling fractions. The appearance of the $\nu = 0$ and $\nu = \pm 1$ QH states indicate that the four-fold degeneracy of the ZLL is completely broken.

To discern whether the $\nu = 0$ symmetry breaking is spin-active, we apply a sequence of tilted magnetic fields that fix the perpendicular magnetic field $B_\perp$ while varying the total magnetic field B_{tot}. By fixing $B_\perp$, the magnetic length $l_B = \sqrt{\hbar/eB_\perp}$ and Coulomb energy scale $E_{e-e} = e^2/4\pi\epsilon_0\epsilon_r l_B$ ($\epsilon_r = 1$ for vacuum is used for suspended devices) are held constant, meaning the electron-electron and exchange interactions that underlie the $\nu = 0$ state are unchanged. However, if this state is fully spin polarized, the current-carrying excitations will have net spins that will be affected by changes in B_{tot} via the Zeeman energy $\Delta E_z = g\mu_B B_{tot}$, where g is g-factor of electron and μ_B is the Bohr magneton. At fixed temperature the changes to the carrier excitation energy will result in a change in conductance observed at the $\nu = 0$ filling factor. Thus by tuning only the Zeeman energy and examining changes in the conductance, we can determine if the activation of the $\nu = 0$ state is spin-sensitive.

The results of measuring the insulating state of the suspended device at several different tilting angles are shown in Fig. 4.1(c), where the resistance maximum R_{max} is measured at the charge neutrality point $V_g = V_D$, at a fixed base temperature $T = 1.6$ K. Since the resistance for $\nu = 0$ QH state tends to increase rapidly as a function of B (Checkelsky *et al.*, 2008, 2009; Du *et al.*, 2009; Bolotin *et al.*, 2009), R_{max} is a good measure to probe this intriguing 'insulating' state. Here we use two-terminal current measurement with a constant voltage bias in order to eliminate any self-heating effects ($\leq$ pW) and to maximize the measurable resistance range. At $T = 1.7$ K, we found that R_{max} increases from $\sim$10 KΩ up to 100 MΩ (comparable to the limit of our measurement set-up) as $B_\perp$ changes from 0 to 3 T. The tilting angle dependence of R_{max} versus $B_\perp$ curves show an interesting trend: while we do not observe appreciable dependence of R_{max} on in-plane magnetic field at lower values of the tilting angle θ (i.e., larger $B_\perp/B_{tot}$ ratio), there is an indication that R_{max}

decreases at larger θ (i.e, smaller $B_\perp/B_{tot}$ ratio). This trend becomes most obvious for the largest tilting angle we measured, θ =80.8°, corresponding to $B_\perp/B_{tot}$, where we observe that R_{max} versus $B_\perp$ curve is substantially lower than any other curves in the graph. The observed trend in the suspended device, i.e., decreasing R_{max} with decreasing $B_\perp/B_{tot}$ at fixed $B_\perp$ can be viewed as strong evidence against the spin-polarized ordering of the $\nu = 0$ QH state.

4.3 Corbino geometry for bulk measurements

There are two obstacles in using suspended samples to draw more quantitative conclusions about the nature of the $\nu = 0$ QH state. First, due to the mechanical instability of suspended samples, R_{max} drifts slightly with respect to V_g. Fig. 4.1(b) shows the conductance as a function of V_g measured at two different tilting angles. Although the overall behavior is consistent, the position of V_g where R_{max} occurs is slightly shifted. Even worse, this shift changes when the device is thermally cycled, making it difficult to estimate the energy gap by the thermally-activated behavior. Second, the four-/two-terminal device geometry measures both the bulk conductance and any possible edge conductance in parallel. This becomes a major source of ambiguity in distinguishing whether the observed insulating behavior originates from the bulk insulating state without the edge conduction or from the localization of edge states by spin/pseudospin-flip scattering (Abanin *et al.*, 2006, 2007b). In order to avoid the mechanical instability and to isolate the bulk conductance, we employ an on-substrate Corbino geometry, a disk-shaped sample with coaxial contacts in which the current flows radially from an inner contact to an outer ring contact. This geometry not only eliminates any unknown edge effects that might interfere with determining the $\nu = 0$ conductance, but is also insensitive to the formation of the known quantized edge conductances of other filling factors, as shown in Fig. 4.2. This

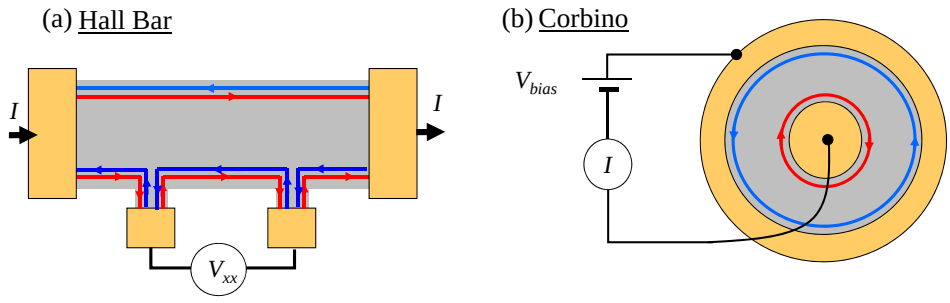

Figure 4.2: (a) Schematic top view of a Hall bar device with counter-propagating edge states, where edge and bulk transport are mixed for two-probe measurements; (b)Schematics top view of a device with Corbino geometry, where only bulk conduction is measured.

geometry then allows directly probing bulk conduction, and thus puts the $\nu = 0$ insulator on an even footing with the bulk insulating character of every other filling factor (Das Sarma and Yang, 2009).

The fabrication procedure for our Corbino devices is shown as in Fig. 4.3(a). Monolayer graphene pieces are deposited on SiO_2 (300 nm)/Si substrates using established mechanical exfoliation techniques, then Cr/Au (1/40 nm) ring-like electrodes are fabricated by e-beam lithography, (an optical image is shown in Fig. 4.3(b)), followed by a dielectric layer deposition and a top Cr/Au plate contact to connect to the inner contact (as shown in Fig. 4.3(c)). The plate geometry connecting to the inner contact guarantees that any voltage applied to this contact will result in a uniform change to the graphene carrier density. To measure the bulk conductance of the graphene we apply an AC voltage bias (V_{bias}) across the inner and outer contacts, and measure the current (I) using a current preamplifier and a lock-in amplifier. The

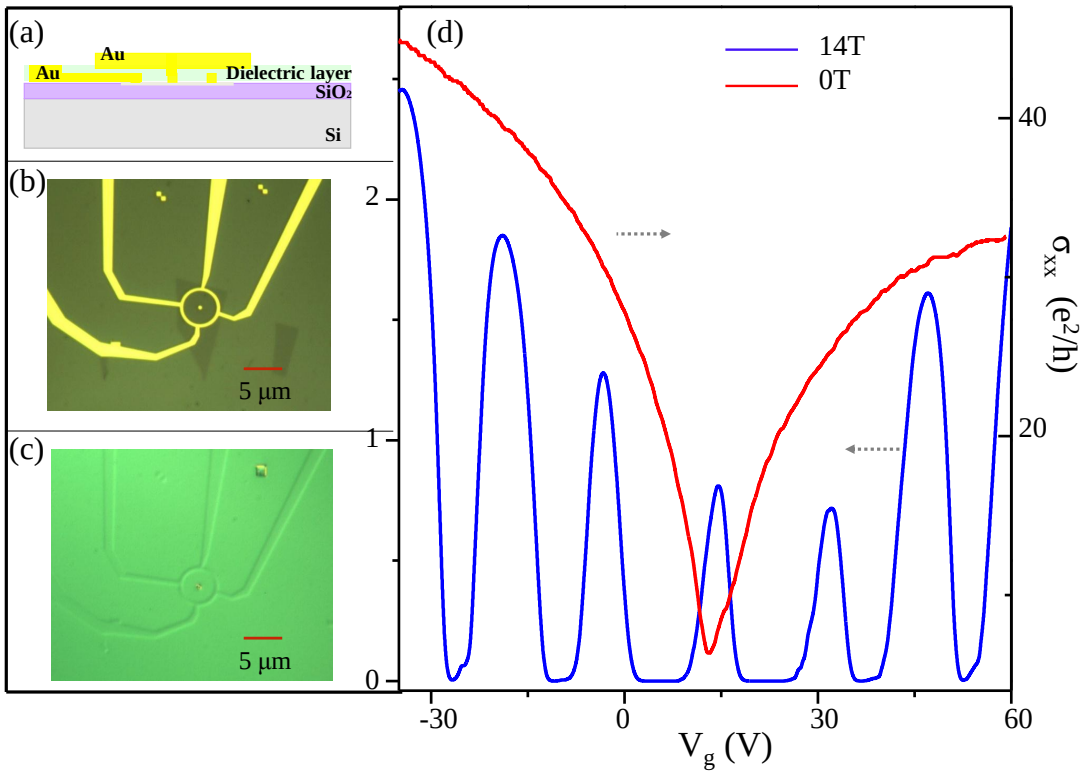

Figure 4.3: (a) Schematic side view of a Corbino device; (b) Optical device image before the inner electrode is contacted by the ground plate; (c) Optical image of a finished device; (d) Bulk Conductivity σ_{xx} as a function of back gate voltage V_g at zero field (in red) and 14 T (in blue), at $T = 7$ K.

bulk conductivity is then given by

$$2\pi\sigma_{xx} = \frac{I}{V_{bias}} \ln \frac{r_{out}}{r_{in}}, \tag{4.1}$$

where r_{out} and r_{in} are the radii of the outer and inner contacts, respectively.

Changing the back gate voltage V_g, we can tune the carrier density in the graphene channel connected by the inner and outer contacts of the Corbino device. Fig. 4.3(d) shows the bulk conductivity σ_{xx} vs. back gate voltage V_g, at $B = 0$ T and 14 T at temperatures lower than 7 K. The mobility of this particular Corbino device is

$\sim$13,000 cm^2/Vs, obtained from the zero-field data. At $B = 14$ T, the four-fold degenerate QH state filling factors $\nu = \pm 2, \pm 6, \pm 10$ appear as vanishing σ_{xx} at their corresponding carrier density. The gate capacitance of this device is estimated to be $C_g/e = 7.2 \times 10^{10}$ cm^{-2}V^{-1} from the position of the observed conductivity minima.

4.4 Lifted degeneracy in bulk transport

Since the mobility of the on-substrate Corbino devices is lower than that of the suspended devices, relatively higher magnetic fields are required to access the degenerately broken filling factors. With the assistance of the highest manmade static magnetic field in the world (45 T hybrid magnet at NHMFL in Tallahassee, Florida), we are able to access the fully lifted degeneracy of the zero energy LL, even under tilted magnetic field.

As shown in Fig. 4.4, at low field ($B = 11.5$ T) well-defined $\nu = \pm 2$ states are observed on both sides of the charge neutrality point, indicative of the four-fold QH degeneracy. As the magnetic field increases to 18 T, a dip of bulk conductivity appears at the charge neutral point. This dip fully evolves and the current flow falls below the noise level at $B = 30$ T. This observation of a vanishing bulk conductivity is consistent with the formation of the $\nu = 0$ QH state (Das Sarma and Yang, 2009). At the same magnetic field, the conductivity minima corresponding to the $\nu = \pm 1$ filling factors are visible. At $B = 45$ T, the four-fold degeneracy at the zero energy level is completely lifted, and the LL splitting at $\nu = -4$ that marks the degeneracy breaking of the $n = 1$ LL is apparent, similar to the previous observation (Zhang *et al.*, 2006). In all measured devices, the magneto conductance is strongly suppressed in the regime between the $\nu = -1$ and $\nu = -2$ filling factors and is not measurable within our experimental sensitivity.

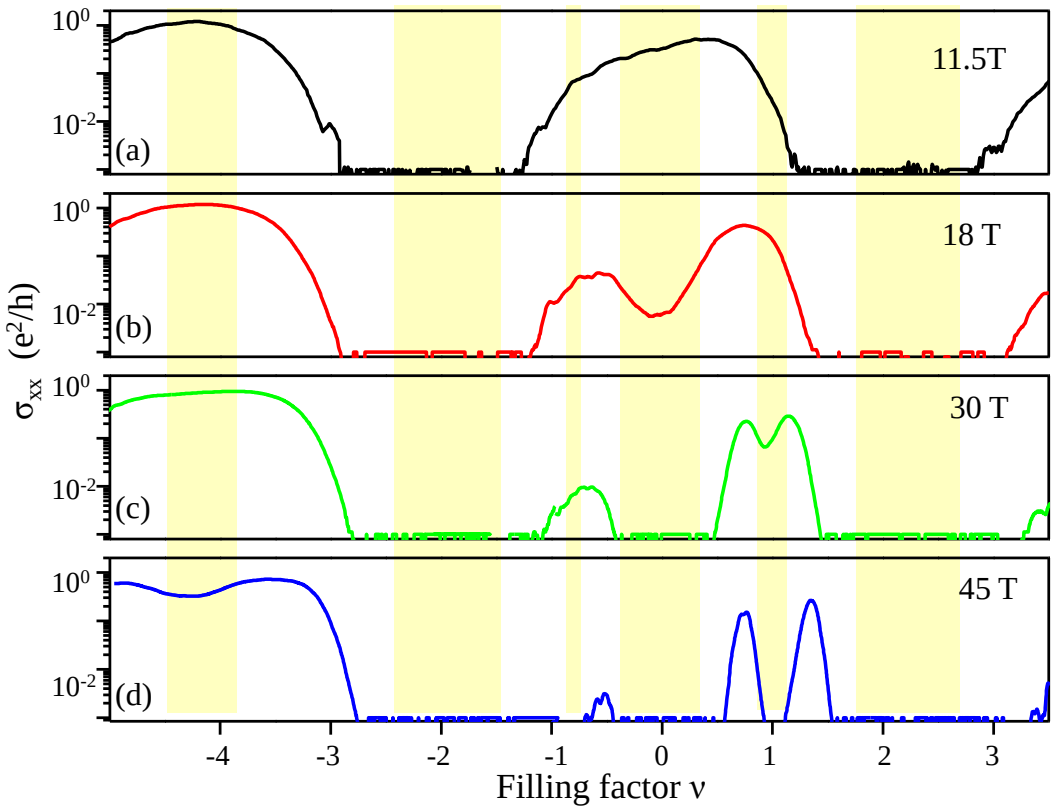

Figure 4.4: (a) σ_{xx} as a function of filling factor at four perpendicular magnetic fields at $T = 1.7$ K. The shaded bands highlight the developing filling factors as the four-fold degeneracy of the ZLL is broken, each manifested as a vanishing bulk conductance.

4.5 Bulk conductivity of $\nu = 0$ and 1 with increasing in-plane magnetic field

As with the suspended devices, we adjust the relative strengths of the Zeeman and Coulomb energy in the Corbino devices by tilting the field in order to explore the nature of the $\nu = 0$ degeneracy breaking. In Fig. 4.5(a), σ_{xx} vs. filling factor ν is plotted with constant normal field ($B_\perp = 21$ T) and increasing total field ($B_{tot} = B_\perp/\cos\theta$). Taking the dielectric constant ϵ_r=4 (averaging the dielectric constant on both side of graphene), the characteristic Coulomb interaction energy at $B_\perp = 21$ T is $E_{e-e} = 740$ K with $\epsilon_r = 4$, while the Zeeman energy varies from $E_z = 47$ K at $B_{tot} = 35$ T to $E_z = 60$ K at $B_{tot} = 45$ T. As the Zeeman energy is increased, the behavior of the $\nu = 0$ and $\nu = 4$ states are completely different. For the $\nu = \pm 4$ QH state, the σ_{xx} minima decrease with increasing B_{tot}, indicating that a spin polarization underlies this LL, a finding consistent with previous experiments on Hall bar devices (Zhang *et al.*, 2006). In contrast, the conductance curves of the $\nu = 0$ state coincide with each other as the total field is increased from $B_{tot} = 35$ T to 45 T. The conductance minima are invariable even in a magnified logarithmic-scale view, as shown in the middle inset of Fig. 4.5(a). The fact that this minima is independent of changes in the in-plane field is consistent with the tilted-field measurements of the suspended device, and adds further credence to the hypothesis that the $\nu = 0$ symmetry breaking is not of spin origin.

We also perform fine-tuned tilted field measurements in a range where the change of Zeeman energy is larger (increased by 50%) and the $\nu = 0$ minima is more sensitive to small changes in $B_\perp$. Fig. 4.5 (b) shows a log-scale σ_{xx} vs. filling factor ν at $B_\perp = 14$ T and 15 T. As the normal field increases by $\sim 6\%$, there is a decrease in the bulk conductivity minima, showing that the $\nu = 0$ state is not yet fully developed. Increasing the total field by $\sim$ 50% while fixing $B_\perp$, the minima display the same

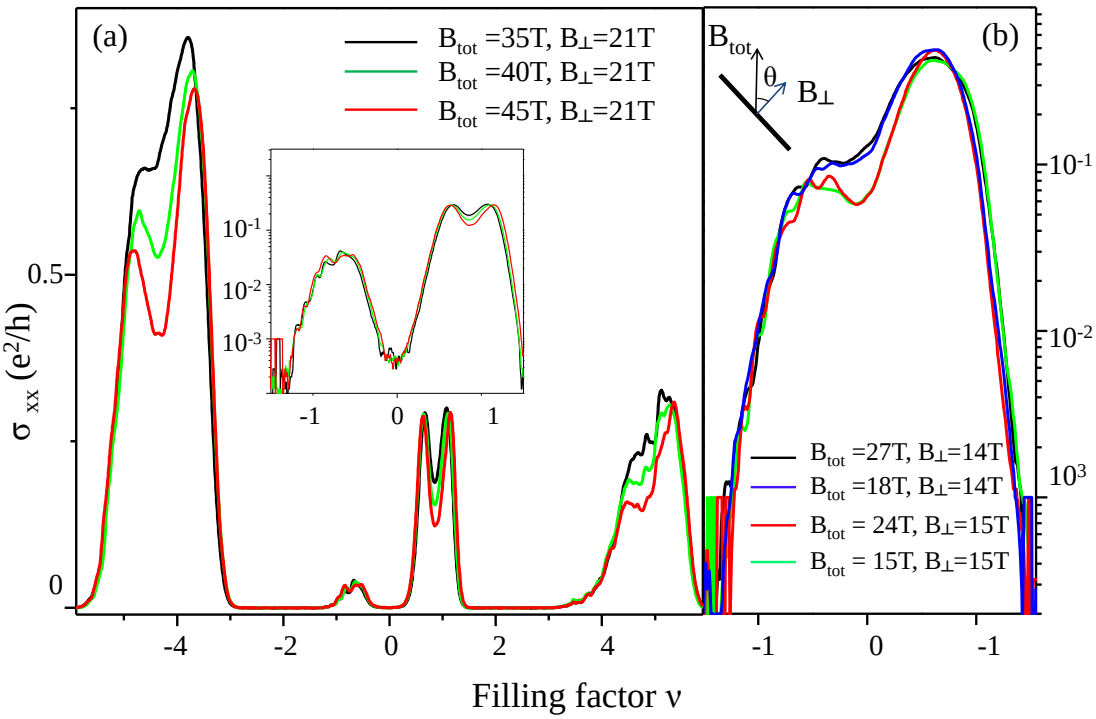

Figure 4.5: (a) σ_{xx} as a function of filling factor at a constant perpendicular magnetic field $B_\perp = 21$ T, for several different total magnetic field. Temperature is fixed at 1.7 K. From top to bottom the corresponding total fields are $B_{tot} = 35$, 40, and 45 T, respectively. The inset shows a close-up of the main panel at the $\nu = 0$ QH state; (b) σ_{xx} at $B_\perp = 14$ and 15 T, where it is sensitive to small changes in the perpendicular field.

insensitivity to in-plane field as in Fig. 4.5(a), reaffirming that the excitations of the $\nu = 0$ state have no net spin.

As for the $\nu = 1$ QH state, experimental data of its tilted-field dependence is also shown in Fig. 4.6. The σ_{xx} minima at this filling factor decrease as B_{tot} increases from 40 T to 45 T, with a slightly decreasing perpendicular field from 40 T to 39.3 T,

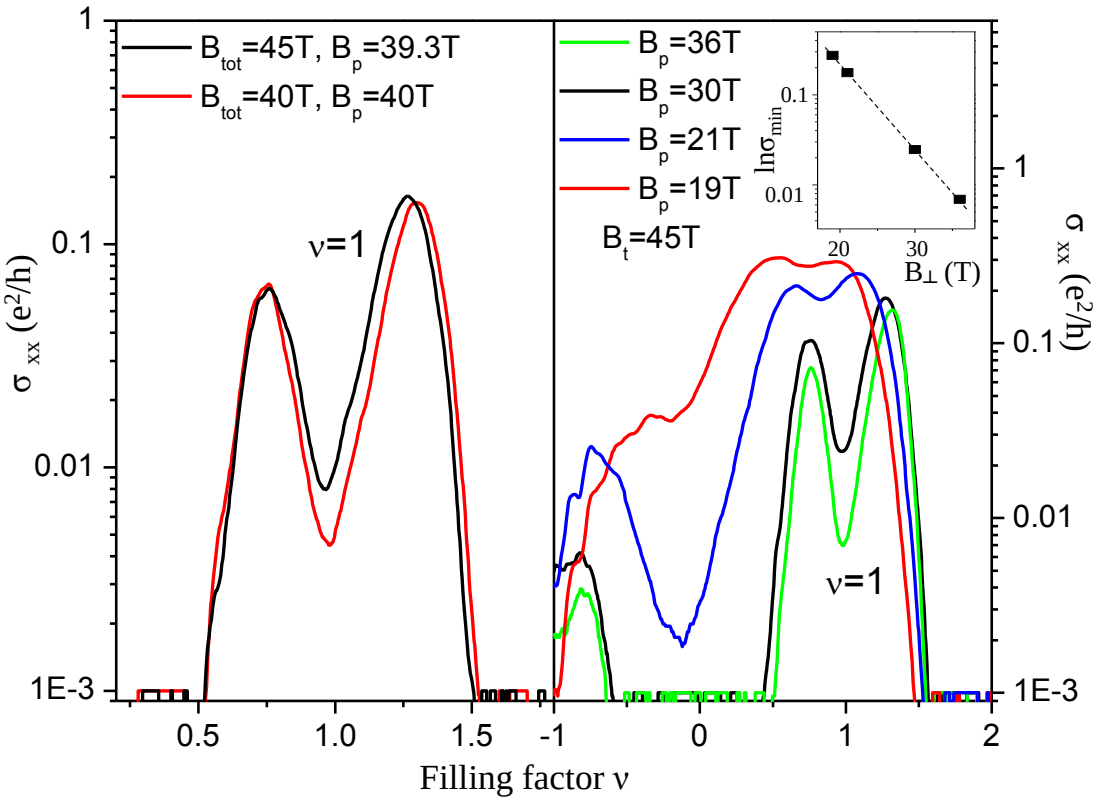

Figure 4.6: (a) σ_{xx} at $\nu = 1$ under two different total magnetic field from 40 T to 45 T with slightly decreased perpendicular field (from 39.3 T to 40 T). (b) σ_{xx} at fixed total magnetic field (45 T) with increasing tilting angle: the corresponding $B_\perp = 36, 30, 21, 19$ T from bottom to top. Inset: σ_{xx}^{min} at $\nu = 1$ vs. $B_\perp$ in a natural logarithmic scale; the straight dotted line is the linear fit of $\ln\sigma_{xx}^{min}$ as a function of $B_\perp$.

indicating that a spin flip excitation occurs. Fig. 4.6(b) also shows that the gap also responds to perpendicular magnetic field, as σ_{xx} minima decreases with increasing perpendicular field. The data in Fig. 4.6(b) could be qualitatively explained by the disorder-induced LL broadening. The inset of Fig. 4.6(b) shows the plot of σ_{xx}^{min} as a function of $B_\perp$. And the linear fit of σ_{xx}^{min} to $B_\perp$ implies that the width of broadened

	Mobility $cm^2V^{-1}s^{-1}$	B_t (T)	B_p (T)	Zeeman (K) $(g\mu_B B_t)$	Coulomb (K) $e^2/\epsilon l_B$	Minimum Conductivity
Corbino $\epsilon = 4$	13,000	18→27	14	23→34	607	No Change within experimental error
		35→45	21	45→60	743	No Change within experimental error
Suspended $\epsilon = 1$	80,000	2.1→6.5	2	2.8→8.7	919	No Change within experimental error
		6.5→12.5	2	8.7→16.8	919	Sharp increase as increasing zeeman

Table 4.2: Comparison of the Zeeman energy and Coulomb energy scales and the minimum conductivity behaviors between the on-substrate Corbino device and the suspended device.

LL (2Γ) may have a $B_\perp$ dependence. Nevertheless, we are certain that the origin of $\nu = 1$ is due in part to a lifting of real spin degeneracy.

4.6 Discussion

Combining the observation of $\nu = 0$ and $\nu = 1$ states, it produces a symmetry-breaking picture of the ZLL where a non-spin polarized state forms at $\nu = 0$ and a, at least partially, spin-polarized state with spin-flip excitations forms at $\nu = 1$.

We are aware that the observation of the spin-active $\nu = 1$ character is inconsistent with the observations in Jiang *et al.* (2007a), whose measurements implied that the $\nu = \pm 1$ QH states are not spin-polarized. This raises the possibility that the excitations at $\nu = 1$ and its ground state may depend on the specific disorder concentration in individual samples (Nomura and MacDonald, 2006; Goerbig *et al.*, 2006). However, the fact that the insulating $\nu = 0$ state does not decrease with decreas-

ing in-plane magnetic fields in both suspended and Corbino devices, where disorder densities are very different, provides evidence that disorder effects do not alter our conclusion that the $\nu = 0$ QH state is not a spin-polarized state for a wide range of disorder (i.e. we exclude the possibility of a spin-ferromagnetic state for $\nu = 0$).

Furthermore, although the tuning range of Zeeman energy to Coulomb energy are very similar as shown in Table 4.2, the behavior of $\nu = 0$ are not exactly the same in suspended graphene compared with on-substrate graphene: minimum conductivity increased (i.e. gap closing) at the highest Zeeman energy even after considering experimental error. This observation assures that disorder may affect the ground state ordering, and it also hints a possible existence of a CAF state (Kharitonov, 2011), where the ground state energy could be adjusted by in-plane magnetic field. Note that very similar results were obtained in graphene samples on hexagonal boron nitride substrate (Young, 2011). Detailed analysis of the bulk and edge charge excitations are needed to further clarify the ordering and to reveal the phase transitions.

4.7 Conclusion

To conclude, our experiments show that both edge and bulk conductances are vanishing at the $\nu = 0$ filling fraction, but neither measurements under tilted magnetic field exhibits an increasing gap with increasing Zeeman energy, suggesting a non-spin-polarized $\nu = 0$ state.

Chapter 5

Quantum Hall edge transport across graphene monolayer-bilayer junction

In this chapter, we first present a surface potential study across the interface of a monolayer and bilayer graphene (MG/BG) junction. Then we present the experimental investigations of the transport property across the MG/BG interface in the quantum Hall regime. Both the monolayer graphene (MG) portion and the bilayer graphene (BG) portion develop their own Landau levels under high magnetic field. While the transport measurements show their distinct quantum Hall effects separately, the transport measurement across the interface exhibits unusual behavior. The transverse resistance across the MG/BG interface is asymmetric for opposite sides of the Hall bar, and the polarity of the asymmetric behavior can be shifted by reversing the magnetic field direction. When the QH plateaus of MG part and BG part overlap, quantized resistance appears only on one side of the Hall bar electrode pairs that sit across the junction. These experimental observations can be ascribed to the QH edge state transport along the MG/BG interface.

5.1 Introduction

As discussed in Chap. 1, in the presence of a magnetic field, the nature of the Dirac fermions in MG and BG results in unevenly spaced Landau levels(LL) containing a distinctive LL at the electron-hole degenerate zero energy, given by

$$E_{n_{MG}^{\pm}} = \pm v_F \sqrt{2e\hbar n_{MG} B} \tag{5.1}$$

for MG (Haldane, 1988) and by

$$E_{n_{BG}^{\pm}} = \pm \hbar\omega \sqrt{n_{BG}(n_{BG}-1)} \tag{5.2}$$

for BG (McCann and Falko, 2006), where $\omega = eB/m$ is the cyclotron frequency with the BG band mass $m \approx 0.04\, m_e$, and n_{MG} and n_{BG} are non-negative integers representing Landau orbit indices for MG and BG respectively.

An example of a MG/BG junction studied in this work is shown in Fig. 5.1(a), where the left half BG sits seamlessly next to the right half MG. Since the charge neutrality points of MG and BG parts are comparable as shown in Fig. 5.1(a), MG and BG parts share similar density of charge carriers. At the MG/BG interface, the work function difference between MG and BG could potentially lead to charge redistribution (Berger *et al.*, 2006), generating surface potential difference. Thus it is appealing to study how the surface potential transition occurs near the interface. Moreover, at high magnetic fields, Landau levels form differently in MG and BG, as shown in Fig. 1.7(b). Edge state conduction, especially at the MG/BG interface, would be an important subject to be understood. Recently, there are several theoretical studies on the transport property of such MG/BG junction system (Mikito Koshino, 2009; Nakanishi *et al.*, 2010). Experimentally, Puls *et al.* (2009) reported anomalous quantum oscillations in two-probe measurements on hybrid monolayer and bilayer graphene structures, where their MG/BG interface continues from source contact to drain contact. However, the contribution of MG/BG interface in the observed quantum oscillation in the two probe conductivity was unclear.

In this work, we first report on measurements of the surface potential across the interface of a MG/BG junction, exploring the local density of states variation at the junction interface. Then we present the quantum edge transport across the MG/BG interface. We propose boundary edge channels along the MG/BG interface are responsible for the observed asymmetric transverse resistance behaviors, and find good quantitative agreement of experimental observations with a theoretical modeling.

5.2 Surface potential mapping

The graphene devices are fabricated and thermal annealed to clean sample surface for surface potential study, following the method described in Chap. 2. Our device geometry is the following: as shown in Fig. 5.1(a), all the measured devices have their source and drain electrodes on each end, with the other eight electrodes on the side of MG part and BG part. This geometry allows us to probe the transverse and Hall voltage on MG and BG parts separately, as well as the transport property across the MG/BG interface. A gate voltage V_g is applied to the desperately doped Si substrate to control the carrier density n_s according to the relation $n_s = C_g(V_g - V_D)/e$, where $C_g = 7.1 \times 10^{10}\, e/\mathrm{V} \cdot \mathrm{cm}^{-2}$ and V_D is the gate voltage corresponding to the charge neutrality point.

Employing scanning kelvin probe microscopy (SKPM) which is capable of scrutinizing contact potential difference (V_{CPD}) between the conductive tapered tip and the sample surface, we can track the local surface potential variation at the MG/BG interface. SKPM measurements at this work are performed in nitrogen atmosphere by commercial AFM (XE-100, Park Systems Corp.). We apply AC voltage with an amplitude of $\sim 0.3 - 1V$ and a frequency of 17kHz to a Cr/Au coated conductive tip. The V_{CPD} signals are obtained by measuring this AC voltage with a lock-in amplifier and applying a feed-back DC voltage to cancel the electrostatic force between

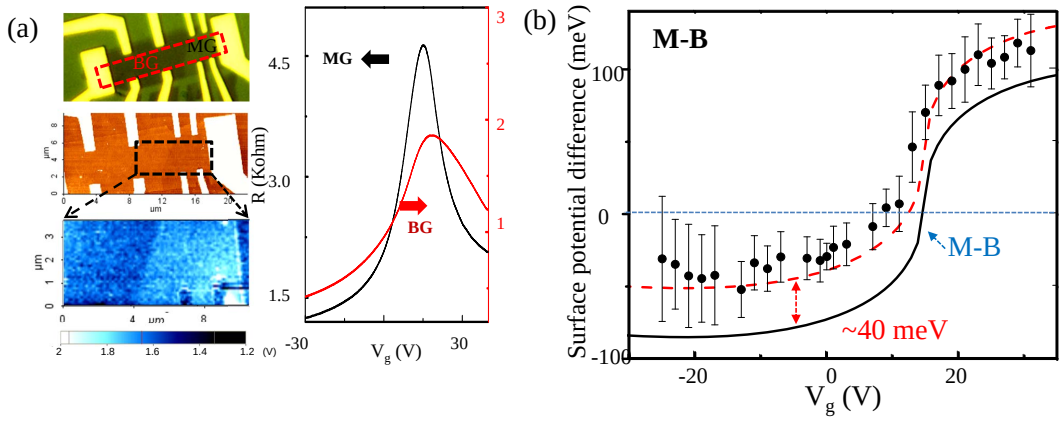

Figure 5.1: Surface potential mapping of a MG/BG junction device. (a) Left panel: Optical(top), topography(middle) and V_{CPD} (bottom) images of a MG/BG junction device at $V_g = 25$ V; Right panel: Gate sweep of the longitudinal resistance of MG and BG parts respectively; (b) Work function difference ($V_{CPD}^{MG} - V_{CPD}^{BG}$) between MG and BG parts at different back gate voltages; black solid line is the theoretical Fermi energy variation of MG and BG, considering their individual CNP's; red dashed line is the work function variation deduced from the black solid line, taking into account of 40 meV offset workfunction between MG and BG.

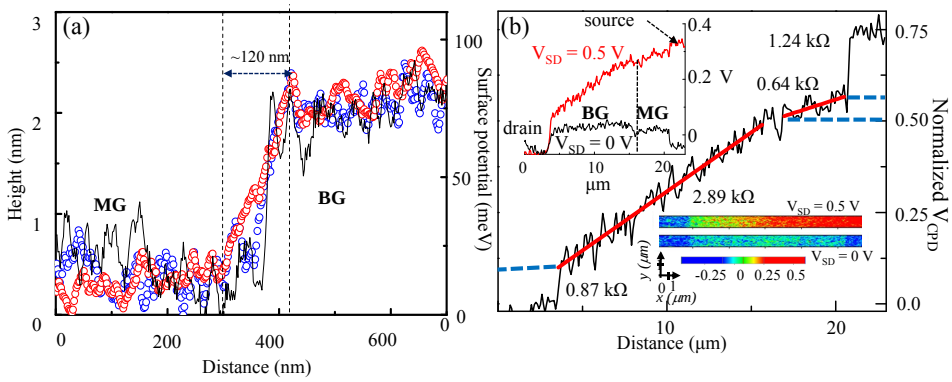

Figure 5.2: Surface potential mapping of a MG/BG junction device: MG/BG interface properties. (a) Selected line profiles across the MG/BG interface from another device: black solid line is the height profile, while open circles (blue and red) are the surface potential profiles at two different locations of the interface; (b) Lower right inset: V_{CPD} mapping of the red dashed box area in the optical image in Fig. 5.1(a) at $V_{SD} = 0$ and 0.5 V; upper left inset: y-axis averaged potential data from the bottom right inset; main panel: normalized potential profiles $\frac{V_{CPD}(V_{SD}=0.5V)-V_{CPD}(V_{SD}=0V)}{V_{CPD}(V_{SD}=0.5V)}$ from data in the upper left panel.

the conductive tip and graphene surface. We use a "two-way scan method" to avoid topographic artifacts convoluted in the surface potential mapping. The first scan is for topography images in non-contact mode with a dithering resonant frequency $\sim$ 120-170 KHz and the second scan is for SKPM image with 10$\sim$30 nm constant tip height away from sample surface.

Fig. 5.1(a) shows the topography and surface potential image on the interface area of the MG/BG junction device at $V_g = 25$ V, as well as the longitudinal resistance as a function of gate voltage for MG and BG parts seperately. The charge neutrality points of the MG and BG parts are 15 V and 18 V, respectively, which indicates an initial doping difference. The work function difference between MG and BG ($W_{MG} - W_{BG}$) can be calculated from $-e(\Delta V_{CPD}^{MG} - \Delta V_{CPD}^{BG})$, as plotted in Fig. 5.1(b). The experimental plot agrees with the theoretical prediction of the Fermi energy difference between MG and BG considering a $\sim$ 40 meV work function difference between MG and BG parts. For MG, $E_f^{MG} = \pm\hbar v_f\sqrt{\pi|n_{MG}|}$, while for BG, $E_f^{BG} = \hbar^2\pi n_{BG}/2m^*$, where n_{MG} and n_{MG} are the carrier density of MG and BG region deduced from their V_D's, and $m^* \approx 0.04m_e$.

Generally, the lateral resolution of height change between MG and BG is $\sim$ 20 nm in the topographic profiles (black solid line in Fig. 5.2(a)), and the transition of surface potential from MG to BG occurs within $\sim$ 120 nm lateral distance (open circled lines in Fig. 5.2(a)), which implies the potential interface length of the MG/BG junction. Note that our SKPM tip is commercialized Cr/Au coated with $\leq$ 50 nm lateral resolution.

The contact effect from the work function difference across the MG/BG junction can also be studied using this surface potential probing technique. As shown in the lower inset of Fig. 5.2(b), we map V_{CPD} of the area enclosed by the red dashed box in the optical image of Fig. 5.1(a) with two different external voltage bias from the source and drain electrodes ($V_{SD} = 0$ V and $V_{SD} = 0.5$ V). By av-

eraging V_{CPD} along the y-axis, we obtain the normalized potential profile as shown in the main panel of Fig. 5.2(b), where the normalized potential is calculated by $\frac{V_{CPD}(V_{SD}=0.5V)-V_{CPD}(V_{SD}=0V)}{V_{CPD}(V_{SD}=0.5V)}$. This allows us to partition resistance contributions from graphene channels and the contacts (Yu *et al.*, 2009). The electrical potential drop from the source and drain contacts can be correlated to the total resistance change between the two contacts. Any sudden kink with discrete slope change that appears in the normalized potential plot is considered as change of local resistivity. The two-probe resistance, which is measured as 5.6 KΩ, includes resistances of MG and BG parts, contact resistances between electrodes and graphene, and contact resistance across the MG/BG interface. From Fig. 5.2(b), we find that the contact resistances between graphene and electrodes are 1.2 KΩ and 0.9 KΩ, respectively. However, no appreciable potential drop is observed across the MG/BG interface, indicating a sharp and high quality interface between the two regions.

5.3 Quantum transport on the edges

In this section, we present magneto-transport property of this junction system. The inset of Fig. 5.3(a) shows the optical microscope image of the device measured in this study. The electrodes are numbered from 1 to 10. Note that the following experiments are carried out using lock-in amplifiers at an excitation current of 100 nA through contact 1 to contact 6. For most MG/BG junction devices we have measured, there is a slight offset of the charge neutrality point between the MG part and the BG part. Fig. 5.3(a) shows the gate dependence of the resistivity of both MG and BG region at 1.7 K. Both the MG and BG region have a mobility of $\sim 4,000$ cm^2/Vs measured at the hole density $n = 4 \times 10^{12}$ cm^{-2}. The transverse resistance and Hall resistance of MG and BG region are measured at $B = 9$ T and $T = 1.7$ K, as shown in the inset of Fig. 5.3(b). As the back gate voltage changes the carrier density, QH

plateaus in R_{xy} with corresponding zeros in R_{xx} are observed. The Hall conductivity of both, deduced from the relation in Eq. 3.1 , are plotted as a function of gate voltage in Fig. 5.3(b). For this particular device, the calculated σ_{xy} of MG part shows well quantized plateau values at $\frac{1}{\nu}\frac{h}{e^2}$ with the integer filling factor $\nu = \pm 2, \pm 6, \pm 10...$, while for BG part, only $\nu = -4$ quantum Hall state is pronounced. $\nu = -4$ state of the BG part overlaps with $\nu = -2$ state of the MG part at the same back gate voltage ranges because of the charge neutrality point offset.

We then investigate the quantum transport behavior across the MG/BG interface. Under the same magnetic field $B = 9$ T, Fig. 5.4(a) displays the transverse resistances across the interface on each side of the junction device as a function of back gate voltage. As shown in the inset of Fig. 5.4(a), the upper side transverse resistance is denoted as R_{2-4} while transverse resistance of the other side is R_{10-8}, with current flowing from contact 1 to contact 6. Note that R_{2-4} and R_{10-8} are asymmetric and completely differ from each other. Upon close inspection at the regime $V_g \in [0, 3]$ V, on one side R_{2-4} vanishes, while on the other side R_{10-8} exhibits a quantized plateau with a non-zero value. Once the magnetic field is flipped to $B = -9$ T, the polarity of two sides changes, i.e., at similar back gate regime, R_{10-8} vanishes while R_{2-4} raises up to the non-zero quantized plateau, on the contrary to the case with positive magnetic field.

5.4 Edge state along the interface boundary

The asymmetric transverse resistance across the MG/BG interface and the polarity change in Fig. 5.4 can be understood using a Landauer-Büttiker type argument with edge channels traveling along the interface boundary. Fig. 5.5 presents a schematic diagram describing the connection of the edge states and interface boundary channels of the MG/BG junction device. In a standard edge state picture of the

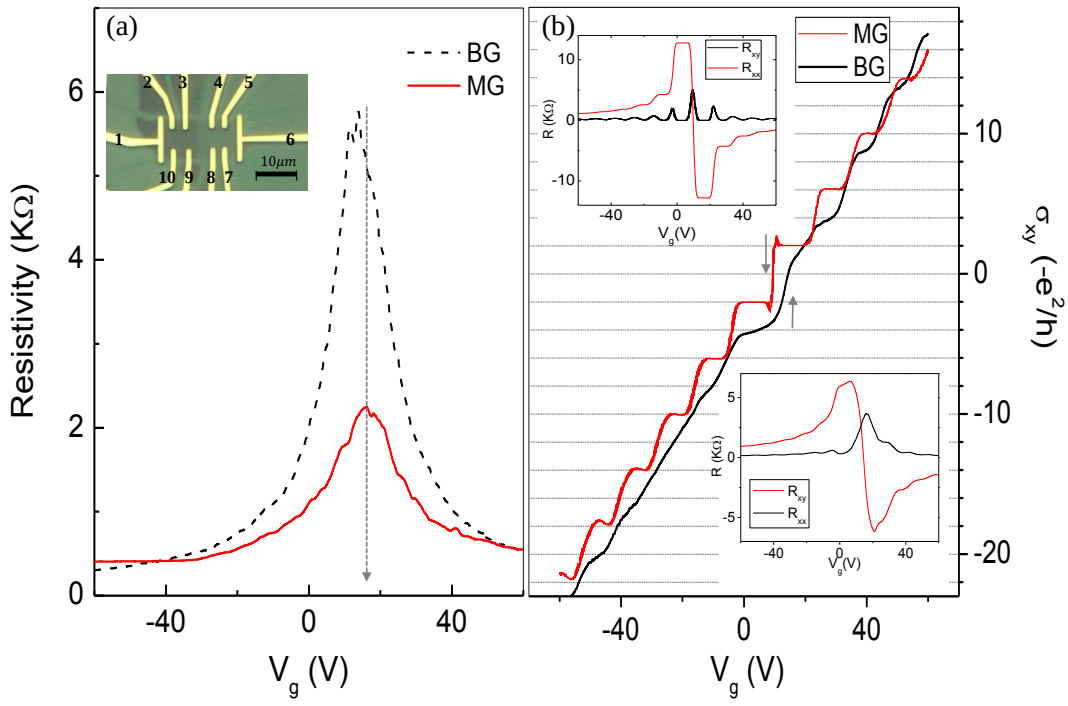

Figure 5.3: (a) Zero magnetic field resistivity of bilayer region (dashed red) and monolayer region (solid black), as a function of back gate voltage at $T = 1.7$ K. Top left inset: Optical image of the measured device; (b) Hall conductivity σ_{xy} vs. back gate V_g of MG side (red), and BG side (black). The gray arrows indicate the charge neutrality point for MG ($V_D^{MG} = 9.6$ V) and BG ($V_D^{BG} = 14.5$ V). Top left inset: Gate dependence of R_{xx} (in black) and R_{xy} (in red) of MG region; Bottom right inset: Gate dependence of R_{xx} (in black) and R_{xy} (in red) of BG region; All data are taken at $T = 1.7$ K $B = 8.8$ T.

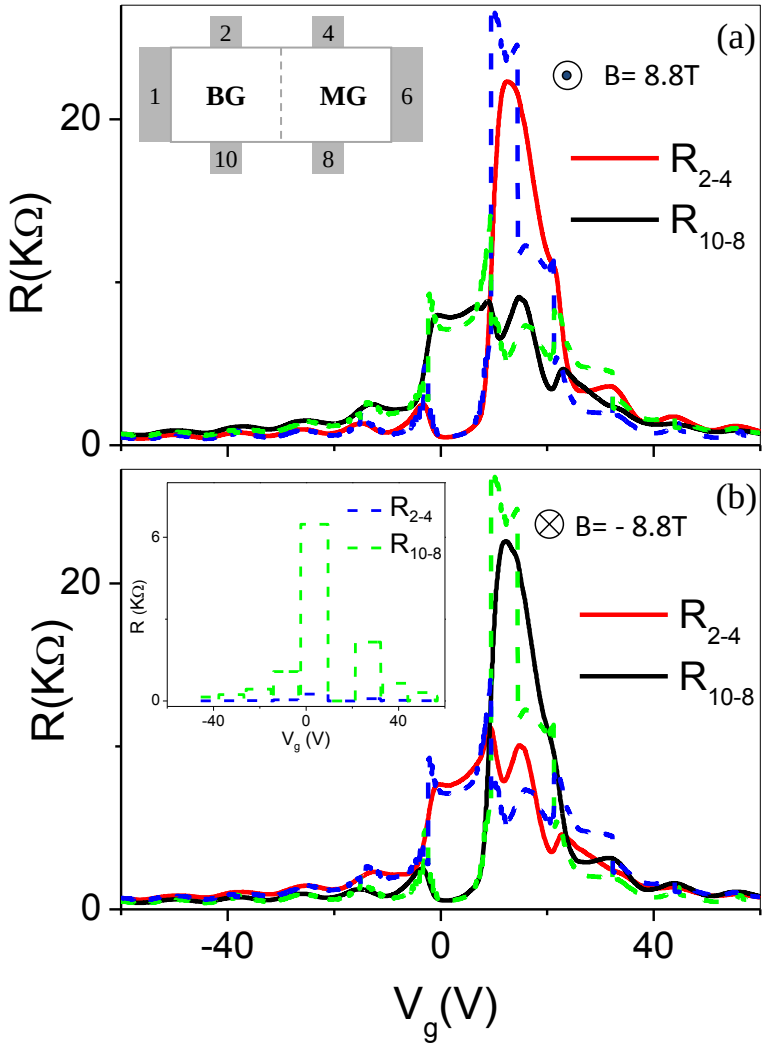

Figure 5.4: Transverse resistance across the MG/BG interface as a function of gate voltage at $B = 8.8$ T (top panel (a)) and $B = -8.8$ T (bottom panel (b)), current sent from contact 1 to contact 6. In both panels, the upper side transverse resistance R_{2-4} is always in red while the lower one R_{10-8} is in black. Fits of R_{2-4} and R_{10-8} ($R = R_{ideal} + R_{xx}^{MG} + R_{xx}^{BG}$), are plotted as dashed blue and dashed green lines, respectively. Inset of (b): theoretical plots for R_{2-4} and R_{10-8} (R_{ideal}) without considering Landau level broadening, assuming the Hall conductivity is always quantized.

QHE, we have $|N|$ channels of chiral edge modes when the system is in the quantum Hall regime with Hall conductivity $\sigma_{xy} = -Ne^2/h$. For BG and MG, we define the number of edge modes: $N_B = g_s g_\nu \times m$ and $N_M = g_s g_\nu \times (m' + 1/2)$, where $m, m' \in Z$, and $g_s = g_v = 2$ are number of degeneracy due to spin and valley respectively. Since N_B and N_M rarely coincide with each other, there should be edge channels with a number of $|N_B - N_M|$ traveling along the boundary of the MG/BG interface otherwise the excessive edge states would be discontinued at the junction interface.

Fig. 5.5(a) shows the edge channels considering $N_B > N_M$. Each arrow represents the direction of electron motion. Note that we consider only electron doping, while in the hole doping case, since the direction of electron motion in each channel becomes opposite compared to the corresponding electron doping, both results become equivalent by changing the upper and lower edges. At the upper edge, N_M modes among all N_B modes of the BG region continues into MG region, while the remaining channels $(N_B - N_M)$ are split and proceed along the MG/BG interface to the other side. At the lower edge, those channels combine with the edge channels in MG region and turn back to the origin. In Fig. 5.5(b),the edge channels of BG and MG change their roles, compared with Fig. 5.5(a). The chemical potential and the numbers of the edge states are denoted as in Fig. 5.5.

For Fig. 5.5(a), the energy conservation gives:

$$\mu' N_B = \mu_2 N_M + \mu_1 (N_B - N_M) \tag{5.3}$$

from which one can determine μ'. The Hall conductivity in MG and BG region is given by:

$$\sigma_{2-10} = \frac{I}{V_{2-10}} = -\frac{e^2}{h} N_B \tag{5.4}$$

$$\sigma_{4-8} = \frac{I}{V_{4-8}} = -\frac{e^2}{h} N_M \tag{5.5}$$

The voltage drop across the MG/BG interface are $V_{2-4} = 0$ and $V_{10-8} = (\mu' - \mu_2)/e$ for the upper and lower sides respectively. Then the transverse resistance across can

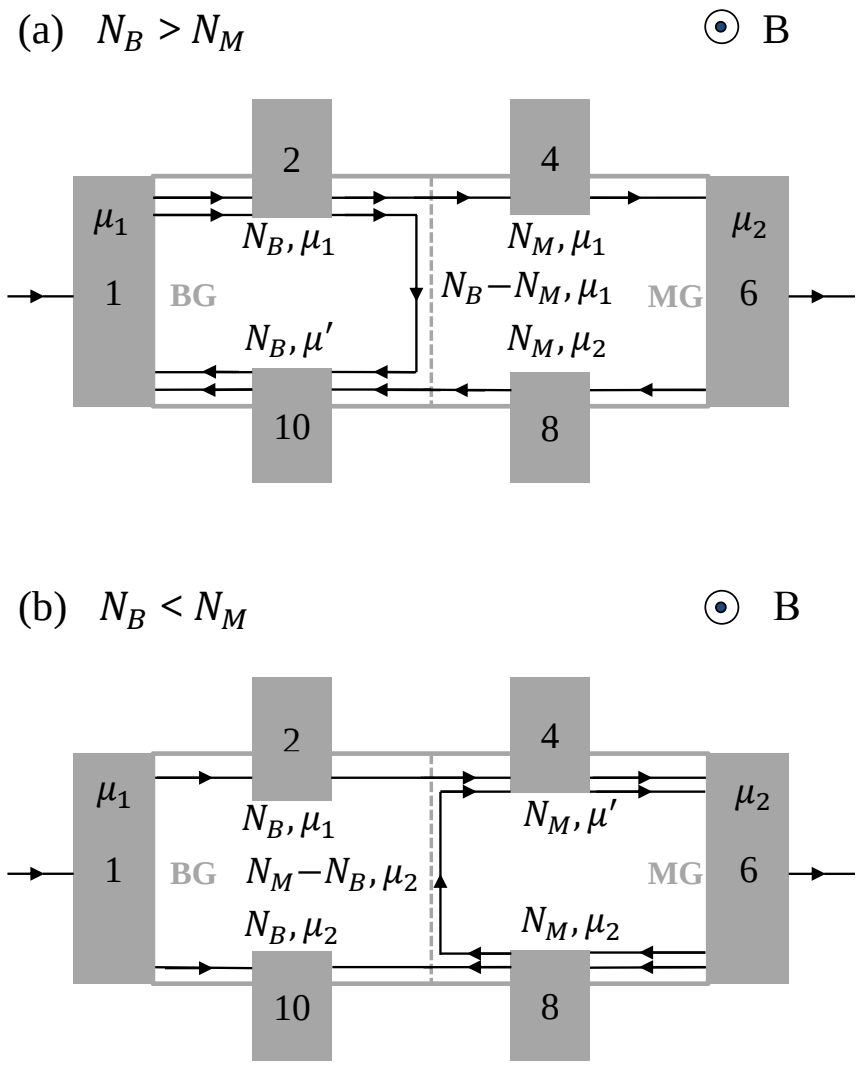

Figure 5.5: Schematic diagrams for the channel connections along the interface boundary for (a) $N_B > N_M$ and (b) $N_B < N_M$.

be deduced as:

$$\begin{aligned} R_{2-4} &\equiv \frac{V_{2-4}}{I} = 0 \\ R_{10-8} &\equiv \frac{V_{10-8}}{I} = \frac{h}{e^2}\left(\frac{1}{N_M} - \frac{1}{N_B}\right) \end{aligned} \tag{5.6}$$

Similarly, the cross resistance for Fig. 5.5(b) can be argued similarly:

$$\begin{aligned} R_{2-4} &\equiv \frac{V_{10-8}}{I} = \frac{h}{e^2}\left(\frac{1}{N_B} - \frac{1}{N_M}\right) \\ R_{10-8} &\equiv \frac{V_{2-4}}{I} = 0 \end{aligned} \tag{5.7}$$

Reversing magnetic field shall result in opposite motion of the carriers, thus leads to polarity change on the two sides. This explains the almost-zero transverse resistance and its corresponding change to a non-zero plateau as the direction of the magnetic field is shifted, as shown in Fig. 5.4(b).

At the carrier density ranges where both the MG part and BG part are in their QH regimes, the predicted transverse resistances across the MG/BG interface can be described by Eq. 5.6 and Eq. 5.7. Otherwise they would be the sum of the longitudinal resistances in each part. Assuming a step-like quantized Hall conductivity for both BG and MG, we plot R_{ideal} according to Eq. 5.7 for $V_D^{MG} = 9.6$ V, $V_D^{BG} = 14.5$ V, at $B = -8.8$ T, and the plots are shown in the inset of Fig. 5.4(b). Considering Landau level broadening, we add the corresponding longitudinal resistances at the MG and BG parts ($R = R_{ideal} + R_{xx}^{MG} + R_{xx}^{BG}$), where R_{xx}^{MG} and R_{xx}^{BG} are calculated from the experimental data according to the device geometry. A comparison between the measured transverse resistances across the interface and those predicted by the proposed edge channels along the interface boundary is plotted in Fig. 5.4, where the fits are plotted as dashed lines. We find an excellent agreement when the residual resistance away from the quantum hall state is taken into account.

For example when $V_g \in [0, 3]$ V, where $N_B = 4$ and $N_M = 2$, a plateau is developed near a quantized transverse resistance $\frac{h}{e^2}\left(\frac{1}{N_M} - \frac{1}{N_B}\right) = 6.5$ KΩ. A transverse resistance difference of ~ 14 KΩ between two sides of the Hall bar is also observed at

$V_g \sim 12$ V, which suggests excessive edge channels start to form along the interface boundary when the MG part has $N_B = 2$ edge channels on the hole side while the BG part develops $N_B = 4$ edge channels on the electron side.

5.5 Conclusion and future work

To conclude, we have measured the local surface potential variations at the interface of MG/BG junction devices. At the quantum Hall regime, we have observed asymmetric transverse resistance across the MG/BG interface with a polarity change as magnetic field is flipped. Edge states along the interface boundary could explain the observation quantitatively.

One can add a top gate on BG part of the junction device to have better control with continuously tunable interface LLs. The QH transport is to certain extent analogous to the QHE in graphene p-n junctions (Williams *et al.*, 2007), except for the two species of Dirac fermions, which makes it a more interesting system to study. Moreover, with the most recent technique using hexagonal boron nitride as dielectric layers, it is possible to study the quantum transport across the MG/BG interface in the symmetry broken regimes of MG and BG, or even in the fractional quantum Hall regimes.

Bibliography

Abanin, D. A., P. A. Lee, and L. S. Levitov, 2006, Physical Review Letters **96**(17), 176803.

Abanin, D. A., P. A. Lee, and L. S. Levitov, 2007a, Solid State Communications **143**(1-2), 77.

Abanin, D. A., K. S. Novoselov, U. Zeitler, P. A. Lee, A. K. Geim, and L. S. Levitov, 2007b, Physical Review Letters **98**(19), 196806.

Abanin, D. A., S. A. Parameswaran, and S. L. Sondhi, 2009, Physical Review Letters **103**(7), 076802.

Alicea, J., and M. P. A. Fisher, 2006, Physical Review B **74**(7), 075422.

Ando, T., 2006, J. Phys. Soc. Jpn. **75**(7), 074716.

Apalkov, V. M., and T. Chakraborty, 2006, Physical Review Letters **97**(12), 126801.

Barlas, Y., R. Côté, K. Nomura, and A. H. MacDonald, 2008, Physical Review Letters **101**(9), 097601.

Berciaud, S., M. Y. Han, K. F. Mak, L. E. Brus, P. Kim, and T. F. Heinz, 2010, Physical Review Letters **104**(22), 227401.

Berger, C., Z. Song, X. Li, X. Wu, N. Brown, C. Naud, D. Mayou, T. Li, J. Hass, A. N. Marchenkov, E. H. Conrad, P. N. First, *et al.*, 2006, Science **312**(5777), 1191.

Blake, P., E. W. Hill, A. H. C. Neto, K. S. Novoselov, D. Jiang, R. Yang, T. J. Booth, and A. K. Geim, 2007, Applied Physics Letters **91**(6), 063124.

Bolotin, K. I., F. Ghahari, M. D. Shulman, H. L. Stormer, and P. Kim, 2009, Nature **462**(7270), 196.

Bolotin, K. I., K. J. Sikes, Z. Jiang, M. Klima, G. Fudenberg, J. Hone, P. Kim, and H. L. Stormer, 2008, Solid State Communications **146**(9-10), 351.

Bostwick, A., T. Ohta, T. Seyller, K. Horn, and E. Rotenberg, 2007, Nat Phys **3**(1), 36.

Brandt, C. S. M., N. B., and Y. G. Ponomarev, 1988, *Modern Problems in Condensed Matter Sciences*, volume 29.1 (North Holland, Amsterdam).

Büttiker, M., 1988, Physical Review B **38**(14), 9375.

Castro, E. V., K. S. Novoselov, S. V. Morozov, N. M. R. Peres, J. M. B. L. dos Santos, J. Nilsson, F. Guinea, A. K. Geim, and A. H. C. Neto, 2007, Physical Review Letters **99**(21), 216802.

Castro Neto, A. H., F. Guinea, N. M. R. Peres, K. S. Novoselov, and A. K. Geim, 2009, Reviews of Modern Physics **81**(1), 109.

Checkelsky, J. G., L. Li, and N. P. Ong, 2008, Physical Review Letters **100**(20), 206801.

Checkelsky, J. G., L. Li, and N. P. Ong, 2009, Physical Review B **79**(11), 115434.

Chen, J.-H., C. Jang, S. Xiao, M. Ishigami, and M. S. Fuhrer, 2008, Nat Nano **3**(4), 206.

Cheng, Z., Q. Zhou, C. Wang, Q. Li, C. Wang, and Y. Fang, 2011, Nano Letters **11**(2), 767.

Das Sarma, S., and K. Yang, 2009, Solid State Communications **149**(37-38), 1502.

Dean, C. R., A. F. Young, P. Cadden-Zimansky, L. Wang, H. Ren, K. Watanabe, T. Taniguchi, P. Kim, J. Hone, and K. L. Shepard, 2011, Nat Phys **7**(9), 693.

Dean, C. R., A. F. Young, I. Meric, C. Lee, L. Wang, S. Sorgenfrei, K. Watanabe, T. Taniguchi, P. Kim, K. L. Shepard, and J. Hone, 2010, Nat. Nano. **5**(10), 722.

Dresselhaus, M. S., and G. Dresselhaus, 2002, Advances in Physics **51**(1), 1.

Du, X., I. Skachko, F. Duerr, A. Luican, and E. Y. Andrei, 2009, Nature **462**(7270), 192.

Efetov, D. K., and P. Kim, 2010, Physical Review Letters **105**(25), 256805.

Feldman, B. E., J. Martin, and A. Yacoby, 2009, Nat Phys **5**(12), 889.

Ferrari, A. C., J. C. Meyer, V. Scardaci, C. Casiraghi, M. Lazzeri, F. Mauri, S. Piscanec, D. Jiang, K. S. Novoselov, S. Roth, and A. K. Geim, 2006, Physical Review Letters **97**(18), 187401.

Fogler, M. M., A. H. Castro Neto, and F. Guinea, 2010, Physical Review B **81**(16), 161408.

Fradkin, E., 1986, Physical Review B **33**(5), 3263.

Fratini, S., and F. Guinea, 2008, Physical Review B **77**(19), 195415.

Fuchs, J.-N., and P. Lederer, 2007, Physical Review Letters **98**(1), 016803.

Geim, A. K., and K. S. Novoselov, 2007, Nat Mater **6**(3), 183.

Ghahari, F., Y. Zhao, P. Cadden-Zimansky, K. Bolotin, and P. Kim, 2011, Physical Review Letters **106**(4), 046801.

Giesbers, A. J. M., L. A. Ponomarenko, K. S. Novoselov, A. K. Geim, M. I. Katsnelson, J. C. Maan, and U. Zeitler, 2009, Physical Review B **80**(20), 201403.

Goerbig, M. O., R. Moessner, and B. Douçot, 2006, Phys. Rev. B **74**, 161407.

Goerbig, M. O., and N. Regnault, 2007, Physical Review B **75**(24), 241405.

Gusynin, V. P., V. A. Miransky, S. G. Sharapov, and I. A. Shovkovy, 2006, Physical Review B **74**(19), 195429.

Gusynin, V. P., and S. G. Sharapov, 2005, Physical Review Letters **95**(14), 146801.

Haldane, F. D. M., 1988, Physical Review Letters **61**(18), 2015.

Hall, E. H., 1879, American Journal of Mathematics **2**(3), 287.

Halperin, B. I., 1982, Physical Review B **25**(4), 2185.

Han, M. Y., B. Özyilmaz, Y. Zhang, and P. Kim, 2007, Physical Review Letters **98**(20), 206805.

Herbut, I. F., 2007, Physical Review B **75**(16), 165411.

Hou, C.-Y., C. Chamon, and C. Mudry, 2010, Physical Review B **81**(7), 075427.

Hwang, E. H., S. Adam, and S. Das Sarma, 2007, Physical Review Letters **98**(18), 186806.

Hwang, E. H., and S. Das Sarma, 2008, Physical Review B **77**(11), 115449.

Ishigami, M., J. H. Chen, W. G. Cullen, M. S. Fuhrer, and E. D. Williams, 2007, Nano Letters **7**(6), 1643.

Jain, J. K., 1989, Physical Review Letters **63**(2), 199.

Jiang, Z., Y. Zhang, H. L. Stormer, and P. Kim, 2007a, Physical Review Letters **99**(10), 106802.

Jiang, Z., Y. Zhang, Y. W. Tan, H. L. Stormer, and P. Kim, 2007b, Solid State Communications **143**(1-2), 14.

Jung, J., and A. H. MacDonald, 2009, Physical Review B **80**(23), 235417.

Katsnelson, M., and A. Geim, 2008, Philosophical Transactions of the Royal Society A: Mathematical, Physical and Engineering Sciences **366**(1863), 195.

Kharitonov, M., 2011, eprint arXiv:1103.6285 .

Khveshchenko, D. V., 2007, Physical Review B **75**(15), 153405.

Klitzing, K. v., G. Dorda, and M. Pepper, 1980, Physical Review Letters **45**(6), 494.

Kroto, H. W., J. R. Heath, S. C. O'Brien, R. F. Curl, and R. E. Smalley, 1985, Nature **318**(6042), 162.

Kurganova, E. V., H. J. van Elferen, A. McCollam, L. A. Ponomarenko, K. S. Novoselov, A. Veligura, B. J. van Wees, J. C. Maan, and U. Zeitler, 2011, Physical Review B **84**(12), 121407.

Landau, L. D., and E. M. Lifshitz, 1980, *Statistical Physics, Part I* (Pergamon, Oxford).

Li, D., W. Windl, and N. P. Padture, 2009, Advanced Materials **21**(12), 1243.

Martin, J., N. Akerman, G. Ulbricht, T. Lohmann, J. H. Smet, K. von Klitzing, and A. Yacoby, 2008, Nat Phys **4**(2), 144.

McCann, E., and V. I. Falko, 2006, Physical Review Letters **96**(8), 086805.

McClure, J. W., 1956, Physical Review **104**(3), 666.

Meric, I., M. Y. Han, A. F. Young, B. Ozyilmaz, P. Kim, and K. L. Shepard, 2008, Nat Nano **3**(11), 654.

Meyer, J. C., A. K. Geim, M. I. Katsnelson, K. S. Novoselov, T. J. Booth, and S. Roth, 2007, Nature **446**(7131), 60.

Mikito Koshino, E. M., 2009, PRB **79**(125443).

Morozov, S. V., K. S. Novoselov, M. I. Katsnelson, F. Schedin, D. C. Elias, J. A. Jaszczak, and A. K. Geim, 2008, Physical Review Letters **100**(1), 016602.

Nakanishi, T., M. Koshino, and T. Ando, 2010, Physical Review B **82**(12), 125428.

Nandkishore, R., and L. Levitov, 2010, Physical Review Letters **104**(15), 156803.

Nomura, K., and A. H. MacDonald, 2006, Physical Review Letters **96**(25), 256602.

Nomura, K., and A. H. MacDonald, 2007, Physical Review Letters **98**(7), 076602.

Nomura, K., S. Ryu, and D.-H. Lee, 2009, Physical Review Letters **103**(21), 216801.

Novoselov, K. S., A. K. Geim, S. V. Morozov, D. Jiang, M. I. Katsnelson, I. V. Grigorieva, S. V. Dubonos, and A. A. Firsov, 2005a, Nature **438**(7065), 197.

Novoselov, K. S., A. K. Geim, S. V. Morozov, D. Jiang, Y. Zhang, S. V. Dubonos, I. V. Grigorieva, and A. A. Firsov, 2004, Science **306**(5696), 666.

Novoselov, K. S., D. Jiang, F. Schedin, T. J. Booth, V. V. Khotkevich, S. V. Morozov, and A. K. Geim, 2005b, Proceedings of the National Academy of Sciences of the United States of America **102**(30), 10451.

Novoselov, K. S., E. McCann, S. V. Morozov, V. I. Fal'ko, M. I. Katsnelson, U. Zeitler, D. Jiang, F. Schedin, and A. K. Geim, 2006, Nat Phys **2**(3), 177.

Ohta, T., A. Bostwick, T. Seyller, K. Horn, and E. Rotenberg, 2006, Science **313**(5789), 951.

Peirls, R. E., 1934, Helvetica Physica Acta **7**, 81.

Peres, N. M. R., F. Guinea, and A. H. Castro Neto, 2006, Physical Review B **73**(12), 125411.

Petrone, N., 2011, unpublished.

Plochocka, P., C. Faugeras, M. Orlita, M. L. Sadowski, G. Martinez, M. Potemski, M. O. Goerbig, J. N. Fuchs, C. Berger, and W. A. de Heer, 2008, Physical Review Letters **100**(8), 087401.

Prada, E., P. San-Jose, G. LeÃşn, M. M. Fogler, and F. Guinea, 2010, Physical Review B **81**(16), 161402.

Puls, C. P., N. E. Staley, and Y. Liu, 2009, Physical Review B **79**(23), 235415.

Semenoff, G. W., 1984, Physical Review Letters **53**(26), 2449.

Shibata, N., and K. Nomura, 2009, Journal of the Physical Society of Japan **78**(10), 104708.

Shimshoni, E., H. A. Fertig, and G. V. Pai, 2009, Physical Review Letters **102**(20), 206408.

Shizuya, K., 2009, Physical Review B **79**(16), 165402.

Skachko, I., X. Du, F. Duerr, A. Luican, D. A. Abanin, L. S. Levitov, and E. Y. Andrei, 2010, Philosophical Transactions of the Royal Society A: Mathematical, Physical and Engineering Sciences **368**(1932), 5403.

Slonczewski, J. C., and P. R. Weiss, 1958, Physical Review **109**(2), 272.

Tapaszto, L., G. Dobrik, P. Lambin, and L. P. Biro, 2008, Nat Nano **3**(7), 397.

Töke, C., and J. K. Jain, 2007, Physical Review B **75**(24), 245440.

Töke, C., P. E. Lammert, V. H. Crespi, and J. K. Jain, 2006, Physical Review B **74**(23), 235417.

Tsui, D. C., H. L. Stormer, and A. C. Gossard, 1982, Physical Review Letters **48**(22), 1559.

Wallace, P. R., 1947, Physical Review **71**(9), 622.

Williams, J. R., L. DiCarlo, and C. M. Marcus, 2007, Science **317**(5838), 638.

Yang, K., 2007, Solid State Communications **143**(1-2), 27.

Yoshida, Z., and E. Osawa, 1971, Aromaticity Chemical Monograph(Kagaku Dojin, Kyoto, Japan) **22**, 174.

Young, A. F., 2011, unpublished.

Yu, Y.-J., Y. Zhao, S. Ryu, L. E. Brus, K. S. Kim, and P. Kim, 2009, Nano Letters **9**(10), 3430.

Zhang, Y., Z. Jiang, J. P. Small, M. S. Purewal, Y. W. Tan, M. Fazlollahi, J. D. Chudow, J. A. Jaszczak, H. L. Stormer, and P. Kim, 2006, Physical Review Letters **96**(13), 136806.

Zhang, Y., Y.-W. Tan, H. L. Stormer, and P. Kim, 2005, Nature **438**(7065), 201.

Zhang, Y., T.-T. Tang, C. Girit, Z. Hao, M. C. Martin, A. Zettl, M. F. Crommie, Y. R. Shen, and F. Wang, 2009, Nature **459**(7248), 820.

Zhao, Y., P. Cadden-Zimansky, Z. Jiang, and P. Kim, 2010, Physical Review Letters **104**(6), 066801.

Zhao, Y., F. Ghahari, P. Cadden-Zimansky, and P. Kim, 2011, unpublished.

Zheng, Y., and T. Ando, 2002, Physical Review B **65**(24), 245420.

Appendix A

Calibrations of tilted angle of the magnetic field

A major part of the experiments in this thesis was performed at the National High Magnetic Field Laboratory (NHMFL) in Tallahassee, Florida. Two magnet cells are used for the data presented in this thesis: 45 T/32 mm Hybrid Magnet (Cell 15) described in Chap. 4, and 35 T/32 mm Resistive Magnet (Cell 12) in Chap. 3. All experiments are conducted using a rotator probe with a variable temperature insert (VTI). Fig. A.1(a) shows a typical sample wirebonded to a custom-made G-10 socket. The socket is inserted into a copper cylinder, which is rotatable through the motorized header (Fig. A.1(c)) by changing the rotator spring length (Fig. A.1(b)).

As described in the inset of Fig. A.2, perpendicular magnetic field ($B_\perp$) can be calculated from total magnetic field B_{tot} through $B_\perp = B_{tot}\cos\theta$. To investigate the spin-component in the symmetry broken QH states, we need a sufficiently large Zeeman energy $E_z = g\mu_B B_{tot} \sim 1.34 B_{tot}$ [K] over a unchanged Coulomb energy $E_{e-e} = e^2/4\pi\epsilon_0\epsilon_r l_B \sim 649\sqrt{B_\perp}/\epsilon_r$ [K], where ϵ_r is the dielectric constant. Thus a large tilting angle is required to magnify the effect of Zeeman splitting. Assuming $B_\perp = 20$ T and $\epsilon_r = 4$, $\theta > 40°$ is needed to reach $E_z/E_{e-e} > 5\%$. However, the control of angle tilting through the step motor control could be with a few degrees error, or even higher due to the subjective judgment of zero-tilting. A 5°-error would

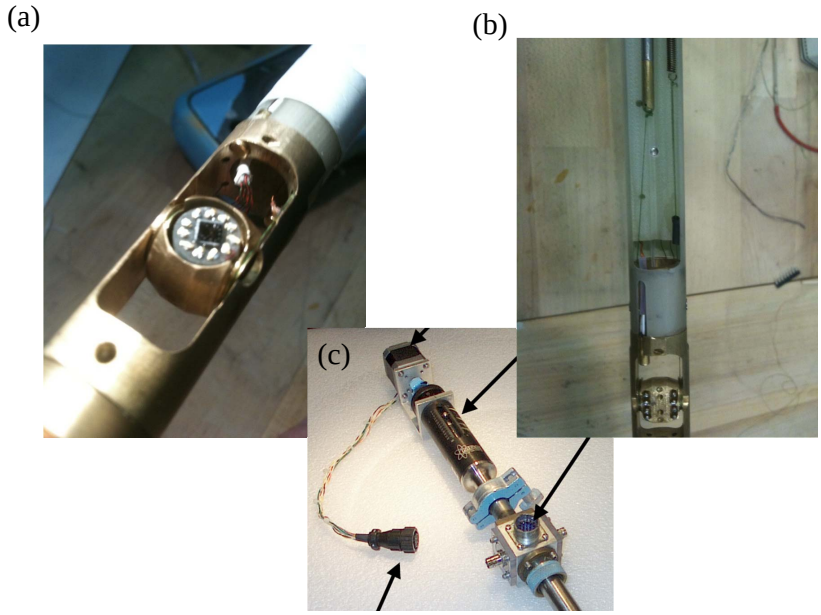

Figure A.1: (a) A sample wirebonded onto a G-10 socket, which is affixed to the rotatable copper cylinder; (b) Back side of a rotator probe: a spring is used to control the rotation; (c) Rotator probe header with a step motor control; panel (c) is from NHMFL's website.

lead to about 2 T difference in $B_\perp$ when B_{tot} is 10 T at $\theta = 60°$. Therefore, to eliminate possible experimental error, it is very important to control the value of $B_\perp$ and B_{tot} with the highest possible precision. The required angle accuracy is usually below 0.2°. Thus a separate angle calibration utilizing the half-integer QHE in graphene itself is performed.

For devices with Hall bar geometry, the calibration process is as the following. We first determine the zero-tilting by the classical Hall effect. Under a small magnetic field, R_{xx} remains the same, while R_{xy} changes linearly with $B_\perp$ through the relation

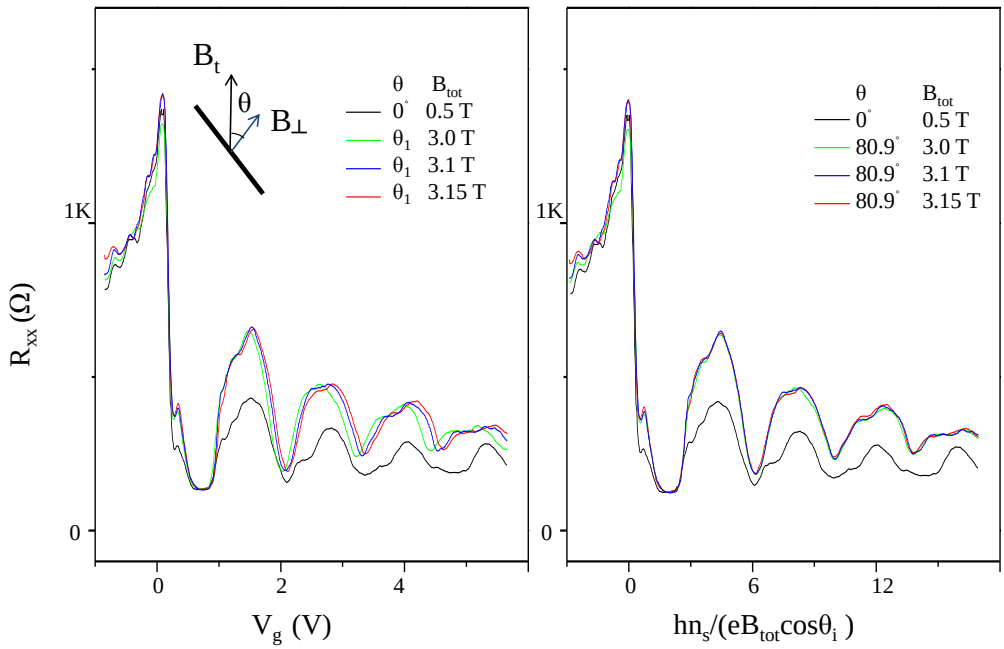

Figure A.2: An example of calibration for a four-probe suspended monolayer graphene device: (a) R_{xx} as a function of back gate under the same unknown tilting angle $\theta = \theta_1$, with $B_{tot} = 3, 3.1, 3.15$ T. Black curve is a reference curve at known $\theta = 0$, $B_{tot} = 0.5$ T; inset: a schematic of tilted magnetic field with total field B_{tot}, and tilting angle θ. (b) After calibration, R_{xx} vs. filling fraction, showing a good match of the R_{xx}^{min}'s. The unknown tilting angle is found to be $\theta = 80.9°$.

$n = \frac{1}{e}\frac{dB_\perp}{dR_{xy}}$. Thus zero-tilting can be achieved by finding the slope of $\frac{d_B}{dR_{xy}}$ with the largest absolute value.

Then we ascertain the absolute value of a tilted angle by the QHE. Under high magnetic field, for monolayer graphene, the LL energy is given by: $\sqrt{2|n|\frac{\hbar^2 v_f^2}{l_B^2}}$, where

the magnetic length $l_B = \sqrt{\frac{\hbar}{eB_\perp}}$ depends only on $B_\perp$. Assuming that the change of angle responds linearly to the header rotation ($\theta_{real} = \alpha\theta_i$), we take several gate sweeps of longitudinal resistance R_{xx} under a fixed tilting angle (θ_i read from the header rotation) at a few different B_{tot}. The R_{xx}^{min}'s should be aligned at the corresponding filling fractions $\nu = hn/[eB_{tot}\cos(\alpha\theta_i + \theta_0)]$. The left panel of Fig. A.2 shows a set of calibration curves for a multi-terminal device of suspended monolayer graphene, where the initial offset $\theta_0 = 0$ has already been determined by the classical Hall effect. The real angles are found to be $\cos^{-1}(\frac{hn}{eB_{tot}\nu})$, $\nu = \pm 2, \pm 6...$ for monolayer graphene. The angle calibration for bilayer graphene devices can be completed similarly, with R_{xx}^{min}'s appearing at filling factors $\nu = \pm 4, \pm 8....$ Since the position of R_{xx}^{min}'s can be affected by the broadening of LLs, we usually test the curve alignment under a fixed B_p with a series of tilted angles to reassure the calibration.

In fact, at very large tilted angles, when spin splitting starts taking effect, there could an oscillatory contribution to R_{xx} described as:

$$\Delta R_{xx} = A\cos(2\pi n + \pi + \varphi_B), \quad A = A_0(n)\cos\frac{\pi}{2}\frac{g^* m^*}{m_e}\frac{B_{tot}}{B_\perp}, \tag{A.1}$$

where $\varphi_B = \pi$ is the monolayer graphene berry phase and cyclotron mass is determined by $m^* = \frac{\hbar^2}{2\pi}\frac{\partial S}{\partial E}$ (S is the area of the orbit in k-space). As a result, the calibrated curves at fixed $B_\perp$ may not have the same R_{xx}^{min}'s since the oscillatory contribution becomes more pronounced as increasing tilted angle, as shown in Fig. A.2. Although reasonable calibrations can be achieved by aligning the position of R_{xx}^{min}'s on the x-axis, we should be aware that relatively larger calibration errors are expected at larger tilted angles.